THE UNIVERSITY OF CHICAGO

DISCOVERY OF A CHOLINERGIC CIRCUIT THAT RELIEVES PAIN, DESPITE OPIOID TOLERANCE

A DISSERTATION SUBMITTED TO
THE FACULTY OF THE DIVISION OF THE BIOLOGICAL SCIENCES
AND THE PRITZKER SCHOOL OF MEDICINE
IN CANDIDACY FOR THE DEGREE OF
DOCTOR OF PHILOSOPHY

COMMITTEE ON NEUROBIOLOGY

BY
SHIVANG SULLERE

CHICAGO, ILLINOIS
AUGUST 2023

Table of Contents

Table of Figures

Table of Supplementary Figures

Acknowledgments

I want to thank Dan McGehee. Without you, I would not be in this program studying neuroscience. Thus, my current and future career in neuroscience is due to you. You took a chance on me, and I hope that someday I can pay it back, or at the very least, pay it forward. You have taught me many things in neuroscience, but the few concepts that I will never forget, include: 1. How to identify interesting scientific questions and use the best methods to convincingly answer them, 2. How to focus efforts toward a clear and logical goal, and 3. The value of intellectual freedom and critical thinking for creating engaging science and passionate scientists. Of course, I will also fondly remember your love for English and your hatred for paperwork. I am grateful for your trust in my abilities and ideas and for accepting my mistakes and shortcomings. These were especially evident during my multiple failures with imaging studies or when the project pushed us in unexpected directions. This trust and acceptance allowed me to develop confidence and independence. I am lucky to have received that from you and can only hope to pass it forward one day. After the Keystone conference, when you said I should go ahead with my ridiculous ideas, it was perhaps the most decisive moment of my career trajectory. Most importantly, I am grateful to have been trained by a good person.

I also thank all the current and past members of the McGehee lab. Braeden, thank you for teaching me surgeries. Chandrika, thank you for teaching me how to patch neurons. Nichole, thank you for teaching me the value of behavioral assays and the importance of a clinical perspective. Alexis, thank you for repeatedly teaching me how to stand up for myself. Ross, thank you for many things, including teaching me the value of focusing on myself, helping me develop a more nuanced appreciation for issues that alter science, and listening to my whines over a cup of coffee. I would also like to thank Josephine Buclez for being an amazing person to work with, rapidly learning techniques, and contributing valuable data that yielded an R01. Loren, thank you for being an honorary member of our lab and contributing unique insights to this thesis!

I would also like to thank my friends in the program, especially Ben, Caroline, and Oliver. Ben, you are an amazingly energetic person. You have all the characteristics to be a fantastic physician, and I hope we can continue to have fun discussions about science in the midst of all your patients. Caroline, you are a brilliant and resourceful person. Our meetings significantly strengthened my own analysis. I wish that science could figure out a way to keep you around. Oliver, thank you so much for exploring all the restaurants with me! Our conversations during those drives have kept me sane. You were essential for my understanding of anything computational. You will be an incredible scientist if you decide to! Nelson, Carolina, and Anastasia thank you very much for your support and availability to chat with me!

I also thank my committee members: Peggy Mason and Jason MacLean. Peggy taught me the value of asking critical questions when I was 'stuck in the weeds' and challenged me to improve my presentation and thinking style. Jason taught me the importance of a published body of work, and I am still trying my best to make that happen! I would also like to thank Xiaoxi here. While not on my committee, he has always been an invaluable sounding board and critical in developing my scientific thinking and statistical understanding. All of your critiques have substantially strengthened me as a scientist, bettering me from where I started with an almost nonsensical first committee meeting. Thank you for helping with my career development, and I hope I remember those critiques forever!

To Alissa and Fred, thank you for your support and guidance. Without Fred, I would just have lofty scientific goals without any acumen. Discussing ideas with you are some of the best memories of my graduate training. Seeing you battle various challenges during your lab setup was perhaps the most critical training I was privileged to receive. Our experiments with naked mole rats at 1 am at night will truly be some of my fondest memories. Alissa, this project is more of your success than mine. You were perhaps the most essential and defining person of my graduate research. You worked hard, thought creatively, suggested ideas, and made me appreciate clinical perspectives. Your attention to detail and motivation to perfect techniques were amazing to behold. I cherish every espresso we had over the four years we worked together. I am grateful to have worked with you, and I hope this synergy continues for ages!

I would also like to thank the support people in the department, including Elena, Donna, and all others, for your help and support. Vytas, thank you for trusting me and your favorite and expensive microscope. It was critical for this PhD. The ARC staff kept the lab functional, especially during Covid-19. I would also like to thank Denise, Dr. Cohen, Dr. Mukesh, and Manish Sanghvi. Without you, it is an overstatement to say that I would be here physically. You helped me through critical challenges in my mental and physical health. Denise, thank you for your selfless love and affection for all of us! We feel it.

Finally, I want to express my heartfelt gratitude to my wife, Aishwarya Mahajan, my mother, Dr. Sunita Sullere, and my father, Dr. Vivek Sullere. Mom and Dad, you worked hard and inspired me and continue to do so. You honestly are my heroes, and I wish I could be 5% of what you are. Your service to humanity, your friends, and your family (mom, particularly here) is beyond everyone. If I have any work ethic or passion in this life, it is because of you. I know you never felt that you were doing anything great or meaningful when you were running around driving me from school to sports and then to classes, but I remember and appreciate it. It was not a trivial challenge raising me. I know I cannot repay you, but I hope I can be half as successful at passing on your values to people around me! Aishwarya, I had the courage to seek a better outlook on life because of you. You supported me whenever experiments failed or I disagreed with my PI, committee, or other scientists. You made my life easy and simple. Despite your own demanding work schedule, you always made time for me, to listen to me practice my talk and stumble through writing emails. I know I can never support you as much as you support me every single day. Your sitting next to me while I was analyzing or your staying up for me when experiments were running late made the most challenging losses seem trivial. I am forever grateful for your presence in my life, and I could not have made this journey without you. I wish I could someday do half of what you did for me, but you are immensely capable of taking your career to amazing heights. I am grateful for everything. This project is a discovery of a potentially important circuit, but my best discovery will always be you!

Abstract

Chronic pain pathologies plague society. While opioids effectively relieve pain, significant side effects, abuse liability, and development of analgesic tolerance outweigh their benefits. Furthermore, increasing levels of opioid prescription and repeated subsequent use has led to the current opioid epidemic, requiring substantive research efforts, as evidenced by the NIH's Helping to End Addiction Long-term Initiative (HEAL) initiative. Whether other endogenous neuromodulators and their receptors can be harnessed to relieve pain with efficacy similar to opioids has not been thoroughly explored.

The role of the neuromodulator Acetylcholine (ACh) in CNS function has been enigmatic. In this thesis, we explored the role of ACh in the ventrolateral periaqueductal gray (vlPAG), a key nucleus of the descending pain modulatory pathway. We found that nocifensive behaviors decreased ACh release in the vlPAG. Additionally, reversing this decrease in ACh by selectively activating cholinergic projections from Pedunculopontine Tegmental Nucleus (PPTg) to the vlPAG decreased the somatic and affective components of acute and chronic pain in opioid naïve and tolerant mice.

We determined that the antinociceptive effects of this cholinergic circuit were mediated through α7 nicotinic acetylcholine receptors (nAChR), which are co-expressed on μ-opioid receptor-expressing (*Oprm1*$^{+}$) GABAergic vlPAG neurons. Parallel *in vivo* experiments revealed an unexpected physiological impact of α7 nAChRs activation: these non-selective cation channels inhibited neuronal activity in a cell-autonomous manner multiple minutes after receptor activation. Using molecular biology and slice electrophysiology, we identified the intracellular signaling mechanism underlying this counter-intuitive decrease in activity: activation of α7

nAChRs decreased neuronal excitability by phosphorylating voltage-gated potassium channels, a mechanism similar to the mechanism proposed for opioid receptors in the vlPAG.

Finally, we explored the manifestation and progression of chronic pain state and opioid tolerance in the vlPAG *in vivo*. The value of obtaining insights in awake-behaving animals is perhaps of utmost importance in the descending pain modulatory pathways, given that the central dogma comes from work conducted in lightly anesthetized animals, which has been questioned. In this thesis, we use 2-photon imaging to track the progression of aberrant neuronal ensemble dynamics. This work leads to unexpected insights into the recruitment of non-pain-responsive neurons into the pain-encoding ensemble. We also observe that α7 nAChRs agonists effectively relieve pain by inhibiting the *Oprm1*$^{+}$ pain-sensitive neuronal ensembles in the vlPAG, even in opioid-tolerant animals. Finally, unlike opioids, α7 nAChRs agonists did not show the development of tolerance, reward profile, or withdrawal symptoms.

To obtain these insights, we have employed methods that allow for rigorous cross-verification at multiple levels. Cross-disciplinary approaches include mRNA measurements, cell-type specific anatomical tracing, *ex-vivo* electrophysiology to assay receptor function and neuronal excitability, and *in-vivo* 2-photon imaging to track the cellular basis for the onset and progression of chronic pain and opioid tolerance. These assays are supplemented by cell-type and circuit-specific manipulations to assay the impact on sensory and affective-motivational aspects of pain behaviors. Together, these investigations identify a novel circuit that modulates pain signaling and non-opioid therapeutic targets for the management of chronic pain.

Introduction

Acetylcholine as a neuromodulator in the central nervous system

Acetylcholine (ACh) is perhaps evolutionarily the oldest and the most well-studied neurotransmitter. It mediates neuromuscular and autonomic sympathetic and parasympathetic neurotransmission either directly or through (nor/)epinephrine. These functions of ACh are essential for mammalian fitness and survival[1–9]. However, in addition to this critical role of ACh in the periphery, in the central nervous system (CNS), the various roles of ACh have been more challenging to identify[8,10–13].

Few roles of ACh in the CNS have been isolated using pharmacological and electrophysiological methods[13]. In the mesolimbic and nigrostriatal circuits, ACh plays key roles in short and long-term modulation of synaptic transmission, potentially leading to changes in reward processing and appropriate cue-reward association with salient sensory information[14]. In the cortex, ACh is known to modulate attention. These effects of ACh are primarily mediated through GABAergic interneurons in the cortex to precisely inhibit pyramidal neurons[13]. In these cortical circuits, ACh also regulates the signal-to-noise ratio of sensory stimuli, cue detection, and memory formation. In the hippocampus, in addition to contributing to learning and memory, ACh also regulates cue-associated stress adaptation through amygdalar and hypothalamic inputs[13]. In the hypothalamus, ACh regulates primitive and critical behaviors for survival, including body-temperature maintenance, sleep states, food intake, and glucose metabolism, by exerting effects in the hypothalamus. While emphasizing the importance of ACh, the richness of the behaviors regulated by ACh increases the difficulty in clearly ascribing behavioral functions to this neurotransmitter, necessitating various conceptual and methodological innovations[13].

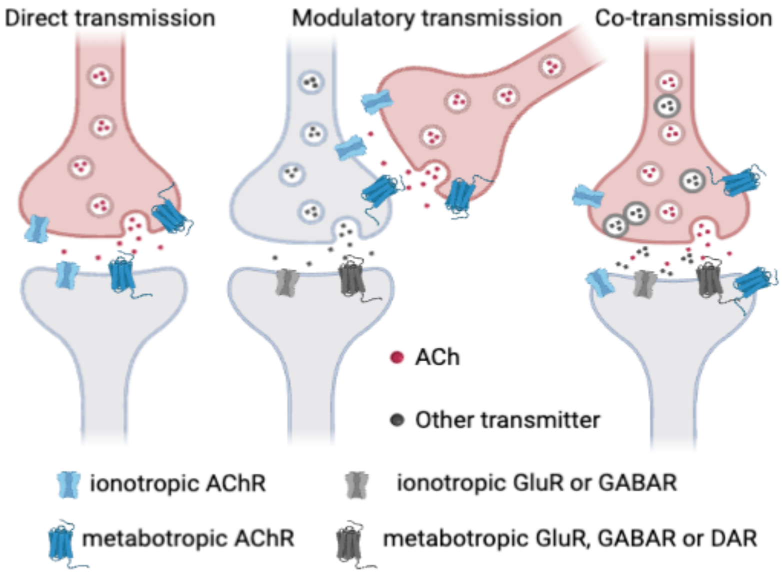

Figure 1: Different types of cholinergic synapses
Adapted[13]

In the CNS, the mode of action of cholinergic transmission has also been controversial: both fast synaptic transmission and volume transmission have been proposed[15]. Fast excitatory synaptic transmission between closely apposed synaptic sites is primarily attributed to glutamate in the CNS. However, rare occasions of fast cholinergic synaptic transmission have been identified[16,17]. Generally, ACh is thought to signal through bulk-volume transmission where the temporally coordinated release of ACh occurs through diffuse axonal arborizations[15]. Single neuron studies suggest that the axonal terminals of cholinergic neurons span large volumes[15]. These large arbors may help encode a behavioral or physiological state of the organism. For example, these cholinergic arbors are thought to tune numerous cortical networks across behaviors such as running[15]. ACh also acts on receptors expressed on presynaptic terminals to strongly influence release probability[18–20]. Volume transmission is well-suited to modulate the release probability through these presynaptic mechanisms. Observing fast synaptic transmission is further compounded by the potential of co-transmission with additional neurotransmitters. The habenulo-peduncular and tegmento-mesolimbic circuits demonstrate strong evidence of co-transmission through the same or parallel axonal fibers[21,22]. This co-release of additional neurotransmitters occludes appropriate monitoring of cholinergic transmission, especially using electrical stimulation methods. The recent advances in optogenetic methods (discussed later) have aided in better characterization of cholinergic synapses in the CNS[13]. However, generally, cholinergic synapses have facilitating post-synaptic responses suggestive of extra-synaptic localization of receptors as opposed to a direct synaptic contact[21,22].

ACh synthesizing neurons have been traditionally identified and labeled through the expression of Choline Acetyl Transferase (ChAT) and vesicular Acetylcholine Transporters (vAChT)[23]. While expression of these proteins does not establish ACh release, they have served as valuable guides in identifying cholinergic brain regions[24]. These results have been further verified using ChAT-GFP and ChAT-Cre mouse lines that allow selective labeling of genetically defined populations of neurons. Sparse interneurons have been identified in cortical regions like primary and secondary motor areas and primary somatosensory and visual areas. Striatal cholinergic interneurons are also well studied[25,26]. While the cortex and striatum harbor local interneurons, long-range projections are primarily harbored in the following brain regions: 1. Medial Septum/Ventral Diagonal Band of Broca, 2. Horizontal Diagonal Band of Broca, 3. Medial Habenula, 4. Arcuate and Dorsomedial Nucleus of the Hypothalamus, 5. Parabigeminal Nucleus, 6. Pontine Gray, 7. Nucleus Ambiguus , 8. Pedunculopontine Tegmental Nucleus, and 9. Laterodorsal Tegmental Nucleus[24]. Most of these brain nuclei either send diffuse axonal arborizations, e.g., Medial Septum, or have a focused output, e.g., Medial Habenula. The output brain regions generally show high levels of ACh Esterase (AChE) to clear Acetylcholine from synaptic clefts and regulate ACh buildup and signaling in the postsynaptic structures[24]. Additional brain regions that express cholinergic neurons comprise the brainstem motor nuclei[24]. The cholinergic system regulates various aspects of postsynaptic structure-function, including sensory processing, learning, memory, fear-responding, attention, sleep, running, and arousal[8,10–13].

Signaling in the postsynaptic structures is mediated through two broad categories of ACh receptors (AChRs): ionotropic-nicotinic (nAChRs) and metabotropic-muscarinic (mAChRs) [23]. In the mammalian CNS, the nicotinic AChRs in the mammalian CNS are pentamers of the following subunits: α2, α3, α4, α5, α7, α9, α10, β1, β2, β3, β4, and β5[23]. The pentamers form either homopentamers in the case of α7, α9, and α10 subunits or heteropentamers with α and β subunits. The stoichiometry of these receptors results in different properties, including binding affinity and calcium permeability. The different binding properties and intracellular signaling provide a rich avenue for pharmacological targeting strategies[23]. Interestingly, non-canonical signaling processes with Ca-permeable receptors (e.g., NMDA) are increasingly being identified, and these provide rich avenues for significant further exploration[27–31]. This is most true for the α7 nAChR, which can have >10~20 times the permeability for Ca^{2+} as opposed to Na^{+}[32]. Indeed, in the wise words of a neurophysiology colleague, these a7 nAChRs should really be thought of as ligand-gated Ca channels. The metabotropic-muscarinic receptors are 7-transmembrane (TM) G-protein coupled receptors of M1, M2, M3, M4, and M5 types[23]. These receptors can differentially alter intracellular signaling through intracellular Ca^{2+} concentrations, cAMP, Adenyl Cyclase, PLCβ and MAPK pathways, GIRK currents, voltage-gated Ca^{2+} channels, and

M-type current via $G_{\alpha s/q}$ and $G_{\alpha i/o}$ pathways[23]. In some cases, the Gβ, Gɣ proteins, and β-arrestin signaling mechanisms have also been proposed[23].

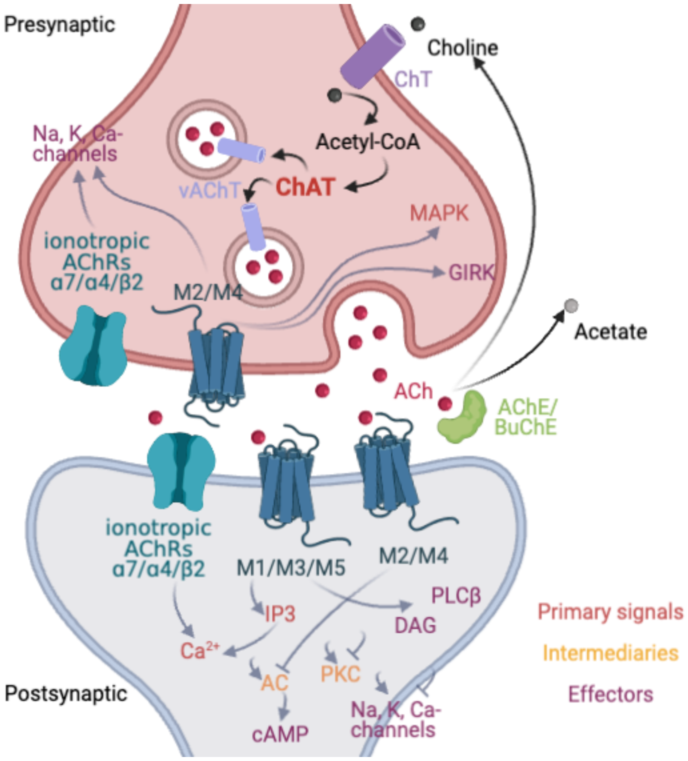

Figure 2: Representative cholinergic synapse
Conventional localization of cholinergic receptors and the subsequent downstream signaling is represented. Acetylcholine synthesis and breakdown are represented as well[23].

In this project, we aim to identify: 1. How ACh modulates pain. 2. The brain regions and the receptor systems responsible for the pain-altering effects of ACh. And, 3. The signaling pathways that yield the observed behavioral effects.

Pain modulatory role of the ventrolateral periaqueductal gray

While pain plays a critical role in organismal survival, chronic pain resulting from the aberrant excitability and connectivity of the pain pathways is a major burden for society[33]. These nociceptive circuits begin with nociceptor neurons at the periphery which express receptors for temperature, mechanical stretch, and tissue damage[34,35]. Activation of these nociceptors is communicated to neurons in the dorsal horn of the spinal cord, which through the spinothalamic tract, communicate nocifensive information to the thalamus and onwards to cortical areas[34,35]. In addition to the spinothalamic tract, multiple parallel pathways send nocifensive information to other brain regions, including descending pain modulatory pathways, resulting in parallel copies[35]. These efference copies are essential for appropriate encoding and modulation based on brain states ranging from identifying properties of the stimuli or altering affective and cognitive behaviors[35–38]. To note here, nociceptor activation does not always result in pain percept as the manifestation of pain requires activation of various cortical regions along with certain sub-cortical regions like the amygdala[39]. In mammals, this pain perception is also controlled by the descending pain modulatory pathways[34,35,40–45]. These descending pain modulatory pathways are the focus of this thesis.

The descending pain modulatory pathway comprises the ventrolateral periaqueductal gray (vlPAG) and its projections to the rostral ventromedial medulla (RVM) and the locus coeruleus (LC) [46,47]. Pain perception in mammals, including humans, can be robustly modulated by changing neuronal activity in the vlPAG, making it an ideal site for the discovery of novel drug targets[45-62]. Endogenous neurotransmitters also alter the function of these descending pain pathways based on different neurophysiological states, e.g., hunger, sleep, and stress[34,35]. vlPAG neurons control ascending pain signaling at the level of the spinal cord via intermediary adrenergic and serotonergic nuclei, including the LC and RVM, respectively[46,47]. The activity of vlPAG neurons is primarily controlled by glutamatergic and GABAergic inputs from areas like the hypothalamus, central amygdala, and anterior cingulate cortex[34,35]. Interestingly, vlPAG neuron populations differentially modulate nocifensive behaviors: either increasing activity of vlPAG glutamatergic or decreasing activity of vlPAG GABAergic neurons is antinociceptive[66–69].

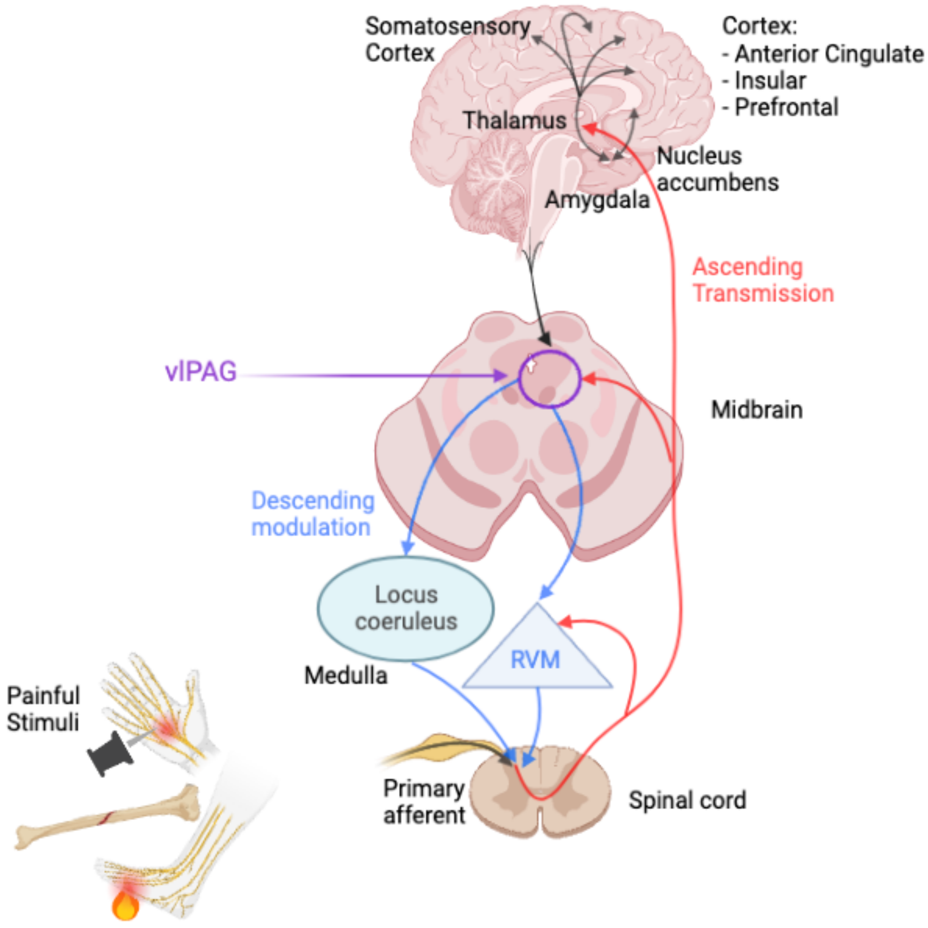

Figure 3: Ascending pain encoding and descending pain modulatory circuits. Adapted[34,35]

While not a focus of this thesis, we have identified that vlPAG neurons also encode pain anticipation (Accessory Figure 4). Pavlovian or operant learning of stimuli associated with pain experiences preferentially activate vlPAG neurons. For example, a tone preceding a noxious experience repeatedly can start eliciting a response from vlPAG neurons even when a painful stimulus is not applied. This response to tone persists even when the following noxious stimuli are removed. Additionally, through repeated operant training, mice can learn a context associated with pain experience. Furthermore, before mice enter the context associated with pain experience, vlPAG neurons show an anticipatory increase in activity. Not surprisingly, multiple human fMRI studies have found that placebo analgesia or anticipation of pain experiences strongly recruits the vlPAG[70,71]. Again, while not investigated in this thesis, future research exploring the contributions of baseline ACh in the learning phenomenon described here could yield significant insights into pain anticipation neurophysiology.

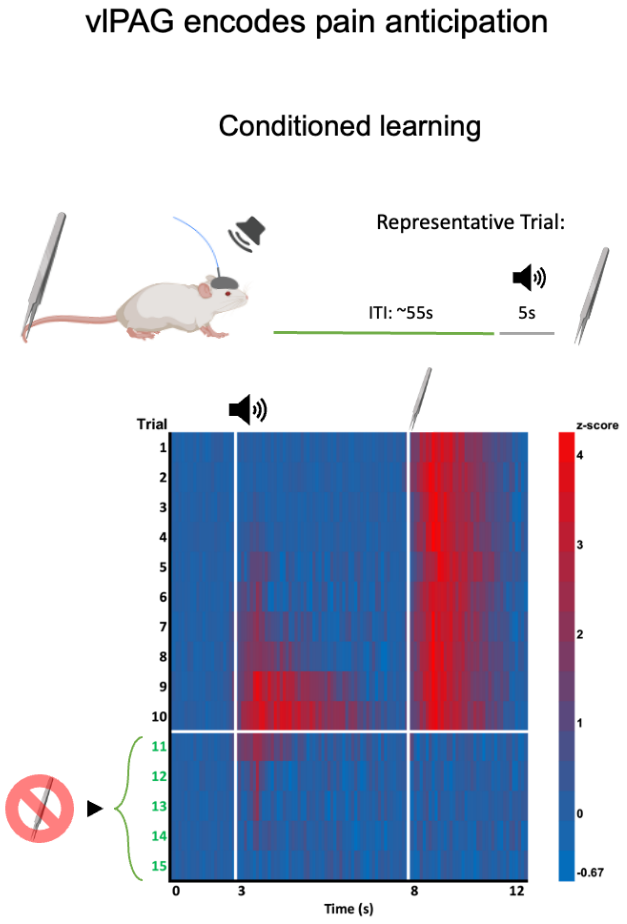

Figure 4: vlPAG activity during conditioned and operant learning.

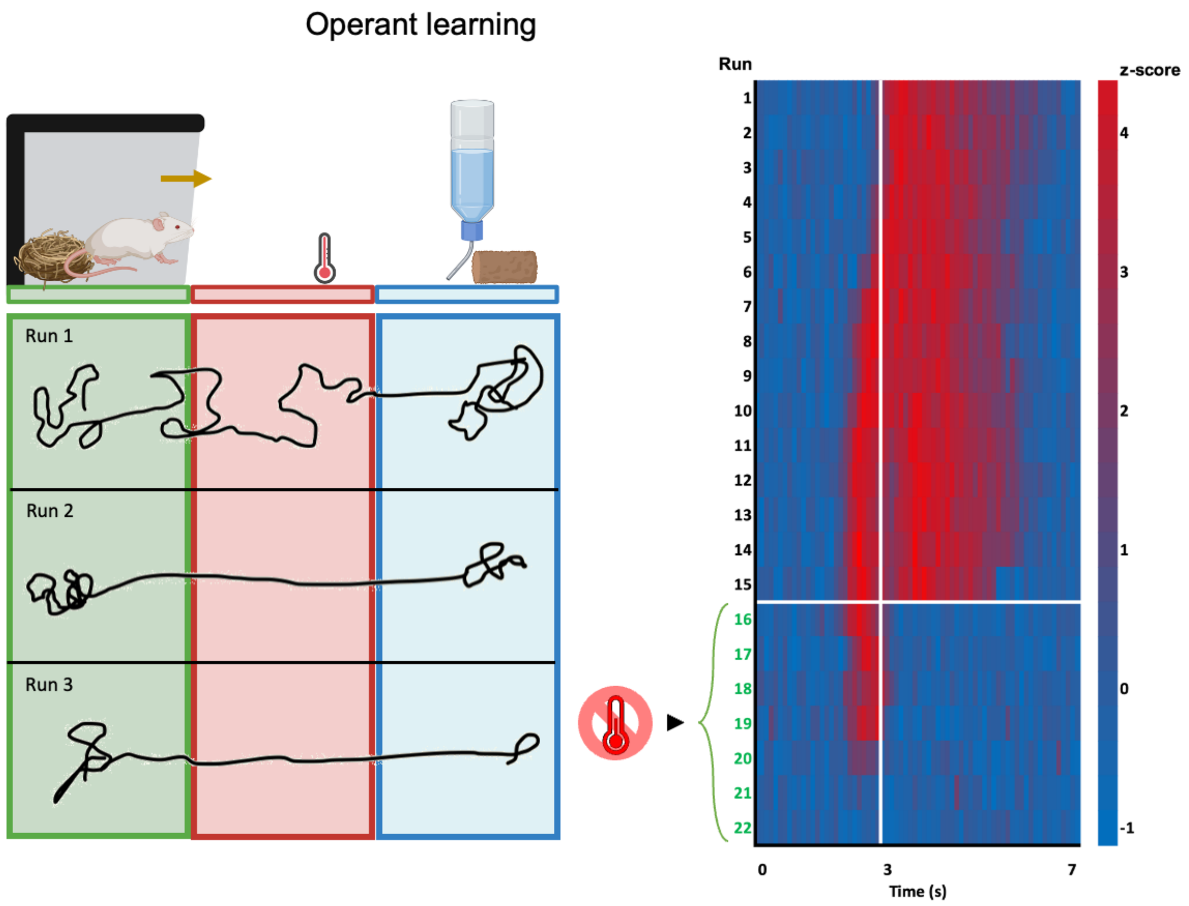

Figure 4 (continued): In conditioned learning assays (above), an auditory tone is played for 5s, and a noxious mechanical stimulus is applied at the end of the tone. GCaMP6-based intracellular Ca^{2+} levels are plotted across rows and color-coded according to z-score. Redder colors represent stronger activation of vlPAG neurons. From trial 11 onwards, the noxious stimulus following the tone was omitted.

In operant learning assays (below), the mice were placed in a three-chambered container that could be spontaneously traversed by the mice. The green chamber was constructed to mimic the mouse's home cage, the red chamber had a temperature-controlled hot plate as the bottom surface, and the blue chamber contained food and water. We then monitor the mice using an overhead camera for multiple hours while recording intracellular Ca^{2+} levels using GCaMP6 and fiber photometry. Over successive runs, the mouse learns that the middle chamber is hot, as evidenced by the shorter path length. The raster plot on the right represents vlPAG activity during the transition from the green to the red chamber. During the first run, we see an increased activity while the mouse is in the red chamber, which persists for a while. However, over successive runs, the increase in activity begins to precede the transition onto the hot plate, suggesting learning and anticipation of the pain experience. When we turn off the hot plate before run 16, we no longer observe the persistent activation of vlPAG neurons due to the heat. However, we still see the anticipatory rise in vlPAG activity before transitioning onto the red chamber. This anticipatory rise in vlPAG activity also disappears after 4-5 trials.

While the vlPAG plays additional roles, including fear memory, freezing behavior, passive coping strategies, and REM and NREM sleep, global electrical or chemogenetic activation of vlPAG is antinociceptive, emphasizing its importance in modulating pain[45-62]. Given these pain modulatory effects of the vlPAG, substantial efforts have attempted to identify neurophysiological mechanisms in the vlPAG that regulate pain. Opioid, cannabinoid, and immune receptors can strongly modulate vlPAG neuronal activity to change nocifensive behaviors[45-62]. Direct excitatory and inhibitory inputs from the orbitofrontal and anterior cingulate cortex and amygdala also alter vlPAG activity to modulate pain signaling[72–75]. Furthermore, neuromodulatory inputs from the hypothalamus and serotoninergic and norepinephrine inputs from dorsal raphe or locus coeruleus also modulate vlPAG activity to alter pain[74,76–82]. While not a focus of this thesis, the exact origin of endogenous opioid and cannabinoid signaling remains to be identified. These discoveries could mark a critical development in the field of endogenous pain modulation. Similarly, what all these inputs encode in a pain-independent manner needs to be further evaluated.

Initial studies identified the antinociceptive potential of the vlPAG using electrical stimulation in rats; subsequently, similar effects were demonstrated in other mammals, including humans[45-62]. Studies conducted in lightly anesthetized animals suggested three different populations of neurons in the descending pain modulatory pathways based on changes in activity during a noxious experience: On-cells (neurons that increase firing), Off-cells (neurons that decrease firing), and neutral cells (neurons that do not show a change in firing rate)[34,35,44]. However, work in unanesthetized, freely behaving animals has questioned this framework[83], further emphasizing the value of studying these systems in awake-behaving animals, a core guiding principle of this thesis.

Relationships between pain and acetylcholine

The strongest support for the pain modulatory effects of ACh comes from AChE inhibitors[84]. Donepezil produces dose-dependent analgesic effects when administered systemically in humans[84,85]. It is also a preventative migraine treatment. While substantial evidence exists for AChR expression and modulation of pain transmission through non-neuronal cells, e.g., macrophages, and peripheral ganglia or dorsal horn of the spinal cord, for this thesis, we will focus on the central, non-spinal, contributions of endogenous ACh. Briefly, elevating ACh in the spinal cord is antinociceptive, and decreasing it is pro-nociceptive, hyperalgesic and allodynic in rodent models[84,85]. These effects are primarily mediated through muscarinic receptors, though partial involvement of nicotinic receptors in contribution to the development of hyperalgesia might be possible. Analgesic effects of a subset of these AChRs may be possible.

In the CNS, ACh plays various roles (described earlier); however, cholinergic modulation of pain has not been well investigated[85]. This is surprisingly a missed opportunity, especially given the ascribed role of ACh as a neuromodulator that regulates plasticity and the substantial plasticity involved with the manifestation of a chronic pain state. AChE inhibitors, when administered in cerebroventricular spaces, are antinociceptive in animal pain models. The brain regions where cholinergic signaling in the context of pain has been explored include the cortex (S1, insular, cingulate, prefrontal), amygdala, and the medulla[84,85]. In the cortex, generally, muscarinic receptors have been shown to play pain-modulatory roles. In the somatosensory cortex, M1 mAChRs and presynaptic β2-subunit containing nAChRs contribute to increased pain sensitivity[84,85]. On the contrary, M1 AChRs have been shown to exert analgesic effects by increasing GABAergic drive in the anterior cingulate cortex[84,85]. In the insular cortex, M2 mAChRs have been shown to be analgesic[84,85]. In the mPFC, neuropathic states reduce nAChR and M1 mAChR expression to reduce neuronal excitability[84,85]. In the amygdala, both α7 nAChRs and mAChRs mediate antinociceptive effects by enhancing GABAergic transmission or reducing neuronal excitability[84,85]. In the medulla, α4β2 nAChRs strongly modulate neurophysiology to yield antinociceptive effects[84,85]. While mRNA and protein studies have demonstrated the presence of AChRs in vlPAG[86–89], the cell-types that express these AChRs and the extent to which endogenous cholinergic inputs act on these receptors to modulate pain has not been investigated. A central goal of this thesis is to systemically conduct a comprehensive assessment of AChR function in the vlPAG, explore their cellular phenotype, characterize overlap with μ-opioid receptor function, and identify the role of endogenous cholinergic inputs in the activation of these receptors.

Methodological innovations

While substantial conceptual innovation is evident, given that endogenous cholinergic signaling in the vlPAG and its modulation of pain have not been investigated previously, this thesis is also strongly supported by technological advances. This thesis has used cell-type and circuit-specific approaches to isolate the role of cholinergic inputs to vlPAG in pain modulation. To assess the contribution of specific AChR(s), we employed a combination of rigorous and high-throughput methods to assay mRNA expression along with precise protein function using brain slice electrophysiology. The fluorescence *in-situ* hybridization (FISH) assays facilitate rapid screening of AChRs and identification of cell-, receptor- and neurotransmitter phenotypes.

Behavioral pharmacology and circuit-specific optogenetics were used to monitor the impact of specific AChRs in antinociception and the possible interactions between cholinergic and opioid pathways. The development and availability of genetic mouse lines allow these experiments to causally link cholinergic activity, vlPAG, and pain, using a variety of somatic and affective pain assays. Additionally, the use of the novel ACh sensor -GRAB$_{\text{ACh 3.0}}$ - and intracellular Ca^{2+} probes (GCaMP6) for *in vivo* fiber photometry experiments allows unprecedented insights into cholinergic signaling in the vlPAG. Furthermore, *in vivo* 2-photon imaging provides new mechanistic insights into the development of chronic pain states. The use of computational models to gather mechanistic insights into pain encoding by vlPAG neurons is also a methodological innovation.

Summary

In this thesis, we assayed extracellular ACh release dynamics under acute and chronic pain conditions using the novel ACh biosensor - GRAB$_{\text{ACh 3.0}}$[90]. Using anatomical and optogenetic approaches, we identify the source of ACh in the vlPAG and test how altering ACh levels in the vlPAG relieves somatic and affective aspects of acute and chronic pain. Following these optogenetic investigations, we identify the receptor and intracellular signaling that mediates the analgesic effects of these cholinergic projections. These investigations are also accompanied by electrophysiological and *in vivo* testing of chronic pain-induced synaptic and intrinsic plasticity in the vlPAG. Additionally, we explore how these AChRs lead to the activation of descending projections to the RVM to relieve pain in opioid-tolerant animals. Finally, using an in vivo 2-photon ensemble imaging approach, we monitor neural activity in the vlPAG to explore the neuropathic pain-induced progression of aberrant neuronal dynamics in the vlPAG and test how opioids, development of opioid tolerance and cholinergic modulation alters these pathophysiological neuronal activity patterns. Together, these investigations ultimately lend insights into a novel circuit and receptor target that relieves chronic pain despite opioid tolerance, without evidence of withdrawal symptoms, reward profile, or the development of analgesic tolerance. While outside the scope of this thesis, it would be of immense clinical value to test the pain-altering effects of α7 nAChR targeting compounds, including: 1. EVP-6124 (Enicline), 2. Tropisetron, and 3. PNU-120596 (a positive allosteric modulator of α7 nAChRs).

Graphical Abstract

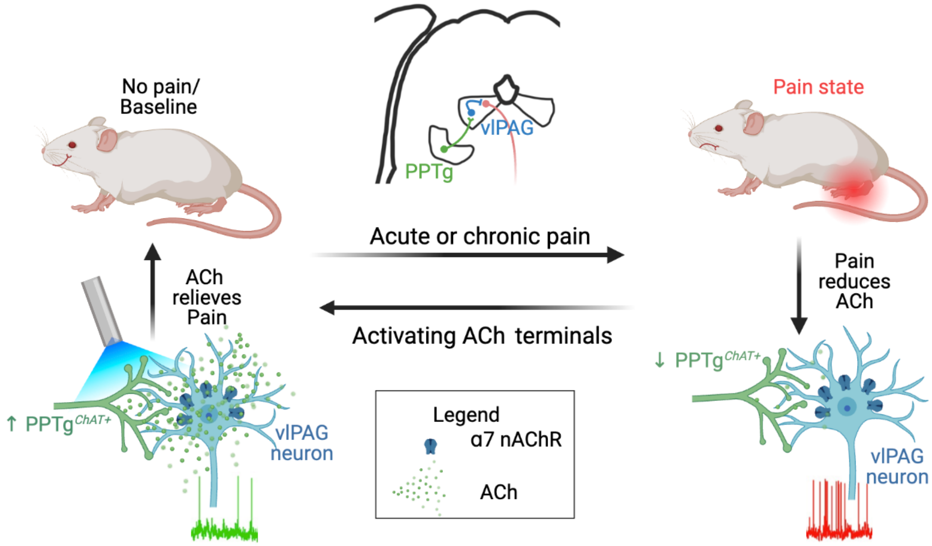

Figure 5: Graphical abstract

Methods

Animals

All procedures were conducted in accordance with the NIH guide for the care and use of laboratory animals, the American Veterinary Medical Association guidelines, and the guidelines from the International Association for the Study of Pain. The use of laboratory animals was approved by the Institutional Animal Care and Use Committee at the University of Chicago. Adult (>8 weeks, 25–35 g) male and female *WT* (C57BL6/J, Jackson labs), *ChAT-Cre* (Strain number: 006410, Jackson Labs), *Chrna7-Cre* (Strain number: 034808-UCD, MMRRC), *Oprm1-Cre* (gift of Julie Blendy, University of Pennsylvania), *Gad2-Cre* (Strain number: 010802, Jackson Labs) and *ChAT-Cre*::*Chrna7-Cre* were used in this study. These mice were bred at the University of Chicago. *Cre* expression specificity was verified using mRNA and immunohistological approaches for *ChAT-Cre* and *Gad-Cre* mouse lines, and mRNA and electrophysiological approaches for *Chrna7-Cre* and *Oprm1-Cre* mouse lines. The *ChAT-Cre*::*Chrna7-Cre* mouse line was verified by the absence of *Chrna7* mRNA in PPTg, *ChAT* mRNA in the vlPAG, and expression of *Cre* mRNA in *Chrna7* mRNA expressing vlPAG neurons and *ChAT* mRNA expressing PPTg neurons. All experiments were conducted in mice that were heterozygous for the *Cre* allele. Mice were group-housed with littermates of the same sex (2-5 animals per cage), given access to food and water *ad libitum*, and maintained on a 12 hr:12 hr light:dark cycle (lights on at 6:00 AM) at 23±1°C. Behavioral assays were conducted during the light cycle. All animals were monitored for gross health status daily for the entirety of the study. For *in vivo* experiments, we used randomly assigned age- and sex-matched litter-mate controls in experimental and control groups. All experiments were replicated in at least one additional independent group. Experimenters were blinded to the viral injection of the experimental groups for all optogenetic experiments. Optogenetic and behavioral experiments consisted of 5–11 mice per group, and *in vivo* and *ex vivo* physiology experiments consisted of 3-7 mice per group. Exact animal numbers are provided in the figure legends. ANOVA was conducted to test for interaction between sex differences in antinociceptive effects of optogenetic inhibition of vlPAG$^{Chrna7+}$ neurons and optogenetic excitation of PPTg^{ChAT+}→vlPAG neurons. However, statistical significance for the interaction term was not observed. Therefore, male and female mice were combined in the final groups for the remainder of the study. Animals were excluded only after post-hoc validation for virus expression and fiber optic placements. Multiple acute somatic pain assays were conducted within the same cohort. However, tonic, chronic, and affective pain assays were conducted in separate cohorts.

Surgeries

Stereotaxic injections and surgical procedures

All surgeries were conducted under aseptic conditions, and all surgical tools were sterilized using a glass bead sterilizer (FST sterilization tool 18000-45). A small animal stereotaxic surgery device (Kopf Instruments) was used to position viral injections and fiber-optic implants. Mice were anesthetized with isoflurane (2% induction, 1-1.5% maintenance), shaved using a trimmer, and placed on the stereotaxic apparatus. Body temperature was maintained at 37°C using a homeothermic heating pad (Harvard Apparatus). An ophthalmic ointment was used to maintain eye lubrication throughout the duration of the surgery. Prior to the incision, mice were administered buprenorphine (Hospira, 0.05 mg/kg, s.c.) and bupivacaine (Hospira, 1 mg/kg s.c. at the site of incision). The surgery site was sterilized with betadine solution, and an incision was made on the top of the skull using surgical blades. A Foredom micromotor drill was used with a drill bit (Kyocera 105-0210L310) to drill a hole (~600-800µm diameter) in the skull. Care was taken to prevent bleeding, and sterilized cotton tip applicators were used to limit any bleeding that occurred. A blunt Hamilton syringe (1700 series, 33G) was used for all viral and fluorescent microsphere injections. The injection volume and flow rates were controlled using a syringe pump (World Precision Instrument, UMP3T). For viral and microsphere injections, 400 nL fluid was injected at a rate of 150 nL/min unless otherwise stated. After the injection needle reached the target DV location, the needle was gently moved dorsoventrally for ~50µm to create a 'pocket' for viral injection. After injection, the needle was held in place for ~7mins to ensure adequate viral diffusion and minimize viral solution from being suctioned up due to backpressure while removing the needle. The injection needle was slowly withdrawn 5-10 min after the end of the infusion.

Injection coordinates in mm relative to Bregma for various brain regions were: vlPAG - AP: -4.75, ML: 0.55, DV: -2.70; PPTg - AP: -4.60, ML: 1.10, DV: -3.50; LDTg - AP:-5.20, ML:0.50, DV:3.5; RVM - AP: -5.70, ML: 0.00, DV: -5.90. The coordinates were scaled based on the length variations of the AP distance between the Bregma and the Lambda. This distance was divided by 4.21 (standard distance), and the ratio was used to scale the coordinates.

For photometry and optogenetics experiments, fiber optic cannulas (MFC_400/430-0.48_5mm_MF1.25_FL, Doric) were implanted using a cannula holder stereotaxic attachment (Kopf Instruments). Cannulas were lowered into the brain at a rate of 300 µm/min. Two skull screws (0-80 1/16, PlasticsOne) were affixed to separate plates of the skull and dental cement (Lang Dental) was used to affix the cannulas and the skull, and the screws to form a headcap. Cannula placement coordinates in mm relative to Bregma are as follows: vlPAG: AP: -4.75 AP, ML: 0.55, DV: -2.50; PPTg: AP: -4.60, ML: 1.10, DV: -3.30. Post-surgery, 0.5mL sterile saline and Meloxicam (Sigma, 5 mg/kg, s.c.). Animals were placed on a heating pad and monitored until they fully recovered from the anesthetic. Mice were allowed to recover, and the virus was allowed time to express for three weeks before behavioral assays. Injection coordinate choices for PPTg and vlPAG were guided by preliminary anatomical experiments exploring the density of cholinergic innervation in the vlPAG.

Viral approaches for anatomical tracing, immunohistochemistry, and slice electrophysiology

For retrograde labeling of cholinergic inputs to vlPAG, we injected 200nL of retrogradely transported virus AAVrg-CAG-DIO-tdTomato (Addgene: 28306) unilaterally into the vlPAG of *ChAT-Cre* mice. For retrograde labeling of inputs to the vlPAG for immunohistochemical analysis, 200nL of fluorescent microspheres (FluoSpheres Carboxylate-Modified Microspheres, dark red fluorescent, 660/680, Fisher Scientific, F8783, diluted 1:4 in saline) were injected unilaterally into the vlPAG of WT mice. To label PPTg^{ChAT+} terminals in vlPAG, in a *ChAT-Cre* mouse line were unilaterally injected 200nL of AAV1-phSyn1-Flex-tdTomato-T2A-SypEGFP (Addgene: 51509) into the PPTg. To label vlPAG$^{Chrna7+}$ neurons for slice electrophysiology recordings, AAV9-hSyn-DIO-mCherry (Addgene: 50459) was injected bilaterally into the vlPAG of *Chrna7-Cre* mice. For electrophysiological recordings of vlPAG→RVM projections, AAVrg-CAG-tdTomato (Addgene: 59462) was injected into the RVM of *Chrna7-Cre* mice. In a subset of these experiments, we also injected AAV9-Ef1a-DIO-ChR2-EYFP (Addgene: 20298) in the vlPAG to optogenetically activate vlPAG$^{Chrna7+}$ neurons while recording from vlPAG→RVM projecting neurons. In slice electrophysiology experiments that tested cholinergic synaptic transmission from PPTg^{ChAT+}→vlPAG, we injected AAV9-EF1a-DIO-ChR2-mCherry (Addgene: 20297) bilaterally in the PPTg of *ChAT-Cre* mice. To test GABAergic synaptic transmission from vlPAG$^{Chrna7+}$ neurons to neighboring vlPAG neurons, AAV9-EF1a-DIO-ChR2-mCherry was injected bilaterally into the vlPAG.

Viral injections and cannula implants for behavioral optogenetic assays

To optogenetically inhibit vlPAG^{Oprm1+} neurons, we injected AAV9-EF1a-DIO-eNpHR3.0-EYFP (Addgene: 26966) in the vlPAG of *Oprm1-Cre* mice and implanted an optical cannula in vlPAG. To optogenetically excite PPTg^{ChAT+}→vlPAG terminals, we injected AAV9-EF1a-DIO-ChR2-mCherry in the PPTg of *ChAT-Cre* mice and implanted an optical cannula in the vlPAG for terminal excitation. A similar method was employed to optogenetically activate LDTg^{ChAT+}→vlPAG terminals, but the virus was injected in the LDTg instead of PPTg. In these surgeries, we implanted the cannula ipsilateral to the viral injection site. For optogenetic manipulation of vlPAG$^{Chrna7+}$ activity, a *Chrna7-Cre* mouse line was used, AAV9-Ef1a-DIO-eNpHR3.0-EYFP or AAV9-EF1a-DIO-ChR2-mCherry was injected, and an optical cannula was implanted into the vlPAG to inhibit or excite, respectively. For optogenetic manipulation of vlPAG^{Gad+} neurons, a *Gad-Cre* mouse line was used, and AAV9-Ef1a-DIO-eNpHR3.0-EYFP or AAV9-Syn-DIO-ChrimsonR-tdTomato (UNC Vector Core) was injected, and an optical cannula was implanted into the vlPAG to inhibit or excite, respectively. Unless otherwise stated, AAV9-hSyn-DIO-EYFP (Addgene: 27056) was used as a control probe for behavioral experiments. For optogenetic experiments, the optical fiber was implanted ~100-150 µm above the virus injection site.

Viral injections and cannula implants for fiber photometry assays

To monitor the activity of vlPAG^{Oprm1+} neurons, in an *Oprm1-Cre* mouse line, we injected AAV9-Syn-DIO-GCaMP6m (Addgene: 100838) and implanted an optical cannula into the vlPAG. Similar approaches were used to monitor the activity of vlPAG$^{Chrna7+}$ and vlPAG^{Gad+} neurons using fiber photometry using *Chrna7-Cre* and *Gad-Cre* mouse lines, respectively. To monitor ACh levels in vlPAG, in WT mice, we injected AAV9-hSyn-ACh4.3 (GRAB$_{\text{ACh 3.0}}$, WZ Biosciences) and implanted an optical cannula into the vlPAG. For photometry experiments, the optical fiber was targeted ~100-150µm above the virus injection site.

Viral injections and cannula implants for simultaneous fiber photometry and optogenetic assays

To simultaneously activate PPTg^{ChAT+}→vlPAG terminals in the vlPAG and monitor the activation-induced ACh release, in *Chat-Cre* mice, we injected GRAB$_{\text{ACh 3.0}}$ in the vlPAG and *Cre*-dependent ChrimsonR in the PPTg. The optical cannula was implanted in the vlPAG. To simultaneously activate PPTg^{ChAT+}→vlPAG terminals while monitoring the activity of vlPAG$^{Chrna7+}$ neurons, in *Chat-Cre*::*Chrna7-Cre* mice, we injected *Cre*-dependent ChrimsonR in the PPTg and *Cre*-dependent GCaMP6m in the vlPAG. The optical cannula was implanted in the vlPAG. To simultaneously activate vlPAG$^{Chrna7+}$ neurons while monitoring the neuronal activity of vlPAG→RVM projection neurons, in *Chrna7-Cre* mice, we injected *Cre*-dependent ChrimsonR in the vlPAG and AAVrg-Syn-jGCaMP7s (Addgene: 104487) in the RVM. The optical cannula was implanted in the vlPAG.

Viral injections and drug infusion cannula implant for opto-pharmacology assays

For focal drug infusion combined with optogenetic stimulation of PPTg^{ChAT+}→vlPAG terminals, we expressed *Cre*-dependent ChR2 in the PPTg in *Chat-Cre* mice and implanted a guide cannula into the vlPAG. A focal infusion and optical cannula (OmFC, Doric) was implanted through the guide cannula to optogenetically stimulate terminals after drug infusion in the same location. Optogenetic stimulation was conducted 15 mins after drug infusion.

Viral and GRIN lens approaches for in vivo imaging assays

For calcium imaging experiments, WT mice were injected with Dexamethasone (0.6mg/kg, Sigma-Aldrich, D1756) before anesthesia for surgery to minimize lens implantation-induced tissue swelling and inflammation. We performed a craniotomy using a trephine (Fine Science Tools, 18004-18) to create a ~1.5 mm diameter hole in the skull. We carefully removed the dura using a bent 30G syringe needle and irrigated the brain surface with sterile aCSF to prevent drying. We then injected 350nL of AAV9-Syn-GCaMP6m in the vlPAG at a rate of 50nL/min in two locations in mm relative to Bregma: AP: -4.75, ML: 0.65, DV: -2.80 and DV: -2.4. These locations are slightly lateral, dorsal, and ventral to the final GRIN lens implantation site. These injection locations were chosen because preliminary experiments suggested that the area above the injection track displayed strong autofluorescence, presumably due to tissue inflammation or death. To allow for viral diffusion, the syringe was removed 10 mins after the injection. Before implanting the grin lens, incisions in a cross-pattern were made on the brain's surface using a surgical blade. GRIN lens (0.6 mm diameter, 7.3mm length, Inscopix, 1050-004597) was implanted using a GRIN Lens holder (RWD Life Science, 998-00201-00) at a rate of 0.15 mm/min. The lens was retracted 200 µm every 1 mm of implantation to allow the tissue to settle around the lens. The GRIN lens was placed ~100–300 µm above the imaging plane. SRO accolade (Zest Dental Solutions) was applied to the base of the GRIN Lens and was cured for 2 mins with a high-intensity UV LED (SDI). The lens was bonded to the skull with adhesive cement (C&B, S380 Metabond Quick Adhesive Cement System) and allowed to harden. Three skull screws were inserted on three separate skull plates to form a triangular pattern around the lens. The lens holder was then removed, and dental Cement (Zest Dental) was applied to the surrounding area of the skull, covering the skull screws. A titanium head plate 4 cm x 1 cm with a 0.75 cm diameter hole was affixed to the head cap with the hole centered above the GRIN Lens. Kwik Cast Silicone Sealant (WPI) was used to fill the hole and cover the GRIN Lens for protection. Animals were monitored daily for changes in health and weight.

After experiments, all animals were checked for the location of viral injection and cannula placement using histological methods and confocal imaging. Animals with inappropriate viral or cannula placement were excluded from the analysis.

Slice electrophysiology

After viral injections and behavioral assays, mice were deeply anesthetized using isoflurane (Baxter). After checking breathing rate (~1 breath per sec) and for lack of nocifensive responses, mice were transcardially perfused using an ice-cold NMDG-slicing solution (~20ml), containing: 92 mM NMDG, 2.5 mM KCl, 1.25 mM NaH_2PO_4, 30 mM $NaHCO_3$, 20 mM HEPES, 25 mM glucose, 2 mM thiourea, 5 mM Na-ascorbate, 3 mM Na-pyruvate, 0.5 mM $CaCl_2·4H_2O$, and 10 mM $MgSO_4·7H_2O$. pH was titrated to 7.3–7.4 with concentrated HCl, and osmolarity was measured to be 300–310 mOsm. After perfusion, the mice were decapitated, and the brains were extracted, dissected, and sliced in the same ice-cold NMDG slicing solution bubbled continuously with 95%-O_2/5%-CO_2.

Acute midbrain coronal slices (250μm thick) containing the vlPAG were taken on the vibratome (VT100S, Leica). These slices were transferred to NMDG solution at 32°C for <12 mins. Then these slices were transferred to HEPES-containing recovery solution, which contained: 92 mM NaCl, 2.5 mM KCl, 1.25 mM NaH_2PO_4, 30 mM $NaHCO_3$, 20 mM HEPES, 25 mM glucose, 2 mM thiourea, 5 mM Na-ascorbate, 3 mM Na-pyruvate, 2 mM $CaCl_2·4H_2O$, and 2 mM $MgSO_4 \cdot 7H_2O$. In the HEPES solution, slices rested for at least 60 mins before each recording. From each animal, 2-3 vlPAG slices were used for experiments. Opsin and fluorophore-containing slices were kept under an optically opaque wrap.

For electrophysiological recordings, the slices were transferred to an upright microscope (Axioskop, Zeiss). Neurons were visualized under infrared illumination with a 40x water-immersion objective equipped with infrared-differential interference contrast (IR/DIC) and epifluorescence video microscopy. A light source (XCite, Excelitas) coupled to excitation filters (470/40 nm and 560/40 nm bandpass) through the fluorescent port of the microscope was used to search for fluorescent neurons and optogenetic activation of opsins including ChR2, ChrimsonR, or eNpHR 3.0 with light pulses. Light pulses were triggered by pCLAMP via TTL pulses to a shutter (LS2, Uniblitz) through the Master-8 interface (A.M.P.I.). Optical power intensity through the microscope objective was set to ~4mW/mm^2 using a photodiode power sensor (S120C, Thor Labs). Optical pulse duration and frequencies were guided by *in vivo* experiments and pilot data collected using slice electrophysiology. Retrogradely or virally labeled neurons were visualized using fluorescence microscopy, and the patch pipette was guided to the neurons for whole-cell/cell-attached recordings using simultaneous GFP/tdTomato fluorescence and DIC illumination. This combined visualization was critical when recording from vlPAG, and PPTg neurons, given that cell morphology was challenging to visualize using DIC illumination in these brain regions.

Recording external solution, artificial cerebrospinal fluid (aCSF) contained: 119 mM NaCl, 2.5 mM KCl, 1.25 mM NaH_2PO_4, 24 mM $NaHCO_3$, 12.5 mM glucose, 2 mM $CaCl_2 \cdot 4H_2O$, and 2 mM $MgSO_4 \cdot 7H_2O$ superfused at ~2 ml/min. The intracellular recording solutions contained: 145 mM K-Gluconate or Cs-Gluconate (if monitoring synaptic currents), 10 mM HEPES, 1 mM EGTA, 2 mM Mg-ATP, 0.3 mM Na_2-GTP, and 2 mM $MgCl_2$ (pH 7.3 adjusted using Tris base, osmolarity of 290–300 mOsm adjusted using sucrose). These experiments were performed at room temperature (~23°C). Intracellular or external aCSF solutions were backfilled in the recording pipettes for whole-cell or cell-attached recordings. After recording, slices were fixed in PFA to confirm injection location and viral expression using confocal microscopy. If the majority of viral expression was outside the intended region, the data were excluded from the analysis.

Signals were amplified with a Multiclamp 700A/Axopatch 200B amplifier, digitized with Digidata 1440A, and controlled with pCLAMP 9 software (Molecular Devices). Data were sampled at 10 kHz and low pass filtered at 1 kHz. Whole-cell patch-clamp recordings were achieved with borosilicate patch pipettes containing the microelectrode (3–6 MΩ) pulled on a Flaming/Brown micropipette puller (model P-97, Sutter Instrument, Novato, CA). Patch pipettes with higher resistance (5-7 MΩ) were used for cell-attached recordings to minimize accidental whole-cell access. In circumstances when cell-attached recordings transitioned to whole-cell recordings, the data were discarded.

To isolate and identify the neurotransmitters mediating optogenetically evoked synaptic currents, we used the following antagonists as necessary: CNQX (20μM), bicuculline (20μM), MLA (10nM), Atropine (1μM), α-bungarotoxin (100nM). Where necessary, DMSO or Kolliphor HS 15 were used to dissolve drugs, and control solutions contained the same diluent concentrations. Only one cell from each slice was recorded for experiments that required drug perfusion. The recorded optically-evoked post-synaptic currents (oPSCs) had short constant latency, suggesting the monosynaptic nature of these synaptic responses. For these oPSC measurements, the variance in 10 oPSC rise-time was monitored. The approximate latency was ~7 ms. To monitor the effects of α7 nAChR activation on vlPAG$^{Chrna7+}$ neuronal physiology, EVP-6124 (2 nM) was bath perfused. This concentration was chosen given the known pharmacokinetics of EVP-6124 in mice.

Cell-attached recordings of action potential frequency were conducted in on-cell configuration with a ~GΩ seal resistance in voltage clamp (0mV) mode with aCSF in the patch pipette. Data were excluded if any run-down was observed during the recording. For cholinergic receptor synaptic communication, cells were held at -70mV in whole-cell voltage clamp mode. For GABAergic synaptic transmission, cells were held at 0mV. Response sizes of oPSCs were calculated by baseline-subtracting and averaging 10 traces together, then calculating the peak amplitude in a 20ms window after the light pulse. When monitoring sEPSCs and sIPSCs, the currents were separated using -70mV and 0mV holding potentials, respectively. Spontaneous synaptic events were detected using MATLAB's *findpeaks* function with prominence >3 median absolute deviation of baseline noise, roughly corresponding to 5 pA amplitude, <0.75 ms rise time, and >3 RMS noise picocoulomb charge transfer as calculated using the area under the curve, roughly resulting in events lasting longer than 5ms. Identified sEPSCs and sIPSCs were cross-verified using Easy Electrophysiology software and visually verified by the experimenter.

When testing for the involvement of the PPARα signaling cascade, GW6471 (100nM) was included in the HEPES solution and aCSF to preincubate the slices and block the PPARα signaling cascade well before activation of α7 nAChRs using EVP-6124. The on-cell action potential firing rates were quantified by threshold crossing using MATLAB's *findpeaks* function and visually verified. These were binned according to described time intervals and normalized to baseline where necessary. Following stable 5 min whole-cell recordings, drugs or optogenetic stimulation effects were tested. In a subset of experiments, we expressed ChR2-mCherry on vlPAG$^{Chrna7+}$ neurons to use optogenetic stimulation after EVP-6124 induced a decrease in firing rate to test for neuronal action potentials.

For whole-cell excitability experiments, cells were recorded in current-clamp configuration and were allowed to stabilize for 5-10 min after establishing whole-cell access. Action potential voltage and current thresholds were calculated based on the first spike elicited by a slow current ramp protocol performed in the current-clamp configuration (200pA over 250ms). The spike threshold was calculated as the first voltage value corresponding to the time derivative of the voltage trace greater than 5mV/ms.

To calculate the relationship between firing rate and current injection, the number of action potentials were counted per current step, using 25pA increments of 1s duration. Input resistance was assessed by injecting a negative current step of -50pA for a 500ms duration.

In measurements of chronic pain-induced changes in cellular excitability, mice were sacrificed five days after CFA or saline injection in the hind paw. CFA or saline administration was counterbalanced within littermates. CFA's hyperalgesic effects were behaviorally verified on the day before electrophysiological recordings.

Data were only included from recordings with series resistance <30 MΩ and where input resistance or series resistance varied <25%. All batches of virally administered opsins employed in the study were functionally tested using slice electrophysiology. Data were primarily analyzed using Clampfit (Molecular Devices) and custom scripts in MATLAB. We aligned the data when the perfusion was switched to the drug-containing aCSF or other manipulations instead of the peak of monitored effects. All chemicals were purchased from Tocris or Sigma. The number of cells and animals employed for each experiment are included in the figure legends.

Optogenetics

For optogenetics experiments, mice were tethered to an optical fiber cable with an inbuilt rotary joint (RJPFL4 outer diameter 1.25mm, core diameter 400µm, ThorLabs). To activate eNpHR 3.0 opsin, we used a 595 nm LED (Thorlabs, M595F2) to deliver constant orange light. To activate ChR2, we used pulsed blue light (473nm) delivered using a DPSS laser (Shanghai Laser & Optics Century Co., Ltd.). Pulses were triggered using Master-9 Pulse Stimulator (A.M.P.I.). To activate ChrimsonR, we used 595 nm LED pulsed using LED Driver and Doric Synapse Studio (Doric systems). Unless otherwise stated, we used 20Hz pulse frequency and 10ms pulse duration for pulsed opsin activation. In all optogenetic experiments, the light at the tip of the cannula was adjusted to ~5mW (10mW/mm^2) peak power at the desired wavelength using a power meter (Thorlabs, PM20A).

All behavioral assays were conducted four weeks after viral and cannula surgeries within a sound-attenuated room at ~23°C. The animals were acclimatized and habituated to the experimental room, experimenter handling, and optical tethers in their homecage for at least 30 mins during the five days prior to the start of experiments. On the day of the experiments, the animals were habituated to the experimental rooms for at least 30 mins before the experiments. Unless otherwise stated, PPTg^{ChAT+}→vlPAG projections were stimulated for 10 mins before acute pain assays. vlPAG$^{Chrna7+}$ and vlPAG^{Oprm1+} neurons were activated or inhibited immediately before the acute pain assay. Recovery was conducted on the subsequent day for all experiments to prevent the residual effects of optogenetic or drug manipulations. Mice were tethered to the optical cables during the baseline and recovery assays. The behavioral apparatus was cleaned with a 70% alcohol solution and dried after each session. Experimenters were blinded to opsin or control fluorophore expression. Movements were video recorded using a camera (Basler) and Ethovision XT-16 software (Noldus) for later verification as necessary. During combined optogenetics and real-time place preference assay, the lasers were triggered based on Master-9 output, which occurred when the mice were detected within the optogenetic stimulation-paired chamber. The real-time location of mice was detected using a camera (Basler) interfaced with a computer (Dell Computers) running Ethovision XT-16 (Noldus). Ethovision sent a TTL output using Noldus IO box to the Master-9 pulse generator based on mouse location. In our experiments, we did not observe an interaction tested by repeated-measures ANOVA in antinociceptive effects and the laterality of the paw in vlPAG$^{Chrna7+}$ optogenetic inhibition or PPTg^{ChAT+}→vlPAG terminal excitation experiments. Hence, we pooled the data obtained from both hind paws. Mechanical thresholds or thermal latencies were measured three times for each mouse.

We used ex vivo slice electrophysiology and in vivo fiber photometry to verify opsin function and assess action potential fidelity. For ChR2 and ChrimsonR, optogenetic 10ms pulses at 1, 2, 4, 8, 16, 20, and 40 Hz were tested using slice electrophysiology in the expected neuron type. eNpHR 3.0 was tested using continuous 1s pulse delivery after step current injections that induced action potentials. ChrimsonR and eNpHR 3.0 were tested *in vivo* using GCaMP6 and GRAB$_{\text{ACh 3.0}}$. We observed that eNpHR 3.0 reliably decreased spontaneous GCaMP6 dynamics during continuous light delivery, and ChrimsonR increased GCaMP6 fluorescence in *Oprm1-Cre*, *Gad-Cre,* and *Chrna7-Cre* mice experiments and increased ACh release in the vlPAG in a frequency-dependent manner in *ChAT-Cre* mice. 10ms pulses at 1, 2, 4, 8, 16, 20, and 40Hz were tested for ChrimsonR. For behavioral opto-pharmacology, we injected the antagonists of the tested AChR 15 mins before optogenetic stimulation in both focal and systemic antagonist assays. The recovery and subsequent AChR antagonist assays were conducted 1 and 2 days after antagonist infusion.

Each viral lot was tested at least once using slice electrophysiology and immunohistochemistry to verify function and expression in the appropriate neuronal phenotype. Post experiments, the viral expression cell type and cannula placement were tested in all experimental animals.

Fiber photometry

A TDT-Doric system was used for our fiber photometry experiments with a lock-in amplifier and processor to drive and demodulate signals (TDT RZ5P). The experimental setup allowed us to simultaneously deliver 405 nm, 465 nm, and 594 nm light and monitor 525 nm light using a 5-port fluorescent minicube (FMC5_IE(400-410)_E(460-490)_F(500-540)_O(580-680)_S, Doric). The monitored light was sent to a femtowatt photodetector (Newport Model 2151), which sent the electrical signals to the RZ5P processor for demodulation. The setup allowed the monitoring of both calcium-dependent and independent signals using different modulation frequencies. Excitation light with a wavelength of 465 nm was 'Calcium dependent' and modulated at 331Hz, and isosbestic control calcium-independent 405 nm wavelength light was modulated at 211 Hz driven using LEDs and an LED Driver from Doric. The output power for individual wavelengths was ~20 µW as measured using a power meter (Thorlabs, PM20A). Since the signal was sampled at 1017.3 Hz, we ensured that no signal was modulated at a frequency greater than half the sampling frequency to prevent aliasing errors. The receiver power levels for the demodulated signal were matched for the calcium-dependent and independent signals. Matching power levels required ~5x light power output from the 405 nm LED. The demodulated signal was low pass filtered at 20 Hz at sixth order. Animals were tethered to a patch cord (0.48NA, 400 µm core diameter, Doric) using a freely pivoting rotary joint and gimbal holder (Doric Lenses). Synapse software (TDT) was used to interface with the RZ5P system to log data, timestamp events using TTL loggers, and control the LEDs. The 595nm wavelength LED (Thorlabs) for activating ChrimsonR, or eNpHR 3.0, was driven using Thorlabs LED driver and interfaced directly with the RZ5P system and Synapse software to deliver precise time-locked stimulation. To inhibit neurons using eNpHR 3.0, we continuously delivered the 595nm LED light. To activate neurons using ChrimsonR, we pulsed 595nm light at a frequency of 20Hz and pulse duration of 10ms unless otherwise stated. During experiments where we activated PPTg^{ChAT+}→vlPAG terminals while monitoring vlPAG$^{Chrna7+}$ neurons, we conducted RHS assays every 3 mins to correlate changes in pain sensitivity and vlPAG$^{Chrna7+}$ neuronal activity induced by PPTg^{ChAT+}→vlPAG terminal activation. When monitoring vlPAG → RVM projection neurons while activating vlPAG$^{Chrna7+}$ interneurons, 595nm LED was pulsed at 20Hz with a pulse duration of 10ms. For these opsin activation experiments, the peak power output for opsin activation was ~5mW (10mW/mm^2).

Habituation to the apparatus and cleaning between tests was identical to the optogenetic experiments above. Generally, individual photometry sessions lasted ~30 mins. Baseline spontaneous fluorescence activity was recorded during open-field behavior, where the movements of the mice were recorded using an overhead camera (Basler). We did not find the movement duration, velocity, or distance correlated with any of the photometry signals that we monitored. Indeed, a recent paper has demonstrated that activating or inhibiting PPTg^{ChAT+} neurons does not alter movement. Stimuli-evoked behaviors, and the associated changes in neuronal activity, were captured using two orthogonally positioned cameras allowing for a temporal precision of ~16ms. When monitoring responses of vlPAG$^{Chrna7+}$ neurons to noxious and salient stimuli, the test stimuli were presented in groups, and a minimum of 30 mins were given between testing of different stimuli.

The data were analyzed using MATLAB according to published protocols. First, the first 5-secs of the recording were removed due to observed opto-electrical artifacts that could contaminate the fit parameters. The photo-bleaching of GCaMP over long sessions was removed using a double exponential fit to the entire dataset. We subtracted the calcium-independent signal from the calcium-dependent signal to reduce movement or hemodynamic artifacts. To that end, a smoothed 405 nm isosbestic signal was fitted to the 465 nm signal using linear regression to obtain fitting coefficients[91,92]. Care was taken to ensure that the fitting coefficients agreed with expectations, i.e., no erroneously negative coefficients existed, and unique outliers did not dominate the fit. In instances where the patch cord came loose during recordings, data were analyzed in separate epochs where the patch cord was connected optimally to ensure consistency of the regression coefficients. Using the fitting coefficients, the 'fit 405nm' signal was calculated, subtracted, and divided from the 465nm signal to obtain a ΔF/F ($=[F_{465}-F_{fit405}]/F_{fit405}$). A robust Z score based on the median ΔF/F was calculated for the concatenated ΔF/F data for all sessions for individual mice to facilitate comparison across mice and sessions. This robust z-score was calculated by first removing the high amplitude events (>2x median absolute deviation) and identifying the median of the filtered trace. This median was subsequently used to normalize the ΔF/F. Unless otherwise stated, the peri-event fluorescence traces were analyzed 2s prior to and 4s after the monitored event. Baseline activity was calculated from the time interval ranging from 2s to 1s before the event. This baseline activity was used to compare across animals and calculate the robust Z score. Generally, the area under the curve and peak amplitude parameters were used to evaluate changes in neuronal activity. The area under the curve was calculated using the trapezoidal method for integrals (*trapz*). Where applicable, peak, mean, and minimum fluorescence were calculated from the 2s prior to the event and from the event to 4s post the event. To calculate the effects of a drug, mean fluorescence values were taken from 10 min to 5 min prior to the drug injection and from 25 min to 30 min after the drug injection, unless otherwise stated. In some instances, the mean ΔF/F value and the frequency and amplitude of transients were calculated using the *findpeaks* command in MATLAB with a prominence value of 2.9 x standard deviation of the data. These results were compared to another method where we took the first-order time derivative of the ΔF/F signal and annotated transients above 5% ΔF/F per 0.01s. If significant differences were observed in the frequency of transients between these two measurement approaches, we manually verified the transients in signal or discarded data. Three conditions were used to identify GCaMP6/$\text{GRAB}_{\text{ACh 3.0}}$/iGABASnFR signals as true physiological signals: 1. The signal should show spontaneous activity under baseline conditions, which was generally reduced under isoflurane anesthesia. 2. The rise time should be much more rapid than the decay time for transients corresponding to behavioral responses or spontaneous transients. And the transient decay time should be representative of the time constant of the physiological response and the indicator used, and 3. The standard deviation of the signal should correspond to *at least* 5% ΔF/F consistently for the duration of the recording period. As additional verification of the signals for $\text{GRAB}_{\text{ACh 3.0}}$ experiments, we used M3 mAChR antagonist: scopolamine (3 mg/kg, Tocris) and acetylcholine esterase inhibitor: donepezil (6 mg/kg, Tocris) to confirm that the signal was representative of acetylcholine. The decrease in activity associated with nocifensive behaviors was observed in those experiments after trial averaging. In a single trial, the nocifensive behaviors were associated with a 'pause' in ACh release. We aligned the data when a drug was injected, or manipulation was conducted and not to the peak monitored effects. The code that supports the analysis will be made available from the corresponding author upon reasonable request.

In vivo calcium imaging

Mice first underwent surgery for viral injection, GRIN lens implant, and headplate attachment as described above. These mice were individually housed after the surgeries. Three weeks after the surgery, each mouse was habituated to the head fixing apparatus (custom-made) over one week. For the first day, mice were allowed to freely explore the apparatus for 15 mins. On days 2-5, mice were head-fixed in the apparatus multiple times a day for increasing time intervals ranging from 5 to 30 mins with sucrose rewards during head fixation. On days 6-7, mice were head fixed to the apparatus for 30 mins without sucrose rewards. On day 7, we selected a particular field of view (FOV) by adjusting the imaging plane (z-axis) through the GRIN lens using a two-photon microscope imaging system (Leica SP-5 equipped with Mai Tai (SpectraPhysics) 710-990 nm broadband laser). Multiple FOVs in different wavelength channels were collected using confocal and two-photon imaging capabilities along different z-positions.

This data was logged and 3D reconstructed to aid in capturing images from the same FOV during the course of the experiments. The z-position of the objective relative to the GRIN lens was controlled using LAS AF software. The FOV selected for imaging was where most cells showed pain-evoked responses. Throughout the imaging session, we just used one FOV to capture all neuronal data. Neurons above and below the FOV were excluded from the analysis.

To image calcium dynamics, an excitation wavelength of 910 nm was used. The microscope was equipped with resonant scanners allowing for 512 x 512 image acquisition at 32 Hz. For photon detection, nondescanned GaAsP photomultiplier tubes (PMT) were used. The PMT photodetectors with adjustable voltage, gain, and offset were kept consistent across animals and imaging sessions. The microscope was interfaced with the LAS AF software system on a computer (HP) to tune the 2p laser power, adjust the gain, and acquire data. The software also allowed control of the z-position of the objective, as mentioned earlier. These software settings corresponded to peak laser intensity: ~1.12W; PMT voltage gain: 1250V, offset: 0%, scan resolution: 512 x 512, zoom: 1.2x, aspect ratio, 1:1. An inverter (LSM technologies) was used to convert the inverted microscope to an upright microscope for *in vivo* imaging. A long working distance 20x air objective was used in these imaging experiments (Olympus, LCPLN20X, 0.45 NA, 8.3 mm WD). This microscope was also capable of confocal imaging with 488 nm Argon laser and GaAsP PMT detectors. These were used to identify the surface of the lens and the potential focal plane, which was subsequently fine-tuned using 2p excitation. When necessary, fields of view and the laser scanning direction were manually rotated to superimpose previous fields of view. To accomplish this, scratch marks on the head plate were used to orient the appropriate FOVs. Prior to each imaging session, FOVs were manually aligned with standard deviation projections from the previous imaging session to ensure the same cells were imaged on consecutive days. Images were collected as 12-bit tiff files at a resolution of 512 x 512 pixels (~455µm x ~455µm) at ~32 Hz.

The experimental procedure was as outlined in Figure 5. Mice were head-fixed during each test day, and cells were visualized first using confocal imaging and then 2p imaging. After 10 mins of head fixing, spontaneous activity was recorded for 10 mins. Subsequently, a noxious stimulus was administered to the tail, which consisted of mechanical and thermal stimuli. Thirty secs of data were captured, during which the noxious stimuli were administered. Data were truncated to 2s before and 4s after applying noxious stimuli to aid data storage and subsequent analysis. Behavioral data was logged by two independent cameras at 60fps to synchronize recordings of nocifensive responses and the neuronal activity with an error rate of ~1-2 frames (15-30 ms). For the mechanical stimuli, we applied a tail pinch using forceps calibrated using a force transducer for consistent application of mechanical force (Sparkfun SEN-09376). A high-intensity infrared heat source was used for the consistent application of radiant heat (BigLasers). Both mechanical and thermal stimuli were applied to the tail of the mice. During separate experiments not conducted during in vivo imaging, we also tested the latency to paw flick using a radiant heat source assay in the same mice. These responses were logged to compare the progression of the pain state. Drugs, including morphine (10mg/kg) and EVP 6124 (0.3mg/kg), were injected subcutaneously, and 15 mins following injection, spontaneous and noxious stimuli evoked activity were once again monitored using the 2-photon microscope. This method was repeated after induction of chronic neuropathic pain via paclitaxel injection, following the morphine tolerance paradigm, and finally after EVP-6124 administration. Successful development of chronic neuropathic pain and opioid tolerance were verified using the RHS assay.

Data were primarily analyzed using NoRMCorre, CNMF, and CellReg pipelines[93–98]. Non-rigid motion correction was conducted on non-spatially and temporally downsampled data. To rectify artifacts induced by motion correction, we determined the maximum translation in each session and cropped it out before cell registration. After non-rigid motion correction, 32 Hz images were temporally downsampled by bilinear averaging to 8 Hz to reduce the sampling frequency for data analysis. Data were not spatially or temporally downsampled after this point for the remainder of the analysis. We used a constrained non-negative matrix factorization pipeline for cell registration, allowing for automated registration of cells. Cells were identified based on their spatial morphology and temporal independence of dynamics. The registered cells were verified by an experimenter blinded to the pain condition or the drug administered. This verification was essential given the neuronal-like calcium activity traces shown by neuropil, including dendrites and local axons. When verifying neurons, experimenters evaluated the median and the standard deviations of the spatial profiles of the neurons and activity trace across all sessions. These metrics allowed for the efficient isolation of active neurons from neuropils, background, and quiescent neurons.

Post-registration, neurons were first selected based on their responses to noxious stimuli. To identify these pain-responsive cells, we pooled evoked responses across all conditions and calculated a p-value for each neuron using a single-tailed Wilcoxon rank-sum. Neurons with $p<0.01$ were designated as responsive to noxious stimuli. Neurons that were responsive in at least one session of the study were considered pain-responsive. While many neurons were pain-responsive in baseline testing, even more neurons were recruited after the chronic pain state was induced. Subsequently, they were tested for their sensitivity to morphine, development of opioid tolerance, and sensitivity to EVP-6124. In raster plot figures, cells are ordered by identity on the magnitude of baseline pain responses. Transients were identified based on the fast rise time and slow decay. These transients were also identified based on first-time-derivative, similar to fiber photometry analysis. These transients were >2.9 median absolute deviation for at least 0.5s. The mean baseline transient rate was calculated independently for each neuron across all sessions. The same identification parameters were used for individual neurons across all sessions. To align cells across multiple sessions, we used CellReg. After assigning all neurons across all imaging sessions to a 'global' neuron, we manually inspected each mouse's cross-day neuronal registration. Given that the activity of multiple neurons was significantly correlated, substantial care was taken to ensure that the spatial footprints were appropriately segregated. ΔF/F values were generated using median fluorescence values after excluding values outside 2x median absolute deviation, similar to fiber photometry analysis. Robust-z-score was generated using similar methods as fiber photometry.

Behavior

Opioid tolerance paradigm

To induce tolerance to the antinociceptive effects of morphine, mice were exposed to twice-daily subcutaneous injections of morphine at escalating doses over seven days. On days 1-2, mice received 2x 10mg/kg injections; on days 3-4, mice received 2x 20mg/kg; and on days 5-7, they received 2x 30mg/kg. Morphine or control saline injections were separated by at least 6 hours.

Tonic inflammatory pain/formalin assay

One week prior to experimentation, mice were habituated to experimenter handling, drug injection, behavioral chamber, and optical fibers. The behavioral chamber was 30cm x 30cm x 100cm (LxWxH) with transparent walls and a 45° angled mirror fixed beneath a transparent floor. On the day of testing, mice were injected intraplantar with saline or 10µL of 1.5% formalin into the plantar surface of one hind paw. The formalin solution was made by diluting 37% formaldehyde (Fisher Scientific Company, F79500) in sterile saline. Following intraplantar injection, animals were placed within the behavior chamber and monitored for 1 hour post-injection by researchers blinded to drug/optogenetic treatment conditions. All sessions were video-recorded using a Logitech camera and Dell laptop to cross-verify behavior scoring with other experimenters and reanalyze data as necessary. JWatcher (UCLA) software was used to track the amount of time the injected paw was flat, lifted, or licked. When fiber photometry was combined with the formalin assay, Synapse software was used to monitor the time spent engaging in nocifensive behaviors. The percentage time spent licking or lifting the paw during this 5-min time bin was calculated to quantify the duration of nocifensive behaviors. The first 10 mins after formalin injection were classified as the acute inflammatory pain phase, and 20-40 mins after formalin infection were classified as the tonic inflammatory pain phase.

To test the analgesic effects of drugs, we injected the test drug 10 mins prior to formalin injection. To test the efficacy of α7 nAChR agonists EVP-6124 (0.3mg/kg s.c., ChemBlock) and PHA-543613 (10mg/kg s.c., Sigma). To test the necessity of PPARα signaling, GW6471 (3mg/kg, Tocris) was injected intraperitoneally 15 min prior to EVP-6124 administration. To test the efficacy of α7 nAChR PAM, PNU-120596 (10mg/kg, Tocris) was injected subcutaneously.

To test the involvement of endogenous opioid circuits, naloxone hydrochloride was administered subcutaneously (6mg/kg, Sigma-Aldrich, BP548). Morphine (10mg/kg s.c., Sigma) was used as a μ-opioid receptor agonist.

Sterile saline or vehicle control was used in all assays. Drugs were dissolved in sterile saline, and Kolliphor or DMSO was used to dissolve drugs when they were not water-soluble according to published protocols.

Thermal radiant heat source (RHS) assay

Mice were habituated to experimenter handling and behavioral arena for three consecutive days prior to experiments. On the day of testing, the radiant heat source was placed at a distance of ~3cm from the foot paw with a power output of ~300mW/cm^2 in the IR wavelength range. The latency to paw withdrawal was measured when additional nocifensive signs accompanied the responses, including vocalization, repeated flicking or licking of the paw, orofacial changes, etc., to prevent the incorrect classification of general locomotion-related paw movement. If no response was observed at a latency of 20s, the test was stopped to avoid tissue damage. Three measurements were taken from each hind paw. Generally, in optogenetic RHS assays, we measured three paw withdrawal latencies corresponding to baseline, manipulation, and recovery.

In opioid tolerance and associated optogenetic testing, morphine was injected 1hr after optogenetic stimulation. In experiments that tested naloxone, it was injected 10 mins before the first RHS assay. Morphine was administered immediately after the first RHS assay, and the second RHS assay was conducted 10 mins later. 10 mins following the second RHS assay, optogenetic stimulation testing was carried out.

During optogenetic activation of PPTg^{ChAT+}→vlPAG terminals, an RHS assay was conducted 15 mins after 20hz pulsed stimulation. In a subset of experiments, varying frequencies of optogenetic stimulation were tested. Multiple frequencies and pulse duration paradigms resulted in analgesic effects >8mins after optogenetic activation of PPTg^{ChAT+}→vlPAG terminals, but 10ms pulses at 20hz were chosen as they closely mimic optogenetic strategies used in various publications. Optogenetic activation was conducted 3 hours after baseline testing, and the recovery assays were conducted on the subsequent day. To test for the reproducibility of analgesic effects, we conducted baseline and optogenetic assays on 10 consecutive days.

vlPAG$^{Chrna7+/Oprm1+/Gad+}$ optogenetic manipulation assay was preceded by baseline testing 3 hours before the manipulation and followed by recovery testing on the subsequent day. Optogenetic activation was conducted using 20hz pulsed stimulation, and inhibition was achieved using continuous light delivery at the respective opsin-activating wavelengths. During certain assays, where we were testing for pronociceptive effects, e.g., activating vlPAG$^{Chrna7+}$ neurons, we decreased the light intensity of the radiant heat source to ~200mW/cm^2 at a distance of ~3cm. The intensity was decreased to prevent ‘floor’ effects which could impede measurements of the pronociceptive effects of optogenetic manipulation.

To test for thermal hyperalgesia, first baseline paw withdrawal latencies were measured, and then complete Freund’s adjuvant (CFA, volume, company) was injected into the intraplantar surface of the hind paw. Mice were tested daily for six days, 3 hours before and during optogenetic activation of PPTg^{ChAT+}→vlPAG terminals or optogenetic inhibition of vlPAG$^{Chrna7+}$ neurons.

To test the involvement of various AChRs in the antinociceptive effects of activating PPTg^{ChAT+}→vlPAG terminals, we administered antagonists systemically after baseline testing. Optogenetic stimulation was conducted 20 mins after antagonist administration for 15 mins before the RHS assay. Antagonists included atropine (10mg/kg, Sigma Aldrich), mecamylamine hydrochloride (3mg/kg, Tocris), DhBE (3mg/kg, Tocris), MLA (10mg/kg, Tocris), or AFDX 116 (6mg/kg, Tocris). Antagonists in focal drug administration studies included MLA (0.5mM, 200nL) and atropine (1mM, 200nL).

To test if EVP-6124 decreases the activity of vlPAG$^{Chrna7+}$ neurons, we optogenetically activated these neurons 35 min after subcutaneous EVP-6124 administration (0.3mg/kg). The RHS assays were conducted at 30 mins and 40 mins after EVP-6124 administration. The test conducted 30 mins after EVP-6124 administration captured the analgesic effects of EVP-6124. The test conducted 40 mins after EVP-6124 administration tested the necessity for the decrease in vlPAG$^{Chrna7+}$ neuronal activity for the analgesic effects of EVP-6124.

Cold allodynia assay

Mice were habituated to experimenter handling and behavioral chamber for three consecutive days prior to experiments. Mice were placed in a test chamber of dimensions 20cm x 20cm x 20cm (LxWxH) with a 2mm thick glass floor. Crushed dry ice was applied to the glass floor below the plantar surface of the hind paws. The time taken by the mice to withdraw their paw from the noxious cold stimulus was quantified as the latency to paw flick. Experiments were conducted with an intertrial interval of 15 mins. These tests were conducted in naïve and CFA-injected paws. Latencies to paw withdrawal were repeated to obtain three values for each hind paw which were then averaged.

Mechanical von Frey assay

Mice were habituated to experimenter handling and behavioral chamber for three consecutive days prior to experiments. Mice were placed in a test chamber 20cm x 20cm x 20cm with a mesh floor. Von Frey Filaments (EB Instruments, Fisher Scientific Company, NM1208120) were pressed perpendicular to the plantar surface of one hind paw applying a constant force to the paw. Paw withdrawal response or lack of a response was recorded for each force of the von Frey filament ranging from 0.04g to 8g using the up-down method. These tests were conducted in naïve and CFA-injected paws. von Frey assays were conducted before (baseline), during, and after (recovery) optogenetic manipulation. Recovery tests were conducted on the day after optogenetic manipulation.

Chronic inflammatory assay

We used complete Freund's adjuvant (CFA) to induce a chronic inflammatory pain state. 20uL of CFA (Sigma-Aldrich, F5881) diluted 1:1 in sterile saline was injected into the hind paw using a 30G insulin syringe. The mice were picked from and returned to the home cage for the CFA injection. The mice were monitored daily for significant changes in health and behavior. Effects of chronic inflammatory pain on neuronal physiology using fiber photometry were tested within and between groups one day prior to CFA injection and three days after CFA injection unless otherwise stated.

Chronic neuropathic assay

To induce a chronic neuropathic pain state, mice were injected subcutaneously with paclitaxel (8mg/kg, Thermo Scientific, AAJ62734MC) on alternate days for eight days, resulting in a total of 4 injections. The mice were picked from and returned to the home cage for these injections. During and after this injection protocol, mice were monitored daily for changes in health and behavior. Effects of chronic neuropathic pain on neuronal physiology using fiber photometry were tested within and between groups one day prior to the first paclitaxel injection and ten days after the last paclitaxel injection unless otherwise stated.

Noxious mechanical or thermal assays

To explore the responses of vlPAG$^{Chrna7+}$ neurons, we administered multiple noxious stimuli. These included pinprick, applying acetone to the hind paw, and applying water at different temperatures to the hind paw. These assays were conducted in the same chamber as mechanical von Frey assays. The order was kept consistent across animals tested. In these assays, high frame rate video capture was used to time lock the nocifensive responses to the fiber photometry signal. For the pinprick, a 25G needle (BD, Fisher Scientific Company, 511098) was applied to the plantar surface of one hind paw. The pressure was applied to the point of tissue indentation without rupturing the paw surface.

To test for cooling-induced nocifensive responses associated with acetone, using a micropipette (Eppendorf, 20-200μL, 3123000055), 20μL of 100% Acetone (Fisher Scientific Company, A18P-4) was applied to the plantar surface of one hind paw. To test for nocifensive responses evoked by water at 55°C, distilled water was maintained at heated to 57°C using a dry bath incubator, and 20μL was applied to the hindpaw using a micropipette. To test for nocifensive responses evoked by water at 2°C, ice water was applied to the hindpaw using a micropipette. The time between pipetting the water in either condition and application was calibrated such that by the time water was applied, the temperature of the water was 55°C or 2°C, as necessary.

Salient stimuli assays

To explore the responses of vlPAG$^{Chrna7+}$ neurons, we administered multiple salient stimuli that were inherently non-noxious. These stimuli included the experimenter's approach to the plantar surface of the paw, white light, auditory tone, plantar brush, and water application, and oral sucrose and quinine administration. These experiments were conducted in the same chamber as von Frey assays. For 'experimenter approach', the experimenter approached the plantar surface of the paw with regular von Frey filaments, but the filament was not touched to the paw. For light application, white light was projected onto the eyes of the mouse at 2000 lux. For auditory tone, 18kHz at 50dB was played for 500ms at a 20cm distance from the mice. To test non-noxious somatosensory stimuli, a brush (Royal & Langnickel size 2) was lightly applied to the plantar surface of the hindpaw, and 20μL of water at 27°C was applied to the plantar surface of the hindpaw using a micropipette. For intraoral delivery of rewarding and aversive gustatory stimuli, 50μL 30% sucrose or 0.2 mg/ml quinine was delivered orally for the mice to spontaneously lick from the micropippeter. The quinine was presented after multiple bouts of sucrose licks.

Open field assay

Mice were placed in a custom-made white acrylic chamber (42cm x 42cm x 20cm) for 20 min. Locomotion was captured using Ethovision XT-16 software by a video camera mounted above the behavioral chamber. We used Ethovision to monitor the mouse's center point, which captured the distance moved, locomotion speed, and movement bouts in 30 sec time bins. These binned locomotor parameters were correlated with fiber photometry data to test for relationships between locomotion and ACh levels or activity of vlPAG$^{Chrna7+}$ neurons using temporal cross-correlation. The correlogram was compared with shuffled data to test for the significance of correlations. In addition to center point-based locomotion, we used head and tail point detection based on fine movements and pixel energy based on the total change in pixels in the video frame to evaluate if fine movements were correlated with physiological parameters using a similar analysis. Spontaneous activity was recorded in the open field chamber unless otherwise stated. To test for changes in anxiety phenotypes during stimulation, we quantified the time spent in the center of the open field and the number of entries into the center region using arenas defined in Ethovision. The center of the arena was 21cm x 21cm. These anxiety assays were conducted for 20 mins, and optogenetic activation or inhibition was conducted for either the first or last 10 mins counterbalanced within groups.

Rotarod assay

Mice were acclimatized to the experimental room for 30 mins before testing. The rotarod (Columbus Instruments, Rota Rod Rotamex 5) was started at four rotations per min (rpm). Then animals were placed in a way so that they walked forward in individual lanes. Four animals were tested simultaneously. The rotations were increased by 1 rpm every 10s. The latency to fall was measured. The assay was stopped after 200s. Five repeated trials were conducted with an intertrial interval of 5 mins, and the latency to fall (s) was averaged across trials. Drugs were injected 15 mins before the first trial. Optogenetic stimulation was conducted for 15min before the first trial and during the intertrial intervals.

Somatic withdrawal assays

Mice exposed to the opioid exposure paradigm were injected with naloxone (10mg/kg). They were placed in a cylindrical chamber with transparent walls with a diameter of 5 in and a height of 10 in. In a 10 min period, the number of times that mice stood on their hind legs was quantified as ‘rearing,’ and the number of times mice jumped (all four paws were off the ground) was quantified as ‘escape jumps’. These behaviors are well-characterized outcomes of naloxone-precipitated opioid withdrawal. Optogenetic inhibition of vlPAG$^{Chrna7+}$ neurons was conducted to test for relief of somatic withdrawal signs, including rearing and jumping.

Real-time place preference assay

Mice were placed into a custom-made black acrylic two-chambered box (52cm x 26cm x 26cm) and allowed to explore the chambers for 20 min. Optogenetic stimulation was triggered based on a pre-decided ‘stimulation-paired’ chamber when mice spontaneously moved to the stimulation-paired chamber. The physical side of the ‘stimulation-paired’ chamber was counterbalanced in these experiments. During these experiments, mice were tethered to an optogenetic patch cord with a rotary joint, and their position was tracked using a Basler camera and Noldus Ethovision XT 16 software. The amount of time spent in the ‘stimulation-paired’ chamber as a percent of total time (20 min) was quantified. The optogenetic stimulation strategy in the real-time place preference assay is defined in the optogenetics section.

Conditioned place preference assay

A custom-made three-chambered behavioral apparatus was used (58cm x 28cm x 28cm). The walls had either vertical or horizontal black stripes with different textured floors in the two main chambers (26cm x 28cm x 28cm). These main chambers were connected by a small central connecting chamber (6cm x 6xm x 28cm). A camera was positioned above the behavioral apparatus to track mice using Noldus Ethovision XT 16 software. On the preconditioning day (day 1), mice were allowed to freely roam the three chambers for 20 mins. This preconditioning data was used to counterbalance the initial chamber preference. We used an unbiased design, wherein groups contained an equal number of mice that showed a preference for the chamber that they would receive or would not receive drug or optogenetic manipulation. On the next three consecutive days (days 2-4), mice underwent a morning and afternoon conditioning session separated by at least 6 hours. In the morning session, mice were secluded in one chamber for 20 mins, and in the afternoon session, mice were secluded in the other chamber for 20 mins. On the post-conditioning day (day 5), mice were allowed to freely roam all chambers. The amount of time spent in either chamber was captured using a video camera interfaced with Ethovision XT 16.

For drug or pain conditioning-based CPP experiments, WT mice were used. When testing for affective pain relief by EVP-6124 - after the pre-conditioning day, mice were split into two groups. Group 1 received a subcutaneous saline injection and intraplantar saline injection (10µL) in the morning and a subcutaneous saline injection and intraplantar 2% formalin injection (10µL) in the afternoon. Group 2 received a subcutaneous saline injection and intraplantar 2% formalin injection in the morning and a subcutaneous EVP 6124 injection and intraplantar 2% formalin injection in the afternoon.

When testing for withdrawal effects associated with EVP-6124 and morphine use, mice were injected with EVP-6124 or morphine for five days. On Day 6, preconditioning baseline preference was monitored. For conditioning, Group 1 received EVP-6124 and saline in the morning and EVP-6124 and MLA in the afternoon. Group 2 received morphine and saline in the morning and morphine and naloxone in the afternoon. Antagonist or saline was injected 10 mins prior to EVP-6124/morphine injection.

For reward profile testing of the conditioned drugs, animals were injected with saline in the morning and EVP-6124, morphine, or saline in the afternoon. The post-conditioning preference for all groups was monitored on the subsequent day. Drug concentrations used in these assays: EVP-6124 (0.3mg/kg), morphine (10mg/kg), naloxone (6mg/kg), and MLA (10mg/kg).

Histological assays

Viral and cannula placement

Mice were deeply anesthetized with isoflurane and perfused with cold phosphate-buffered saline, followed by perfusion with 4% paraformaldehyde in PBS. Brains were then placed in PFA for 24 hours and then immersed in hypertonic sucrose solution, first 15% and then 30% until they sank. They were subsequently embedded in optimal cutting temperature (OCT) compound (Tissue-Plus, FisherBrand) until slicing. 40 µm coronal slices (Leica CS3050 S) were cut and mounted onto Superfrost-Plus Microscope Slides (FisherBrand) with DAPI Fluoromount-G (Southern Biotech) and covered by a coverslip (Fisherbrand). Slides were stored at 4°C until imaging. The slices were imaged on a confocal microscope (Marianas 3i spinning disk confocal) for viral and cannula placement at 20x magnification (Zeiss). These images were masked, and if the majority of viral spread or cannula tip was outside the intended region, the animals and the associated data were discarded.

Immunohistochemistry

Slicing procedures were the same as above. But for immunohistochemistry staining, slices were transferred to a 24 well-plate and immersed in PBS (1X, pH 7.4). Slices were treated for 1 hour with a blocking solution based in PBS (1X, pH 7.4) with 0.01% Triton X-100 (Electron Microscopy Sciences, 22145) and 10% Normal Goat or Donkey Serum (Abcam, AB 7481, AB 7475). For the described experiments, one or multiple of the following primary antibodies were mixed in blocking solution: solution: anti-c-fos (Cell Signaling 2250, 1:2000), anti-ChAT (Millipore Sigma AB144P), anti-μ-OR (Abcam 134054), anti-Gad65 and Gad67 (Millipore Sigma AB1511), anti-Gad67 (Millipore Sigma MAB5406), Anti-m2 mAChR (Millipore Sigma MAB367), Anti-PPARα (Santa Cruz 398394), Anti-NAPE-PLD (Abcam 246951), Anti-FAAH (Abcam 128917), Anti-pAMPK (Cell Signaling 2535), Anti K_v2.1 (Addgene 180083) Anti pK_v2.1 (gift from James Trimmer). In experiments exploring protein expression of α7 nAChRs, we used fluorescently conjugated α-Bungarotoxin (Invitrogen B13422 or B35450). Slices were incubated in the primary antibody overnight and triple-washed with PBS (1X, pH 7.4) the following morning. When using antibodies raised in mice, Anti-Mouse F(ab) IgG H&L fragments were used (Abcam 6668). Secondary antibodies were chosen according to the blocking serum, the primary antibody's host, and multiplexing with other antibodies. For example, if we used normal goat serum and primary raised in rabbit and needed staining in 488/green channel, we used 1:400 dilution of Goat Anti-Rabbit IgG H&L (Alexa Fluor 488, Abcam 150077). Secondaries antibodies were allowed to incubate for 2 hours. Slices were then triple-washed and mounted on Superfrost-Plus Microscope Slides (FisherBrand) with DAPI Fluoromount-G (Southern Biotech) and covered by a coverslip (Fisherbrand). Slides were covered and stored at 4°C until imaging. For visualization, the slices were imaged on a confocal microscope (Marianas 3i spinning disk confocal) at 20x (Zeiss Plan-Neofluar NA 0.5 air) or 40x (Zeiss Plan-Apochromat NA 1.3 oil). In certain experiments, mice were either pretreated *in vivo* with α7 nAChR agonist or saline and then exposed to a pain state using formalin or saline injection in the hindpaw. Care was taken to acclimatize the animals to handling, transport, and anesthesia-related stress for 3-days prior to the perfusion. Animals were sacrificed 30 mins after drug or formalin injection. For vlPAG slices, 1 in 4 sampling was used, i.e., every 4th brain slice was used to cover the extent of the vlPAG. For whole-brain slicing exploring cholinergic inputs, 1 in 6 sampling was used. Known cholinergic nuclei with long-range projections were selectively explored for labeling. After image acquisition, slices were analyzed for overlap using a custom-written script in Cell Profiler in a manner similar to the analysis profile used for FISH. To evaluate changes in expression or phosphorylation levels of proteins of interest, data from both experimental groups were acquired, processed, and analyzed with exactly the same parameters by experimenters blinded to the treatment. At least one slice per animal was included where no primary antibody was added and another slice where no secondary antibody was added to test for nonspecific labeling or background fluorescence, respectively.

Fluorescent in situ hybridization/RNAScope

Adult (~P60) wild-type male and female (n = 4 total) were used for these experiments. Mice were deeply anesthetized with isoflurane, and brains were extracted and immediately flash-frozen over dry ice and at -80°C under RNase-free conditions. Care was taken to ensure that decapitation to permanent freezing happened within ~45s-1 min. After the brains were completely frozen, they were embedded in an OCT compound (Tissue-plus, Fisherbrand) and frozen once again. Brains were sliced along the coronal plane at a thickness of 20µm (Leica CS3050 S). These slices were immediately transferred to Superfrost Plus Microscope Slides (Fisherbrand) and were stored at -80°C until the next day when the hybridization protocol was conducted.

The hybridization assay was conducted as per Advanced Cell Diagnostics (ACD) instructions for Manual RNAscope Fluorescent Multiplex Assay. Materials for this experiment were purchased as a complete kit from ACD (ACD, 321720). Slides were removed from the -80°C freezer and fixed in chilled 4% PFA using Tissue-Tek containers for 10 mins. The tissue was then dehydrated in 50% EtOH, 70% EtOH, and 2x in 100% for 5 min immersions. Slides were air-dried, and a hydrophobic barrier was drawn by a hydrophobic pen (Immedge Pen). After the barrier was dried, the slices were treated with a protease (Protease 4) that completely covered the slice for 30 min at room temperature. The protease was removed from the slides. The slides were placed in the Tissue-Tek hybEZ slide rack and staining dish and washed with PBS (1X, pH 7.4). Probes were mixed so that Channel 1, Channel 2, and Channel 3 had a 50:1:1 dilution, per ACD instructions, and were warmed to 40°C. The probe mix was pipetted onto the tissue to fully immersed the tissue. The slides were then placed in a sealed 40°C oven for 2 hours

(HybEZ oven). The slides were then washed in 1X RNAscope wash buffer (ACD) three times for 2 mins each. AMP-1 was then applied to the slides and incubated in the oven for 30 mins. After incubation, slices were washed three times in the RNAScope wash buffer. The process of incubation and triple washing was repeated for AMP-2 (15 min incubation), AMP-3 (30 mins), and AMP 4-FL (15 mins). After the final wash, nuclei were counterstained using DAPI Fluoromount-G (Southern Biotech), and slides were coverslipped (Fisherbrand). Slides were stored at 4°C in a dark environment until imaging on the subsequent day.

Images were acquired with a Marianas confocal microscope and 3i software using a 20x (Zeiss Plan-Neofluar NA 0.5 air) or 40x (Zeiss Plan-Apochromat NA 1.3 oil) objective. 16-bit images were acquired using the same microscope settings for each quantified image, i.e., similar intensity, threshold, and exposure times. The images were analyzed using a custom script written in CellProfiler. To analyze the images, individual channels corresponding to 405 nm, 488 nm, 561 nm, and 647 nm excitation were extracted. No deconvolution was performed. The DAPI/405 nm images were used to draw nuclei outlines using size, roundness, intensity, and contrast parameters. After identifying the nuclei, the number of green, orange, and red puncta were quantified using intensity, roundness, and size thresholds. Given that few mRNAs, including those of vGat and vGlut, were extremely highly expressed, we used % area coverage as our measure instead of counting puncta. This parameter captured the amount of extended nucleus area covered by probes in green, orange, or red channels. The extended nucleus area was characterized by increasing the diameter of the DAPI-stained nucleus to 20 μm. Generally, the % area coverage correlated strongly with the number of puncta in separately analyzed data. Background intensity values were obtained from ROIs that lacked cell bodies and subtracted independently in each channel, if necessary. Parameters to identify mRNA puncta, including area and nucleus boundaries, were kept consistent across slices. Positive and negative cells were categorized based on an adapted Otsu thresholding method. Generally, these required % area coverage to be >~3% of the extended nucleus area. Three slices spanning the anterior-posterior axis of vlPAG were used for the analysis. From each slice, six fields of view were captured for the analysis. Images were taken with six z-plane steps with 3µm step sizes. All assays included three positive (*Polr2a, Ppib, Ubc*) and one negative control probe (*Dapb*), which were used to verify the signal in the slides with test probes. Where possible, positive and negative tests were conducted using brain regions known to contain mRNA of the concerned test probe, e.g., VTA, hippocampus, mHb, etc. The RNAScope probes reference numbers that were used are listed: Neurotransmitters: 317621 – *Th*; 319191 – *Slc32a1*; 319171 – *Slc17a6*; 410351 – *Tac1*; 318761 – *Penk*; 318771 – *Pdyn*; 408731 – *Chat*; 404631 – *Sst*; and 313321 – *Npy*. Cholinergic receptors: 495291 – *Chrm1*; 495311 – *Chrm2*; 437701 – *Chrm3*; 410581 – *Chrm4*; 495301 – *Chrm5*; 312571 – *Chrna5*; 465161 – *Chrna7*; 449231 – *Chrnb2*; 449201 – *Chrnb3*; and 452971 – *Chrnb4*. Other targets: 315841 – *Oprm1*; 420721 – *Cnr1*; 466631 – *Hcrtr1*; 418851 – *Glp1r*; 411141 – *Htr3a*; 406501 – *Drd2*; and 474001 – *Cre-O1*.

Analysis

Data are expressed as means ± standard error of the mean in figures and text. Paired or unpaired two-tailed t-tests with or without Bonferroni corrections, Benjamini-Hochberg (B-H) procedure, and Pearson regressions were performed as appropriate. One-way, two-way, and repeated-measures ANOVA were used to compare more than two groups using GraphPad or MATLAB. Signed-rank and rank-sum tests refer to Wilcoxon signed-rank and rank-sum tests, respectively. For spontaneous post-synaptic currents, unpaired t-test was used to test for changes in frequency, and Kolmogorov–Smirnov test was used to test for differences in amplitude distributions. Spontaneous synaptic or calcium events were visually verified by the experimenter blinded to the treatment group to ensure the software correctly determined the events. For behavioral assays, either unpaired t-test, paired t-test, 1-way ANOVA, or 2-way repeated-measures ANOVA was used to analyze data, and Sidak post hoc test was used as appropriate. We used identical code and analysis methods for all cohorts throughout the study. All experiments were randomized and performed by a researcher blind to the viral injection or the pain state. Mice were not selected for any experimental condition based on previous observations or tests. Individual mice within cages were chosen arbitrarily to receive control or experimental viral injections, opioid tolerance treatment, or chronic pain manipulation. Individual mice were ear-tagged to assist in post-hoc verification of the animal’s identity. At least one animal from each group was tested within an experimental session. Generally, no cage was assigned for just one manipulation. Optogenetic stimulation frequencies, drug concentrations, and tolerance exposure paradigms were selected based on preliminary experiments. All behavioral experiments were recorded by computer videography and analyzed in a blinded manner. Histological verifications were conducted prior to the final analysis of behavioral data. Experimenters were blinded to the groups during histological verification to the group allocation. Sample sizes were predetermined for optogenetic and electrophysiological studies using power analysis but were not predetermined for fiber photometry and imaging studies. However, our sample sizes are similar to those reported in the literature. All relevant data and code are available from the authors upon reasonable request.

Test, statistics, significance levels, and sample sizes for each experiment are listed in Tables S1. ns $p > 0.05$, t tests and post hoc comparisons: $p < 0.05$, $p < 0.01$, $p < 0.001$; interaction: # < 0.05, ## $p < 0.01$, ### $p < 0.001$.

Results

Activation of cholinergic PPTg terminals in vlPAG drives analgesia

ACh release in the vlPAG is inhibited during nocifensive behaviors.

We investigated the relationship between pain states and the physiology of the endogenous neuromodulator acetylcholine (ACh) in the vlPAG. ACh regulates multiple behaviors critical for survival, and endogenous ACh release is relatively underexplored in the context of pain modulation. Using a novel ACh sensor – GRABACh 3.0 – we explored the dynamics of ACh release (Fig 6a). We observed that under no-pain baseline conditions, ACh is spontaneously released in the vlPAG (Fig 6b, Supp Fig 1a). While in multiple brain regions, behaviorally salient stimuli generally increase ACh release, nocifensive responses to acute painful stimuli decreased extracellular ACh levels in the vlPAG, as observed by the transient reduction in GRABACh 3.0 fluorescence (Fig 6c). In addition, inducing chronic pain using Complete Freund's Adjuvant (CFA) injection into the hind paw also decreased baseline ACh levels, as indicated by the decrease in mean fluorescence during open field behavior (Fig 6d,e). Note that ACh levels in the vlPAG were not correlated with movement (Supp Fig 1a,b).

Chronic pain assessment requires multiple behavioral sessions, which might alter endogenous neuromodulatory systems. Hence, we verified the negative correlation between ACh and pain state using a single-session formalin assay[99]. Within a formalin assay, different temporal phases are associated with varying levels of nocifensive behaviors, with Phase 1 associated with acute pain, followed by an Interphase with lower levels of nocifensive behaviors, and then Phase 2, which is associated with tonic or persistent inflammatory pain. Thus, a formalin assay provides an opportunity to correlate the animal’s pain state with ACh levels in the vlPAG. We observed that time periods of the formalin assay where mice demonstrated stronger nocifensive behaviors were associated with lower GRABACh 3.0 fluorescence, indicating lower levels of ACh in the vlPAG and vice-versa (Fig 6f, g). These observations suggest an interdependency between the pain state of an organism and the cholinergic tone in the descending pain pathways.

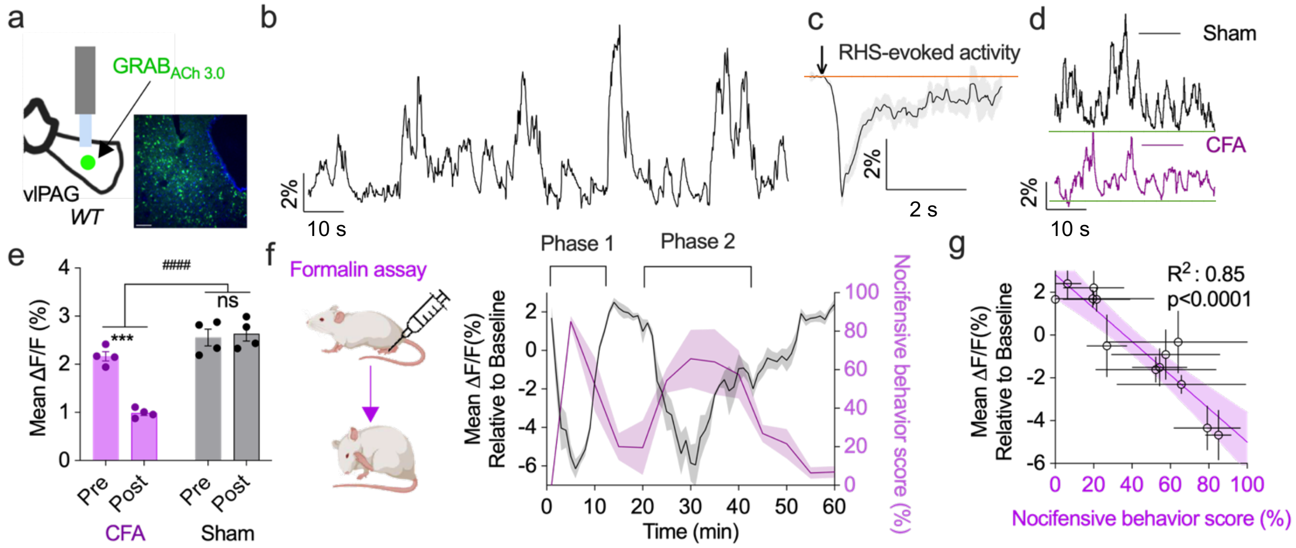

Figure 6: Nocifensive behaviors correlate with decreased ACh levels in the vlPAG.

a) Left: Schematic of viral GRAB$_{\text{ACh 3.0}}$ injection and cannula placement in the vlPAG. Right: Fluorescence image showing GRAB$_{\text{ACh 3.0}}$ expression on vlPAG neurons (green) with nuclear DAPI stain (blue, scale bar 50µm).
b) Representative recording of vlPAG GRAB$_{\text{ACh 3.0}}$ fluorescence dynamics recorded using fiber photometry during open field behavior.
c) Mean GRAB$_{\text{ACh 3.0}}$ fluorescence traces time locked to paw withdrawal in response to Radiant Heat Source (RHS) assay (downward arrow represents paw withdrawal, 6 traces per animal, n=4). Orange line indicates baseline fluorescence.
d) Representative GRAB$_{\text{ACh 3.0}}$ fluorescence traces from Sham control (black) and CFA injected animal (purple) collected 3 days after CFA/Sham injection. Green line indicates the zero value for fluorescence.
e) Mean GRAB$_{\text{ACh 3.0}}$ fluorescence in mice Pre- and Post-CFA injection (purple) and in Sham controls (gray). Sham: Pre vs. Post paired t-test p=0.7443, t=0.3576. CFA: Pre vs. Post paired t-test p = 0.0002, t= 23.73. Interaction: RM 2-way ANOVA p<0.0001, F(1,6) = 309.82.
f) Left: Schematic showing formalin injection in the plantar surface of the hind paw and subsequent monitoring of nocifensive behaviors for 1hr post formalin injection. Right: Mean

Figure 6 (continued): GRAB$_{\text{ACh 3.0}}$ per minute is plotted on the left y-axis in black, and the nocifensive behaviors score (% duration of a 5min time bin that mice spend licking, lifting, or guarding their paw) is plotted on the right y-axis in purple. Phase 1 (0-15min) and Phase 2 (20-45min) of the formalin assay are indicated at the top.

g) Negative correlation between nocifensive behaviors score (%) and mean GRAB$_{\text{ACh 3.0}}$ fluorescence in 5 min time bins. Each data point represents a separate 5 min time bin. The error bars represent the s.e.m across animals in that time bin (n=4).

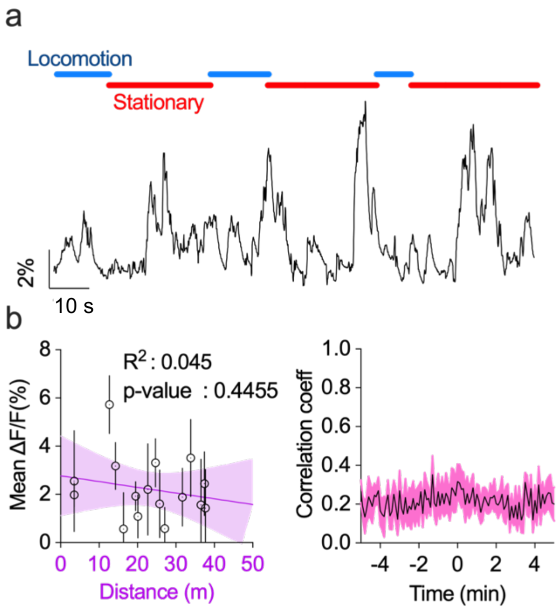

Supp Fig 1: ACh levels in vlPAG are not correlated with movement.

a) Representative recording of vlPAG GRAB$_{\text{ACh 3.0}}$ fluorescence recorded using fiber photometry during open field behavior. Behavior was captured using 2 orthogonally positioned cameras and analyzed manually and using Ethovision (see Methods). Locomotion and stationary phases are annotated in blue and red at the top, respectively.

b) Left: Mean vlPAG GRAB$_{\text{ACh 3.0}}$ fluorescence in 5 min time bins during open field behavior is plotted on the y-axis, and the corresponding distance traveled during the same 5 min time bin is plotted on the x-axis. Each point represents data from a single mouse. n=3 mice. Right: Correlogram between distance moved in the 10s-time bin and mean fluorescence during the same time bin. n=3 mice.

Cholinergic PPTg neurons project to the vlPAG.

Given the negative correlation between nocifensive behaviors and ACh release in the vlPAG, we explored potential cholinergic inputs to the vlPAG, with the goal of testing the analgesic effects of activating these inputs. We used a retrograde anatomical labeling approach, injecting a retrogradely transported virus (AAVrg)[100] into the vlPAG of *ChAT-Cre* mice to label presynaptic *Cre*-expressing neurons with tdTomato and non-*Cre*-expressing neurons with EYFP[101] (Fig 7a). After verifying the injection site location with EYFP fluorescence (Fig 7b), we conducted whole-brain confocal imaging (Fig 7c). We identified strong tdTomato backlabeling in Pedunculopontine Tegmental Nucleus (PPTg) and Laterodorsal Tegmental Nucleus (LDTg, Fig 7d). Sparse labeling was observed in cholinergic nuclei of the basal forebrain, including the Medial-Septum Diagonal Band of Broca (MS-DBB) (Fig 7c, d). Viral infection may differ between neuronal types. To rule out that potential confound, we cross-verified our AAVrg-based results using retrograde labeling with fluorescent microspheres and ChAT immunohistochemistry (IHC) and found backlabeling in cholinergic nuclei similar to that seen with viral infection (Supp Fig 2a). We also performed axonal tracing experiments by injecting a virus in PPTg that, in a *Cre*-dependent manner, expresses tdTomato in the cell nucleus and Synaptophysin-tagged EYFP in axon terminals (Supp Fig 2b). In the vlPAG, we observed robust EYFP labeling of axonal terminals, further verifying presynaptic cholinergic terminals originating from the PPTg (Supp Fig 2c). These results agree with previous publications[102,103] and publicly available data from Allen Brain Institute and demonstrate strong neuromodulatory input to the descending pain pathways originating from PPTg.

We extended these anatomical results by evaluating physiological ACh release in the vlPAG during selective activation of these cholinergic inputs. Here, we expressed red-shifted opsin ChrimsonR on PPTg^{ChAT+} terminals and GRAB$_{\mathrm{ACh\ 3.0}}$ in the vlPAG to simultaneously activate cholinergic terminals while monitoring ACh levels (Supp Fig 2d). We observed that activating PPTg^{ChAT+} terminals in the vlPAG increases GRAB$_{\mathrm{ACh\ 3.0}}$ fluorescence, indicating ACh release (Supp Fig 2e). These functional tests demonstrate that brainstem cholinergic nuclei provide strong endogenous ACh input to the vlPAG and open the door to optogenetic testing of pain modulation via these inputs.

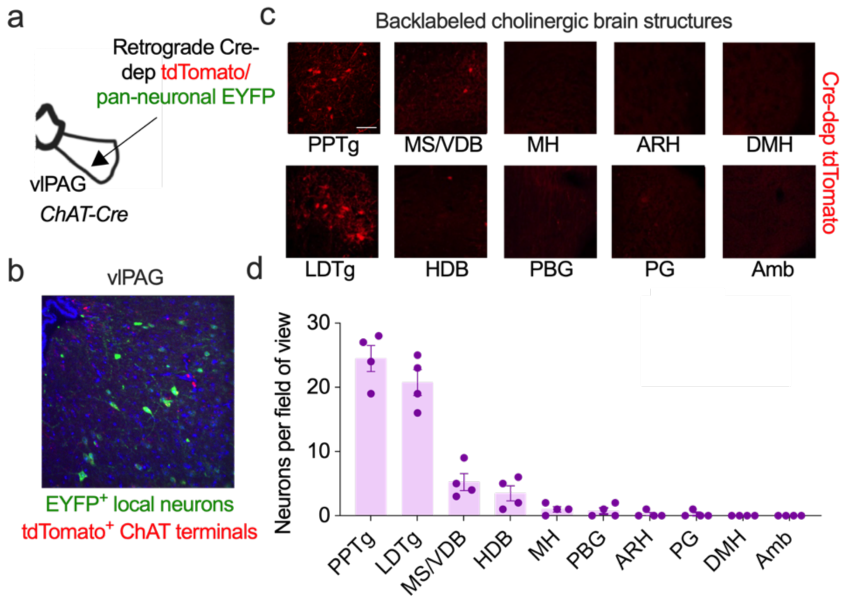

Figure 7: Identifying cholinergic inputs to the vlPAG.

a) Schematic showing injection of retrogradely transported virus that expresses tdTomato in *Cre*-expressing neurons and EYFP in all neurons in the vlPAG of *ChAT-Cre* mice.
b) Viral injection site in the vlPAG with local interneurons (green), cholinergic terminals (red), and DAPI stained nuclei (blue, scale bar 50µm).
c) Representative images of cholinergic brain structures.
d) Quantification of backlabeled cholinergic neurons per field of view (FOV). Each data point represents an animal. From each animal, at least 6 FOVs were collected per brain region, and the number of neurons were averaged per animal. n=4.

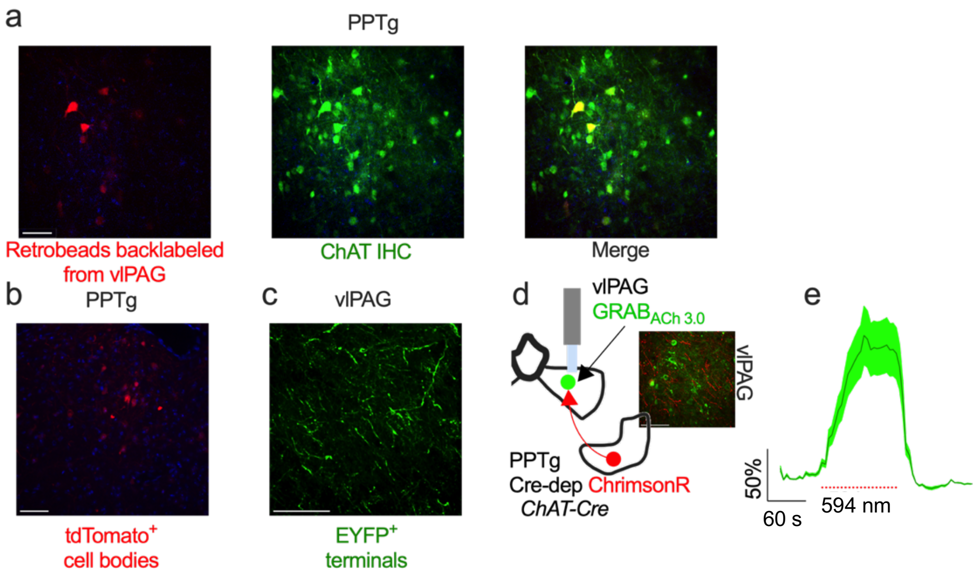

Supp Fig 2: PPTg^{ChAT+} neurons send functional cholinergic projections to the vlPAG.

a) Left: PPTg fluorescence image depicting neurons backlabeled from the vlPAG by red fluorescent microspheres (retrobeads). Middle: Immunolabeling of cholinergic neurons in the PPTg (green). Right: Merged image showing cholinergic PPTg neurons backlabeled from the vlPAG in yellow (scale bar 50µm).
b) PPTg fluorescence image showing the injection site of a *Cre*-dependent virus expressing nuclear-localized tdTomato in *ChAT-Cre* mice. Nuclei of PPTg^{ChAT+} neurons are labeled red, and the nuclear DAPI stain is in blue (scale bar 50µm).
c) vlPAG fluorescence image of PPTg^{ChAT+} terminal expression of synaptophysin-tagged EYFP (green, scale bar 50µm).
d) Left: Schematic of viral ChrimsonR-tdTomato expression in PPTg^{ChAT+} neurons and pan-neuronal viral GRAB$_{ACh\ 3.0}$ expression in the vlPAG. Right: Fluorescence image of the vlPAG showing expression of ChrimsonR-tdTomato in PPTg^{ChAT+} terminals (red) and GRAB$_{ACh\ 3.0}$ (green, scale bar 50µm).
e) Mean vlPAG GRAB$_{ACh\ 3.0}$ fluorescence (green) time-locked to optogenetic activation of PPTg^{ChAT+} terminals (red dotted line) collected using simultaneous optogenetics and fiber photometry (2 traces per animal, n=2).

Activating PPTg^{ChAT+}→vlPAG projections is antinociceptive.

Given the dense PPTg^{ChAT+}→vlPAG anatomical connectivity (Fig 7) and the strong negative correlation between nocifensive behaviors and ACh release in the vlPAG (Fig 6), we explored the pain-relieving effects of activating this cholinergic circuit. In *ChAT-Cre* animals, we expressed ChR2[104] in PPTg^{ChAT+} neurons and placed an optical cannula in the vlPAG to activate cholinergic terminals (Fig 8a). Control animals expressed EYFP in these projections. Activating these cholinergic terminals increased latency to paw flick in a radiant heat source assay (RHS; Fig 8b) and increased the paw withdrawal threshold in a von Frey assay (Fig 8c). Given that LDTg was backlabeled in our anatomical tracing experiments (Fig 7c), we tested for antinociceptive effects of LDTg^{ChAT+} projections to the vlPAG. However, activating these LDTg projections showed little to no modulation of nocifensive responses (Supp Fig 3a), suggesting other roles of these projections.

We verified the antinociceptive effects of activating PPTg^{ChAT+}→vlPAG terminals using an alternate optogenetic approach (Supp Fig 3b). In *ChAT-Cre* animals, we injected retrogradely-transported virus in the vlPAG that expressed ChR2 in a *Cre*-dependent manner and placed an optical cannula in PPTg to selectively activate PPTg^{ChAT+}→vlPAG projection neurons (Supp Fig 3b). Somatic activation increased the latency to paw flick in the RHS assay, suggesting similar antinociceptive effects to that seen with axon terminal stimulation (Fig 8b). The analgesic effects of activating these projections were stable and repeatable over multiple days of testing. Furthermore, repeated stimulation of these projections over multiple days did not show evidence of tolerance at time scales that induce tolerance to repeated morphine injections (Supp Fig 3c).

Next, we explored the analgesic effects of activating this circuit in chronic inflammatory pain conditions induced by intraplantar CFA injection. We observed that activating PPTg^{ChAT+}→vlPAG projections consistently increased latency to paw flick (Fig 8d, Supp Fig 3d) and paw withdrawal threshold (Supp Fig 3e), indicating decreased mechanical allodynia and thermal hyperalgesia. In this chronic pain state, we also tested for cold allodynia using crushed dry ice, where we saw similar increases in latency to paw withdrawal, indicating anti-allodynic effects (Supp Fig 3f).

Given these robust somatic effects, we employed a real-time place preference assay to test if activating PPTg^{ChAT+}→vlPAG projections relieved the affective component of chronic pain (Fig 8e). We observed that mice in chronic inflammatory pain preferred to spend more time in the chamber paired with activation of PPTg^{ChAT+}→vlPAG projections, compared to EYFP controls or mice not in chronic pain (Fig 8e). These observations suggest that activating this circuit relieves the affective component of pain but does not induce preference in the absence of chronic pain.

Like many brain regions, neuronal activity in the brainstem cholinergic centers can be associated with locomotion. While a recent study demonstrated that inhibiting or activating PPTg^{ChAT+} neurons does not alter motor function[105], we assessed the potential confounding effects of our optogenetic activation of PPTg^{ChAT+}→vlPAG projections on locomotion, general motor control, and anxiety. To that end, we used an open field assay[106], rotarod assay[107], and a high-power output radiant heat source. In the open field assay, we observed that stimulating PPTg^{ChAT+}→vlPAG projections did not alter the distance traveled (Supp Fig 3g), the number of movement bouts (Supp Fig 3h), or time spent in the center zone (Supp Fig 3i). In the rotarod assay, we saw that activating these projections did not alter the latency to fall (Supp Fig 3j). Using a high-powered radiant heat source, we demonstrated that higher intensity RHS assay has lower latency to paw flick than the regular intensity RHS assay, even during optogenetic activation (Supp Fig 3k). These observations indicate that optogenetic activation of PPTg^{ChAT+}→vlPAG projections modulates pain sensitivity without altering the motor function or anxiety levels.

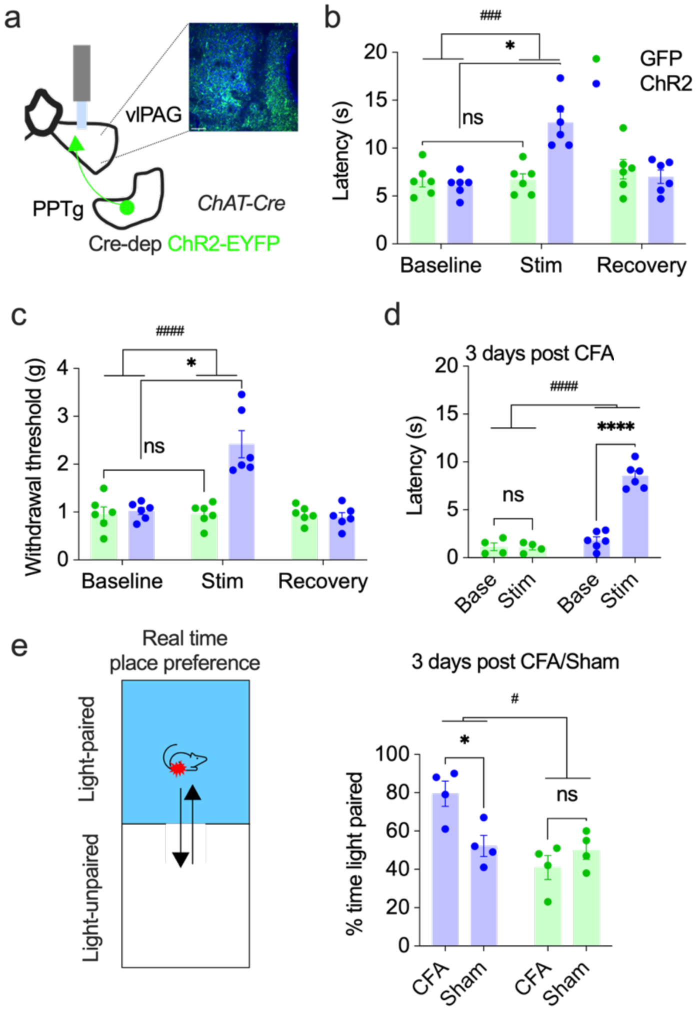

Figure 8: Activating PPTg^{ChAT+}→vlPAG projections is antinociceptive in acute and chronic pain conditions.

Figure 8 (continued): a) Left: Schematic showing *Cre*-dependent ChR2 expression in PPTg of *ChAT-Cre* animals and cannula placement in the vlPAG. Right: Fluorescence image showing ChR2-EYFP expression in the cholinergic terminals from the PPTg (green) with nuclear DAPI stain (blue, scale bar 50µm).
b) Latency to paw withdrawal in a RHS assay during no stimulation (Baseline), optogenetic stimulation (Stim), and post-stimulation (Recovery) in ChR2 expressing (blue) and GFP control animals (green). GFP: Baseline vs. Stim paired t-test p= 0.996, t= 0.08377. ChR2: Baseline vs. Stim paired t-test p=0.0123, t=4.54. Interaction: RM 2-way ANOVA p=0.007, F(2,20)=10.68. n=6 per group.
c) Paw withdrawal threshold in a von Frey assay during no stimulation (Baseline), optogenetic stimulation (Stim), and post-stimulation (Recovery) in ChR2 expressing (blue) and GFP control animals (green). GFP: Baseline vs. Stim paired t-test p= 0.9982, t= 0.05559. ChR2: Baseline vs. Stim paired t-test p=0.0166, t=4.218. Interaction: RM 2-way ANOVA p<0.0001, F(2,20)=16.03. n=6 per group.
d) Latency to paw withdrawal in an RHS assay in mice injected with CFA (3 days prior) during no stimulation (Baseline) and optogenetic stimulation (Stim) in ChR2 expressing (blue) and GFP control animals (green). The assay was conducted 3 days after CFA injection GFP: Baseline vs. Stim paired t-test p=0.99, t=0.1297. ChR2: Baseline vs. Stim paired t-test p<0.0001, t=12.58. Interaction: RM 2-way ANOVA p<0.0001, F(1,8)=64.94. n=6 per group.
e) Left: Schematic of a real-time place preference assay demonstrating optogenetic activation when the CFA-injected mouse is in the light-paired chamber and no optogenetic activation when the mouse spontaneously moves to the light-unpaired chamber. The experiment was conducted 3 days after the CFA injection. Right: Time spent by mice in the optogenetic stimulation-/light-paired chamber. ChR2-expressing mice are shown in blue, GFP expressing mice are in green. Sham injections involved intraplantar injection of CFA diluent. GFP: Baseline vs. Stim paired t-test p= 0.5099, t= 1.134. ChR2: Baseline vs. Stim paired t-test p=0.0276, t=3.435. Interaction: RM 2-way ANOVA p=0.0179, F(1,6)=10.44. n=4 per group.

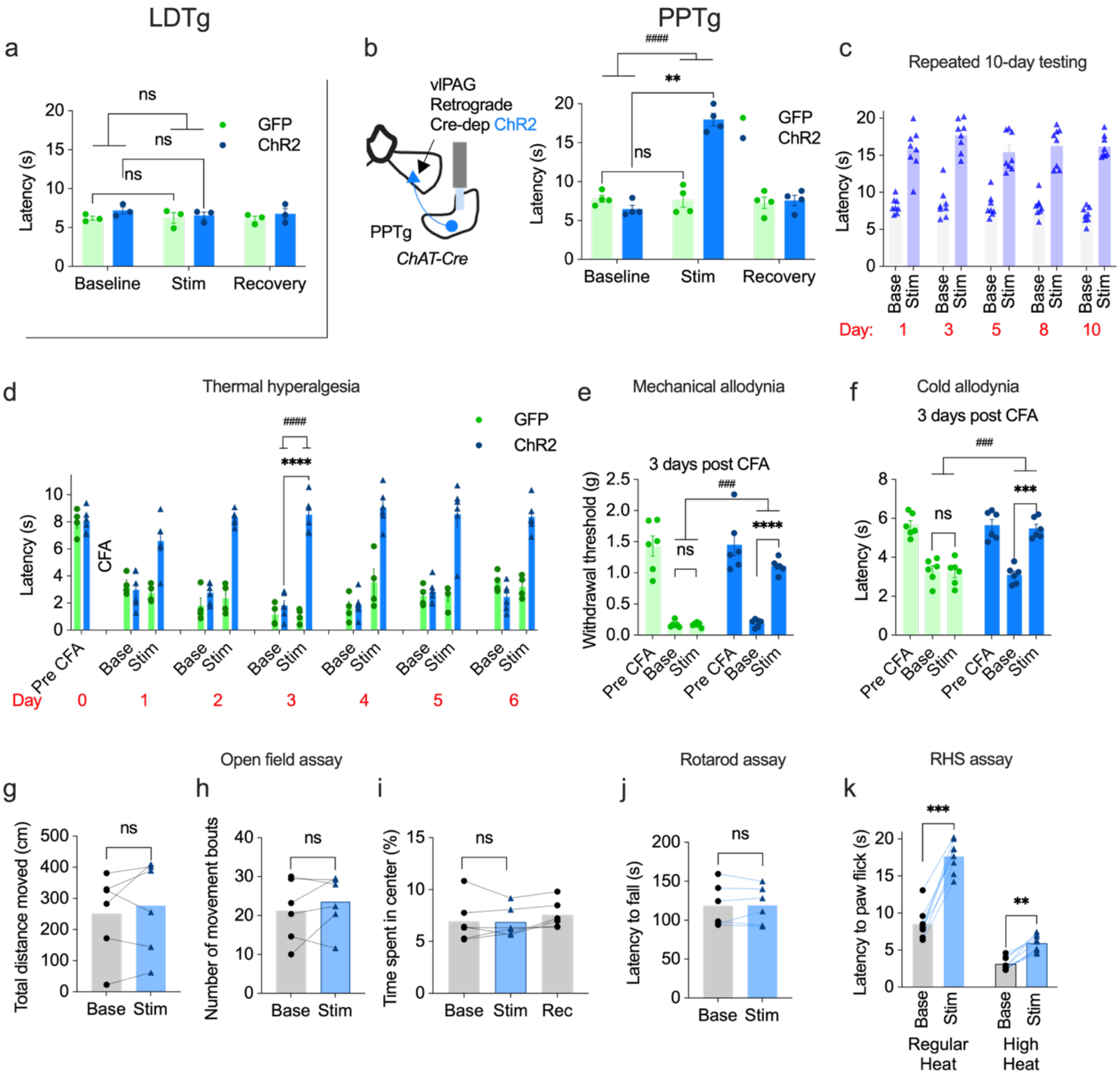

Supp Fig 3: Activating projections from PPTg^{ChAT+} but not LDTg^{ChAT+} to the vlPAG is antinociceptive without altering baseline motor function.

a) In animals expressing ChR2/GFP in LDTg^{ChAT+}→vlPAG projections, latency to paw withdrawal in a RHS assay during no stimulation (Baseline), optogenetic stimulation (Stim), and post-stimulation (Recovery) in ChR2 expressing (blue) and GFP control animals (green). ChR2: Baseline vs. Stim paired t-test p=0.2674, t=2.341.
GFP: Baseline vs. Stim paired t-test p=0.9989, t=0.04618. Interaction: RM 2-way ANOVA p=0.6470, F(2,8)= 0.4600. n=3 per group.
b) Left: Schematic showing injection of retrogradely transported *Cre*-dependent virus expressing ChR2 in the vlPAG and cannula implant in the PPTg for optogenetic activation of PPTg^{ChAT+}→vlPAG projection cell bodies in *ChAT-Cre* mice. Right: Latency to paw withdrawal

Supp Fig 3 (continued): in a RHS assay during no stimulation (Baseline), optogenetic stimulation (Stim), and post-stimulation (Recovery) in ChR2 expressing (blue) and GFP control animals (green). ChR2: Baseline vs. Stim paired t-test p=0.0030, t=11.27. GFP: Baseline vs. Stim paired t-test p=0.9610, t=0.2730. Interaction: RM 2-way ANOVA p<0.0001, F(2,12)=40. n=4 per group.

c) Latency to paw withdrawal in RHS assay conducted over 10 days of repeated testing before (Base, gray bars) and after optogenetic stimulation of PPTg^{ChAT+} terminals in the vlPAG (Stim, blue bars). n=8 per group.

d) Latency to paw withdrawal in RHS assay conducted before (Pre CFA) and after intraplantar CFA injection and optogenetic activation of PPTg^{ChAT+} terminals in the vlPAG. Latencies before and after optogenetic activation are represented as 'Base' and 'Stim', respectively, in ChR2-expressing (blue) and GFP control (green) mice. ChR2: Base vs. Stim paired t-test p<0.0001, t=13.15. Interaction: RM 2-way ANOVA p<0.0001, F(1,8)=55.8. n=4 in GFP group and n=6 in ChR2 group.

e) Paw withdrawal threshold in von Frey assay before (Pre CFA) and after injection of CFA in ChR2 expressing (blue) and GFP control groups (green) during baseline (Base) and after optogenetic activation (Stim) of PPTg^{ChAT+} terminals in the vlPAG. ChR2: Base vs. Stim paired t-test p<0.0001, t=6.276. GFP: Base vs. Stim paired t-test p>0.9999, t=0.01147. Interaction: RM 2-way ANOVA p=0.0002, F(2,20)=13.15. n=6 per group.

f) Latency to paw withdrawal in cold allodynia assay before (Pre CFA) and after injection of CFA in ChR2 expressing (blue) and GFP control groups (green) during baseline (Base) and after optogenetic activation (Stim) of PPTg^{ChAT+} terminals in the vlPAG. ChR2: Base vs. Stim paired t-test p<0.0001, t=6.398. GFP: Base vs. Stim paired t-test p=0.9988, t=0.2640. Interaction: RM 2-way ANOVA p<0.0001, F(2,20)=13.64. n=6 per group.

g) Total distance moved in an open field assay during no-stimulation baseline (Base) and during optogenetic activation of PPTg^{ChAT+} terminals in the vlPAG (Stim). Base vs. Stim paired t-test p=0.4145, t=0.8895. n=6 per group.

h) Number of movement bouts in an open field assay during no-stimulation baseline (Base) and during optogenetic activation of PPTg^{ChAT+} terminals in the vlPAG (Stim). Base vs. Stim paired t-test p=0.3347, t=1.067. n=6 per group.

i) Time spent in the center in an open field assay during no-stimulation baseline (Base), during optogenetic activation of PPTg^{ChAT+} terminals in the vlPAG (Stim), and post-activation recovery (Rec). Base vs. Stim paired t-test p=0.8138, t=0.2482. n=6 per group.

j) Latency to fall in a rotarod assay during no-stimulation baseline (Base) and after optogenetic activation of PPTg^{ChAT+} terminals in the vlPAG (Stim). Base vs. Stim paired t-test p=0.9302, t=0.09212. n=6 per group.

k) Latency to paw withdrawal in RHS assay in regular heat source intensity (Regular Heat) and high heat source intensity (High Heat) in ChR2 expressing groups during baseline (Base) and optogenetic activation (Stim) of PPTg^{ChAT+} terminals in the vlPAG. Regular Heat: Base vs. Stim paired t-test p<0.0001, t=13.79. High Heat: Base vs. Stim paired t-test p<0.0001, t=9.062. n=6 per group.

Optogenetic inhibition of μ-opioid receptor expressing vlPAG neurons vlPAG^{Oprm1+} neurons is antinociceptive post opioid tolerance.

Repeated opioid administration leads to reduced analgesic efficacy[108–110], which is part of the phenomenon known as opioid tolerance. To test how μ-opioid receptor-expressing vlPAG neurons (vlPAG^{Oprm1+}) respond to nocifensive behaviors before and after opioid tolerance, we expressed GCaMP6 in vlPAG^{Oprm1+} neurons using *Oprm1-Cre* mice (Fig 9a). In these mice, we used *in vivo* fiber photometry to measure intracellular calcium changes reflecting changes in neuronal activity (Fig 9b). We found that vlPAG^{Oprm1+} neurons are activated during nocifensive behaviors, such as paw withdrawal from acute nociceptive thermal stimuli in the RHS assay. Also, chronic inflammatory pain state (intraplantar Complete Freund's Adjuvant injection) increased noxious-stimuli evoked fluorescence response amplitude in these neurons, evidenced by increased mean fluorescence (Fig 9b, c) and a higher peak transient amplitude in response to nocifensive stimuli (Fig 9d, e). As expected, morphine (10mg/kg, i.p.) effectively decreased mean fluorescence (Fig 9g, h) and the peak transient amplitude in response to noxious stimuli (Fig 9i, j, black control trace), suggesting that morphine inhibits vlPAG^{Oprm1+} neurons. Exposing mice to an escalating morphine dose regimen (10→30mg/kg over six days; Fig 9f) induced an opioid-tolerant state[108,111], verified by a lack of increase in latency to paw flick after morphine administration (Supp Fig 4a). Morphine doses that inhibited vlPAG^{Oprm1+} neurons in control mice did not inhibit vlPAG^{Oprm1+} neurons in opioid-tolerant mice (Fig 9g-j, red tolerant trace), indicating compromised recruitment of descending pain pathways.

Next, we tested whether direct, cell-autonomous inhibition of vlPAG^{Oprm1+} neurons relieved pain in this opioid-tolerant state. To that end, we expressed the inhibitory opsin, halorhodopsin (eNpHR 3.0), in vlPAG^{Oprm1+} neurons and implanted a fiberoptic cannula in the vlPAG (Fig 9a). Halorhodopsin expression was verified using simultaneous fiber photometry with GCaMP expressed in the same cells. Optogenetic inhibition decreased mean fluorescence (Supp Fig 4b). Optogenetic inhibition of vlPAG^{Oprm1+} neurons in opioid-naïve mice increased latency to paw flick in RHS assay (Fig 9k), effectively recapitulating the behavioral impact of morphine (10 mg/kg). After inducing and verifying opioid tolerance, we observed that optogenetic inhibition of vlPAG^{Oprm1+} neurons still increased the latency to paw flick (Fig 9l). Furthermore, optogenetic inhibition increased latency to paw flick even after naloxone (3mg/kg i.p.) administration (Fig 9m). These observations demonstrate that even in opioid-tolerant animals, inhibiting vlPAG^{Oprm1+} neurons can still relieve pain by recruiting descending pain pathways. In a separate group of CFA-injected animals, we verified that inhibiting vlPAG^{Oprm1+} neurons reduces thermal hyperalgesia associated with chronic inflammatory pain as well (Supp Fig 4c).

Finally, we tested whether activating PPTg^{ChAT+}→vlPAG projections recapitulates these observations and relieves pain in opioid-tolerant mice. Indeed, after opioid tolerance, while morphine lost its analgesic potency, optogenetic activation of PPTg^{ChAT+}→vlPAG projections increased latency to paw flick (Supp Fig 4d, e). Furthermore, activation of PPTg^{ChAT+}→vlPAG projections also relieved pain even after naloxone administration (Supp Fig 4f), demonstrating conserved analgesic potency of activating PPTg^{ChAT+}→vlPAG projections even after opioid tolerance.

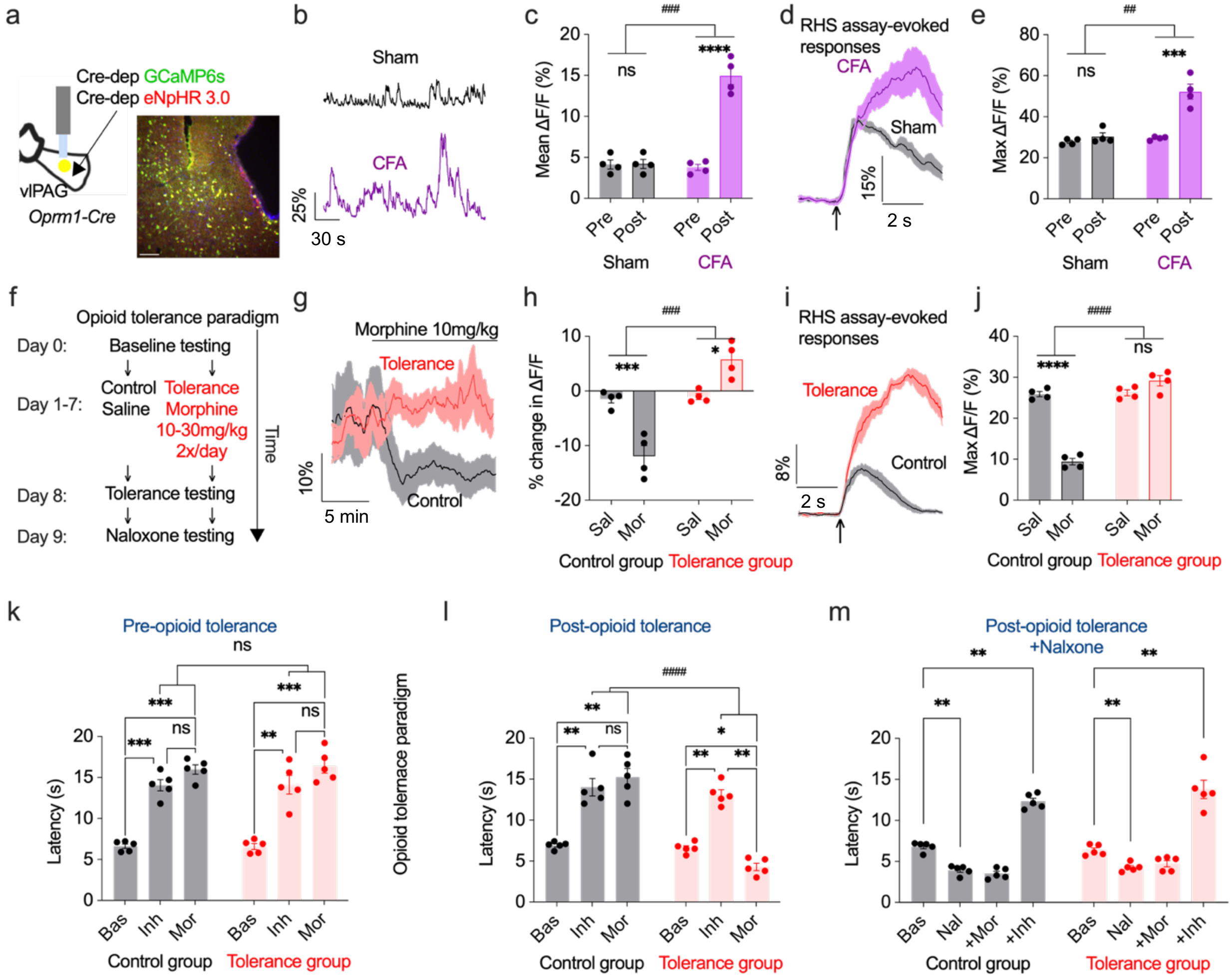

Figure 9: Inhibiting vlPAG^{Oprm1+} neurons is antinociceptive under baseline and opioid-tolerant conditions.

a) Left: Schematic depicting GCaMP6 and eNpHR 3.0 expression in vlPAG^{Oprm1+} neurons and cannula placement in the vlPAG. Right: Fluorescence image showing GCaMP6 (green) and eNpHR 3.0 (red) expression in the vlPAG and nuclear DAPI staining (blue, scale bar: 50µm).
b) Representative GCaMP6 fluorescence traces from vlPAG^{Oprm1+} neurons collected using fiber photometry during open field behavior in CFA-injected (purple) and sham control mice (black). Data collected 3-days after CFA injection.
c) Mean fluorescence in sham control (black) and CFA-injected mice (purple). Sham: Pre vs. Post paired t-test p=0.9976, t=0.06338. CFA: Pre vs. Post paired t-test p<0.0001, t=10.49. Interaction: RM 2-way ANOVA p=0.0003, F(1,6) = 54.34. n=4 per group.
d) Mean vlPAG^{Oprm1+} GCaMP6 fluorescence traces time locked to paw withdrawal (upward arrow) in CFA-injected (purple) and sham control mice (black, 6 traces per animal, n=4).
e) Peak vlPAG^{Oprm1+} GCaMP6 fluorescence transient during RHS-evoked responses in sham control (black) and CFA-injected (purple) mice. Sham: Pre vs. Post paired t-test p=0.6323,

Figure 9 (continued): t=0.9188. CFA: Pre vs. Post paired t-test p=0.0004, t=8.214. Interaction: RM 2-way ANOVA p=0.0021, F(1,6) = 26.61. n=4 per group.

f) Schematic of the tolerance exposure paradigm used in subsequent experiments.

g) Mean vlPAG^{Oprm1+} GCaMP6 fluorescence traces time locked to morphine injection (10mg/kg, i.p.) during open field behavior in mice exposed to opioid tolerance paradigm (red) or control (black).

h) Percent change in vlPAG^{Oprm1+} GCaMP6 fluorescence during 15-20 mins post morphine/saline injection compared to 10-5 mins before morphine injection in mice exposed to opioid tolerance (red) or controls (black). Control: Sal vs. Mor paired t-test p=0.0009, t=6.947. Tolerance: Sal vs. Mor paired t-test p=0.0082, t=4.503. Interaction: RM 2-way ANOVA p=0.0002, F(1,6) = 65.55. n=4 per group.

i) Mean vlPAG^{Oprm1+} GCaMP6 fluorescence traces time locked to paw-withdrawal during RHS assay after morphine (10mg/kg, i.p.) injection in mice exposed to opioid tolerance paradigm (red) or control (black).

j) Peak vlPAG^{Oprm1+} GCaMP6 fluorescence transient during RHS-evoked responses after morphine/saline injection in mice exposed to opioid tolerance (red) or controls (black). Control: Sal vs. Mor paired t-test p<0.0001, t=11.85. Tolerance: Sal vs. Mor paired t-test p=0.1579, t=2.083. Interaction: RM 2-way ANOVA p<0.0001, F(1,6) = 97.04. n=4 per group.

k) Latency to paw withdrawal in RHS assay before opioid tolerance in control and tolerance group under baseline conditions (Bas), during optogenetic inhibition (Inh), and after morphine injection (Mor). Control: Bas vs. Inh p=0.0004, q=19.52. Inh vs. Mor p=0.3072, q=2.421. Bas vs. Mor p=0.0004, q=18.69. Tolerance: Bas vs. Inh p=0.0091, q =8.325. Inh vs. Mor p=0.3591, q=2.208. Bas vs. Mor p=0.0004, q=19.61. Interaction: RM 2-way ANOVA p=0.9462 F(2,16)=0.05553. n=5 per group.

l) Latency to paw withdrawal in RHS assay after opioid tolerance in control and tolerance group under baseline conditions (Bas), during optogenetic inhibition (Inh), and after morphine injection (Mor). Control: Bas vs. Inh p=0.007, q=8.949. Inh vs. Mor p=0.8271, q=0.8503. Bas vs. Mor p=0.0032, q=11.09. Tolerance: Bas vs. Inh p=0.0032, q = 11.05. Inh vs. Mor p=0.0017, q=13.13. Bas vs. Mor p=0.0114, q=7.82. Interaction: RM 2-way ANOVA p<0.0001 F(2,16)=25.54. n=5 per group.

m) Latency to paw withdrawal in RHS assay after opioid tolerance and systemic naloxone injections in control and tolerance groups under baseline conditions (Bas), after naloxone (Nal) and morphine administration (Mor), and during optogenetic inhibition (Inh). Control: Bas vs. Nal p=0.0084, q=8.625. Bas vs. Inh p=0.0023, q=13.5. Tolerance: Bas vs. Nal p=0.0025, q = 13.23. Bas vs. Inh p=0.0051, q=11.01. n=5 per group.

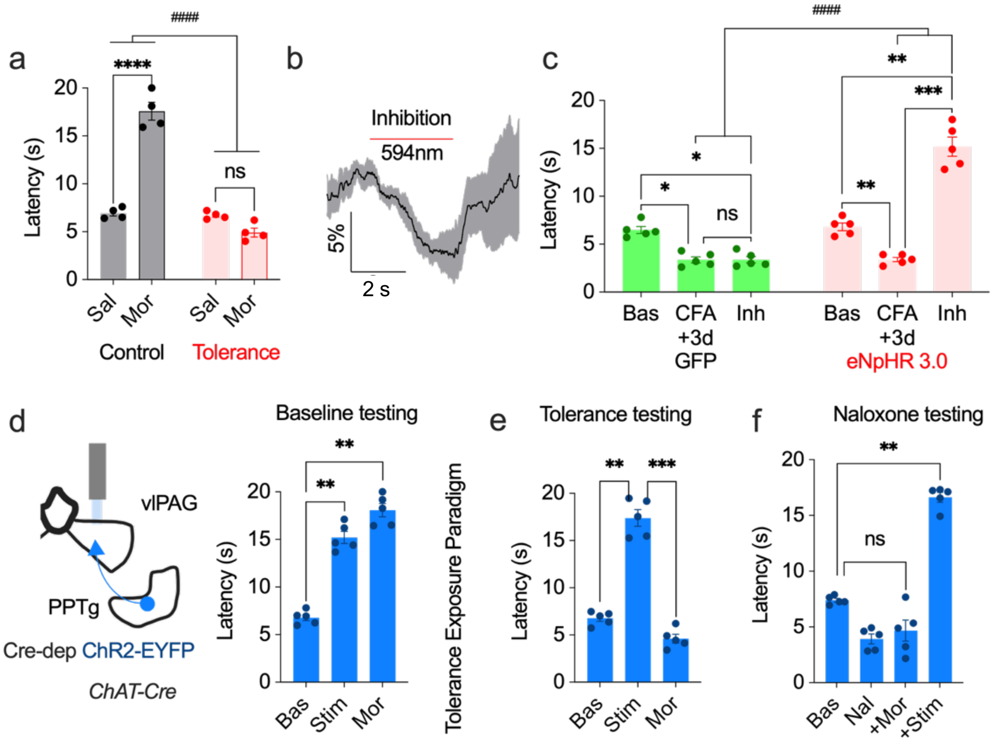

Supp Fig 4: Inhibiting vlPAG^{Oprm1+} or activating PPTg^{ChAT+}→vlPAG projections is antinociceptive under baseline and opioid-tolerant conditions.

a) Latency to paw withdrawal in RHS assay after opioid tolerance post saline (Sal) and morphine (10mg/kg, Mor) administration in control (grey) and tolerance (red) groups. Control: Sal vs. Mor paired t-test p=0.0009, t=6.947. Tolerance: Sal vs. Mor paired t-test p=0.0082, t=4.503. Interaction: RM 2-way ANOVA p=0.0002, F(1,6) = 65.55. n=4 per group.
b) Mean vlPAG^{Oprm1+} GCaMP6 fluorescence (black trace) collected using simultaneous optogenetics and fiber photometry time locked to optogenetic inhibition of vlPAG^{Oprm1+} neurons (1 trace per animal, n=8).
c) Latency to paw withdrawal before (Bas) and after intraplantar CFA injection (CFA and Inh) in mice expressing GFP (green) or eNpHR 3.0 (red) in vlPAG^{Oprm1+} neurons. CFA+3d refers to 3 days post intraplantar CFA injection, and Inh refers to optogenetic inhibition of vlPAG^{Oprm1+} neurons. GFP: Bas vs. CFA paired t-test p=0.0009, t=6.947. CFA vs. Inh paired t-test p=0.0009, t=6.947. Bas vs. Inh paired t-test p=0.0009, t=6.947. eNpHR 3.0: Bas vs. Mor paired t-test p=0.0082, t=4.503. CFA vs. Inh paired t-test p=0.0009, t=6.947. Bas vs. Inh paired t-test p=0.0009, t=6.947. Interaction: RM 2-way ANOVA p=0.0002, F(1,6) = 65.55. n=4 per group.
d) Left: Schematic showing *Cre*-dependent ChR2 expression in PPTg of *ChAT-Cre* animals and cannula placement in the vlPAG. Right: Latency to paw withdrawal in RHS assay before opioid tolerance under baseline conditions (Bas), during optogenetic stimulation (Stim), and after morphine injection (Mor). Bas vs. Stim: paired t-test p=0.0004, t=19.52. Bas vs Mor: paired t-test p=0.3072, t=2.421. n=5 per group.

Supp Fig 4 (continued): e) Latency to paw withdrawal in RHS assay after opioid tolerance under baseline conditions (Bas), during optogenetic stimulation (Stim), and after morphine injection (Mor). Bas vs. Stim: paired t-test p=0.0004, t=19.52. Stim vs Mor: paired t-test p=0.3072, t=2.421. n=5 per group.

f) Latency to paw withdrawal in RHS assay after opioid tolerance and systemic naloxone injections under baseline conditions (Bas), after naloxone (Nal) and morphine administration (Mor), and during optogenetic stimulation (Stim). Bas vs. Stim: paired t-test p=0.0004, t=19.52. Stim vs. Mor: paired t-test p=0.3072, t=2.421. n=5 per group.

Activation of α7 nAChRs in the vlPAG is analgesic.

α7 nAChRs mediate the analgesic effects of activating PPTg^{ChAT+}→vlPAG projections

We then explored the underlying cholinergic receptors mediating these antinociceptive effects. First, we assayed AChR mRNA expression in the vlPAG using Fluorescent *In Situ* Hybridization (FISH) (Fig 10a, Supp Fig 5a)[112]. We observed strong expression of α7 nAChR (*Chrna7*) mRNA and M2 mAChR (*Chrm2*) mRNA in the vlPAG and weak expression of M4 mAChR (*Chrm4*) mRNA (Fig 10a, Supp Fig 5a). Using circuit-specific optogenetic stimulation and AChR pharmacology, we tested the involvement of AChRs in the antinociceptive effects of activating PPTg^{ChAT+}→vlPAG projections. Here, we sequentially injected antagonists of various AChRs before activating PPTg^{ChAT+}→vlPAG projections. We found that the systemic administration of α7 nAChR antagonists (MLA 6mg/kg) and produced the most robust reduction in antinociceptive effects (Fig 10b). Interestingly, pan-muscarinic (atropine 10mg/kg) and M2 mAChR antagonist (AFDX-116 3mg/kg) altered baseline latencies to paw flick without changing the antinociceptive effects of activating this circuit (Fig 10b). Given that the AChR antagonists may alter signaling in other brain regions, we verified our observations by focally infusing the α7 nAChR antagonist, methyllycaconitine (MLA), into the vlPAG and testing for antinociceptive effects of activating the circuit. These experiments revealed that while baseline pain sensitivity was unaltered by α7 nAChR antagonist, the antinociceptive effects of activating PPTg^{ChAT+}→vlPAG projections were effectively blocked following MLA infusion into the vlPAG (Fig 10c). Together, these observations implicate α7 nAChRs as the mediator of the antinociceptive effects of activating this cholinergic circuit. Interestingly, the higher affinity M2 mAChRs appear to mediate baseline pain sensitivity, likely due to baseline cholinergic tone.

To test if α7 nAChRs also mediated synaptic communication between PPTg^{ChAT+} and vlPAG neurons, we used brain slice electrophysiology with optogenetics. We expressed ChR2 in PPTg^{ChAT+} terminals and took brain slices to record from vlPAG neurons in regions where the densest innervation was observed (Fig 10d). We observed that optogenetic stimulation of PPTg^{ChAT+} terminals evoked rapid inward currents in 71% of the recorded vlPAG neurons (n=17 neurons, 6 mice, Fig 10e). These synaptic currents were blocked by MLA (10nM) and recovered after washout (Fig 10f). In a subset of these experiments, we also observed that another highly selective α7 nAChR antagonist, α-bungarotoxin (100 nM), irreversibly blocked these synaptic currents (Supp Fig 5b). The ionotropic glutamate antagonist, CNQX (20 μM), did not affect optically evoked EPSC amplitudes (Supp Fig 5c). These observations demonstrate functional fast cholinergic synaptic transmission which is a rare observation within the CNS[13,15,16,113,114].

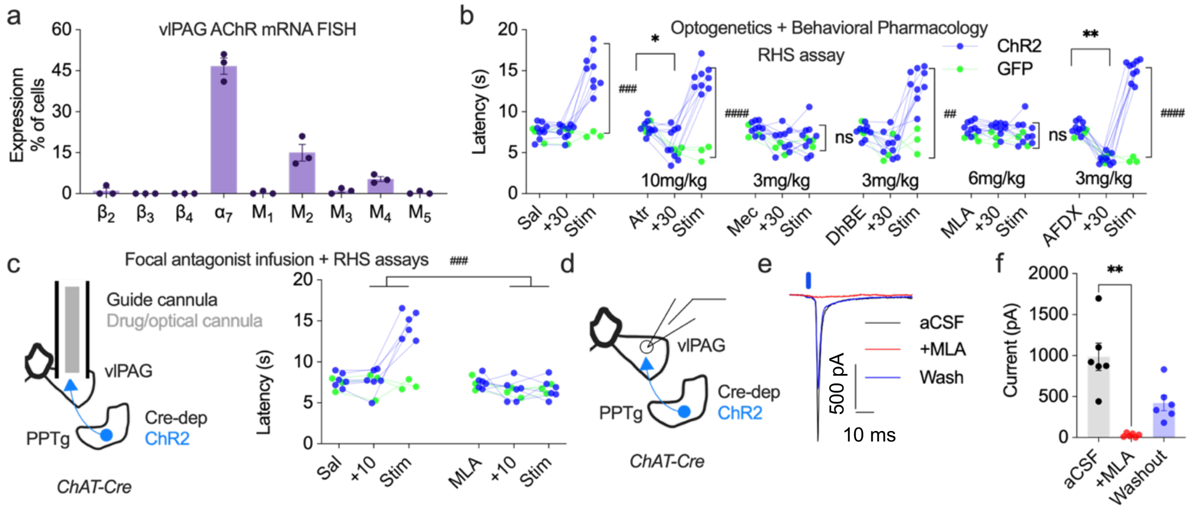

Figure 10: Antinociceptive effects of activating PPTg^{ChAT+}→vlPAG projections are mediated through α7 nAChRs.

a) Expression of AChR mRNA on vlPAG cells explored using fluorescence *in situ* hybridization (FISH). Six representative vlPAG images were taken per mouse, and the percent mRNA-positive cells per image were averaged. n=3.
b) Latency to paw withdrawal during RHS assay for mice injected with ChR2 (blue) or GFP (green) in PPTg^{ChAT+} neurons before drug injection and vlPAG terminal stimulation (drug name),

Figure 10 (continued): 30 mins after systemic drug injection (+30) and after optogenetic stimulation of terminals (Stim). Drugs and their concentrations are listed on the x-axis. Sal: GFP: Baseline vs. Stim paired t-test p>0.9999, t=0.000. ChR2: Baseline vs. Stim paired t-test p<0.0001, t=10.15. Interaction: RM 2-way ANOVA p=0.0005, F(1,10)=25.74. Atr: GFP: Baseline vs. Stim paired t-test p=0.9420, t=0.315. ChR2: Baseline vs. Stim paired t-test p<0.0001, t=13.02. Interaction: RM 2-way ANOVA p<0.0001, F(1,10)=46.04. Mec: GFP: Baseline vs. Stim paired t-test p=0.6445, t=0.8718. ChR2: Baseline vs. Stim paired t-test p=0.8939, t=0.4329. Interaction: RM 2-way ANOVA p=0.6020, F(1,10)=0.2901.

DhBE: GFP: Baseline vs. Stim paired t-test p=0.7752, t=0.6572. ChR2: Baseline vs. Stim paired t-test p<0.0001, t=7.556. Interaction: RM 2-way ANOVA p=0.0093, F(1,10)=10.30. MLA: GFP: Baseline vs. Stim paired t-test p>0.9999, t=0.000. ChR2: Baseline vs. Stim paired t-test p=0.6308, t=0.8938. Interaction: RM 2-way ANOVA p=0.6645, F(1,10)=0.1997. AFDX: GFP: Baseline vs. Stim paired t-test p=0.9210, t=0.3701. ChR2: Baseline vs. Stim paired t-test p=<0.0001, t=25.22. Interaction: RM 2-way ANOVA p<0.0001, F(1,10)=167.2. n=9 ChR2, 3 GFP.

c) Left: a schematic showing strategy for PPTg^{ChAT+} terminal activation along with focal drug infusion. Right: Latency to paw withdrawal in a RHS assay in mice expressing ChR2 (blue) or GFP (green) in PPTg^{ChAT+} terminals in the vlPAG. RHS assay was conducted before drug administration (drug name), 10 min after focal drug infusion (+10), and after optogenetic stimulation (Stim). Sal: GFP: +10 vs. Stim paired t-test p=0.9996. ChR2: +10 vs. Stim paired t-test p=<0.001. MLA: GFP: +10 vs. Stim paired t-test p>0.9999. ChR2: +10 vs. Stim paired t-test p<0.0001. RM 3-way ANOVA +10 vs. Stim x Sal vs. MLA x ChR2 vs. GFP p =0.0006, F(1,28)=14.75. n=6 ChR2, 3 GFP.

d) Slice electrophysiology schematic. ChR2-expressing PPTg^{ChAT+} terminals were activated during voltage-clamp recordings (-70mV) from vlPAG neurons to monitor optogenetically evoked synaptic currents.

e) Representative traces from one recording demonstrating PPTg^{ChAT+} terminal activation-evoked inward current that is blocked by bath application of α7 nAChR antagonist MLA (10nM).

f) Current amplitude of optically evoked synaptic responses before, during, and after MLA (10nM) bath perfusion. PPTg^{ChAT+} terminals were optogenetically activated using 5ms 473nm pulses, and vlPAG neurons were recorded. RM ANOVA F(1.342, 6.710)=19.09, p=0.0026; Tukey's: aCSF vs. MLA p = 0.0056,q=7.979, MLA vs. Washout p = 0.0152, q=6.3. n=6 cells, 4 mice.

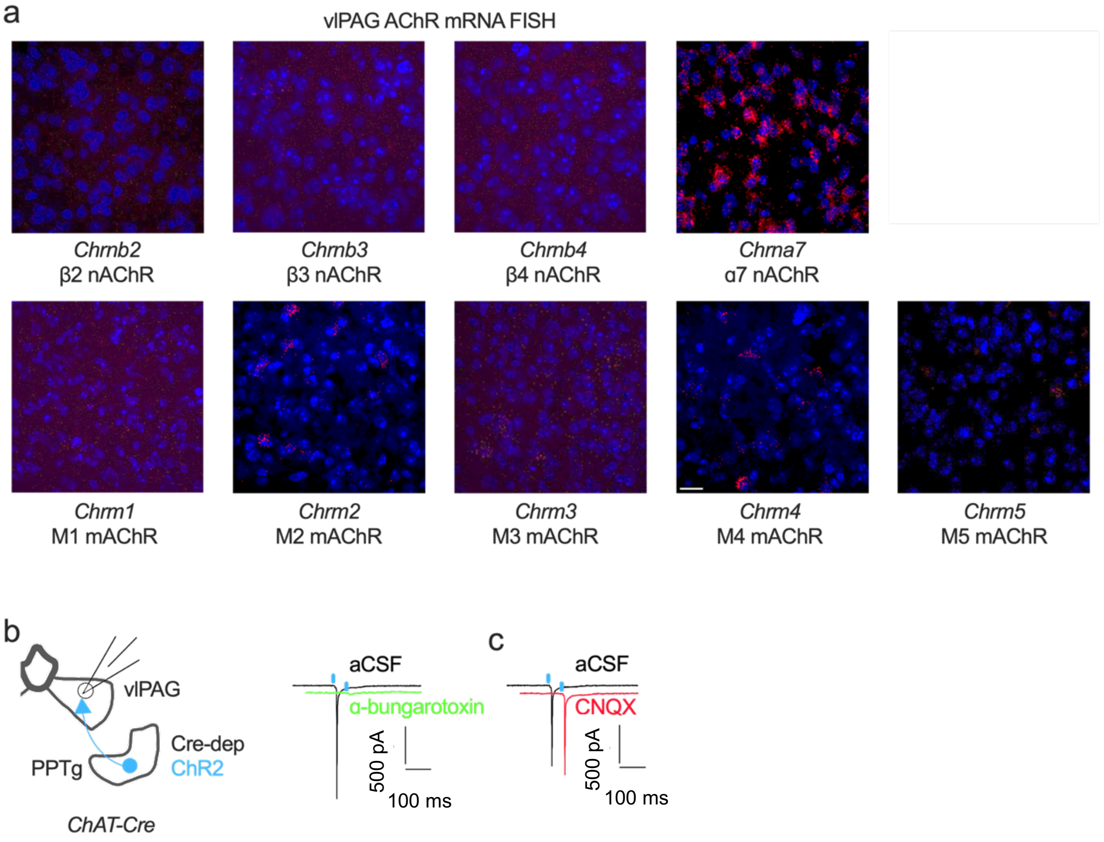

Supp Fig 5: Functional cholinergic synaptic transmission between PPTg^{ChAT+} and vlPAG is mediated through α7 nAChRs

a) Representative fluorescence images of AChR mRNA expression (red) in the vlPAG using fluorescence in situ hybridization with nuclear DAPI stain (blue, common scale bar: 20µm).
b) Left: Slice electrophysiology schematic. ChR2-expressing PPTg^{ChAT+} terminals were activated during voltage-clamp recordings (-70mV) from vlPAG neurons to monitor optogenetically-evoked synaptic currents. Right: Representative traces demonstrating PPTg^{ChAT+} terminal activation-evoked inward current is blocked by bath application of α7 nAChR antagonist α-bungarotoxin (100nM, +20 min).
c) Representative traces demonstrating PPTg^{ChAT+} terminal activation-evoked inward current that is not altered by bath application of AMPAR antagonist CNQX (20µM).

vlPAG$^{Chrna7+}$ neurons are activated during nocifensive behaviors in response to noxious stimuli.

Given that α7 nAChRs mediated the analgesic effects of activating PPTg^{ChAT+}→vlPAG projections, we sought to explore the changes in the physiology of vlPAG$^{Chrna7+}$ neurons during exposure to nociceptive stimuli. First, we used *in vivo* fiber photometry to monitor intracellular calcium dynamics representative of neuronal activity, targeted to α7 nAChR-expressing neurons using a *Chrna7-Cre* mouse line and *Cre*-dependent expression of GCaMP6 in vlPAG$^{Chrna7+}$ neurons (Fig 11a). We observed increases in fluorescence indicating that vlPAG$^{Chrna7+}$ neurons were activated by noxious stimuli that elicited nocifensive behaviors selectively, including hot (55°C) and cold (2°C) water, von Frey filaments (>1.4g), radiant heat, noxious pinprick, and acetone (Fig 11b). These neurons were not strongly activated by other non-noxious stimuli, including somatosensory, visual, olfactory, or auditory stimuli. Interestingly, these neurons were weakly activated by intraoral administration of sucrose and quinine, suggesting potential modulation of a subset of vlPAG$^{Chrna7+}$ neurons by salient gustatory stimuli (Fig 11b).

Given that acute nociceptive stimuli activate vlPAG$^{Chrna7+}$ neurons, we investigated how chronic pain states alter the physiology of these neurons. Intraplantar CFA injections were administered to induce a chronic inflammatory pain state. Using *in vivo* fiber photometry, we observed that CFA injection increased RHS-evoked transient amplitudes and higher mean fluorescence intensity, indicating elevated activity of vlPAG$^{Chrna7+}$ neurons compared to sham controls (Fig 11c, d). To identify the cellular basis of this maladaptive plasticity, we used *in vitro* slice electrophysiology to record from fluorescently labeled vlPAG$^{Chrna7+}$ neurons in brain slices from CFA-injected mice. We observed minimal differences between CFA and control neurons in intrinsic excitability parameters, including resting membrane potential, action potential threshold, and current-firing rate relationship (Supp Fig 6a). Interestingly, we observed a significantly stronger excitatory synaptic drive to these vlPAG$^{Chrna7+}$ neurons in tissue slices from animals in a chronic pain state compared to sham controls, as evidenced by increased frequency of sEPSCs (Fig 11e, f). However, no difference in the inhibitory drive was seen (comparing frequency and amplitude of sIPSCs, Supp Fig 6b). These observations suggest that the increased excitability of vlPAG$^{Chrna7+}$ neurons in chronic pain conditions is mediated by either a change in presynaptic release probability at excitatory inputs or an increased number of excitatory dendritic connections. Along with a reduced cholinergic input, chronic pain-induced maladaptive hyperexcitability of vlPAG$^{Chrna7+}$ neurons is mediated through an aberrant excitatory synaptic drive. Furthermore, these observations suggest that inhibiting vlPAG$^{Chrna7+}$ neurons relieves pain. This is somewhat counterintuitive, as activation of α7 nAChRs should have excitatory effects in these neurons. Thus, we used in vivo optogenetics to test the causal relationship between the activity of vlPAG$^{Chrna7+}$ neurons and nocifensive behaviors.

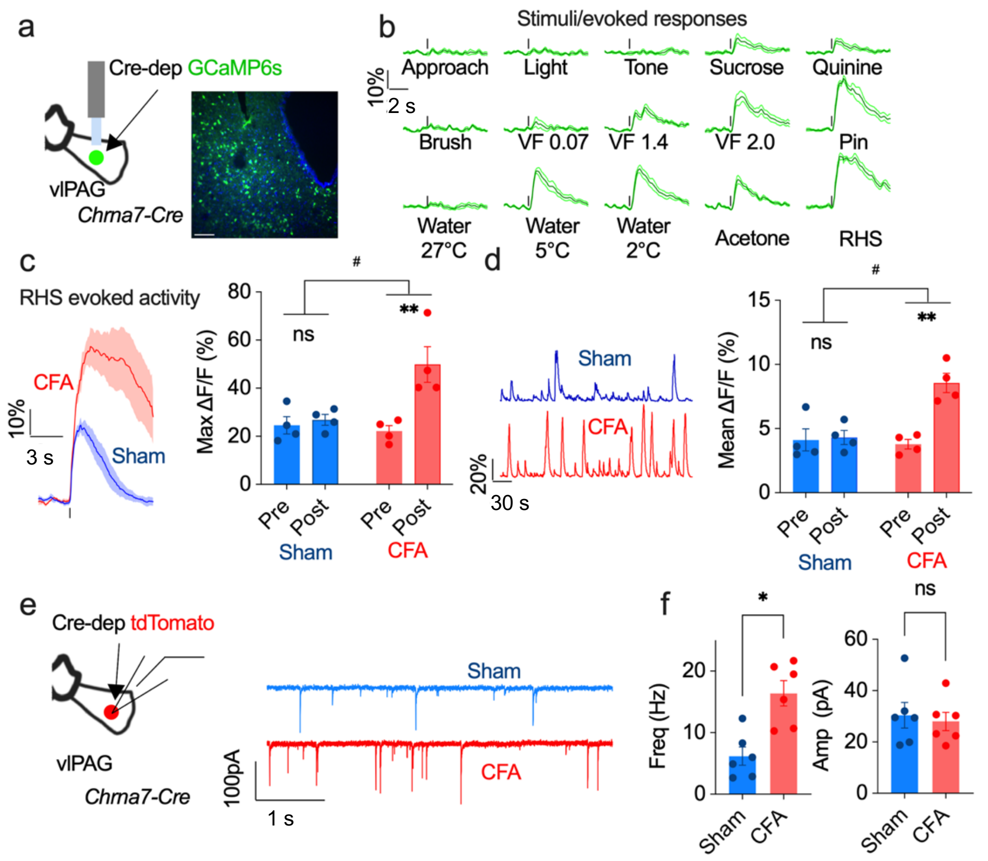

Figure 11: vlPAG$^{Chrna7+}$ neurons are preferentially activated by noxious stimuli.

a) Left: schematic depicting GCaMP6 expression in vlPAG$^{Chrna7+}$ neurons and cannula placement in the vlPAG. Right: fluorescence image showing GCaMP6 (green) expression in the vlPAG and nuclear DAPI staining (blue, scale bar: 50µm).
b) Mean vlPAG$^{Chrna7+}$ GCaMP6 fluorescence traces time locked (vertical line) to either stimuli presentation (approach, light, tone) or behavioral response (all others) collected using fiber photometry (6 traces per animal, n=8).
c) Left: mean vlPAG$^{Chrna7+}$ GCaMP6 fluorescence traces time locked (vertical line) to paw-withdrawal during RHS assay after in sham control (blue) and CFA-injected mice (red, 6 traces per animal, n=4 per group). Right: max vlPAG$^{Chrna7+}$ GCaMP6 fluorescence transient during RHS-evoked responses in sham control (blue) and CFA-injected (red) mice. Recordings were conducted 3 days after injection. Sham: Pre vs. Post paired t-test p=0.4426, t=0.8934. CFA: Pre vs. Post paired t-test p=0.0032, t=5.448. RM 2-way ANOVA p=0.0122, F(1,6) = 12.53. n=4 per group.
d) Left: representative vlPAG$^{Chrna7+}$ GCaMP6 fluorescence traces during open field behavior in CFA-injected (red) and sham control (blue) mice. Right: mean fluorescence in sham control (blue) and CFA-injected (red) mice. Sham: Pre vs. Post paired t-test p=0.9250, t=0.3585. CFA: Pre vs. Post paired t-test p=0.0014, t=4.52. RM 2-way ANOVA p=0.0259, F(1,6) = 8.652. n=4 per group.

Figure 11 (continued): e) Left: schematic showing slice electrophysiology conducted from fluorescently labeled vlPAG$^{Chrna7+}$ neurons using *Cre*-dependent tdTomato expression in *Chrna7-Cre* mice. Right: representative voltage-clamp recordings (-70mV, Cl$^-$ reversal ~-70mV, Cs$^+$ internal) to monitor spontaneous EPSCs from CFA-injected and sham-control animals 3 days after injection.

f) Frequency and amplitude of sEPSCs recorded from vlPAG$^{Chrna7+}$ neurons in vlPAG slices taken from mice after CFA or sham injections. Freq: CFA vs. Sham KS test: p=0.026 D=0.8333. Amp CFA vs. Sham KS test: p>0.9999 D=0.1667. n=6 cells, 5 mice.

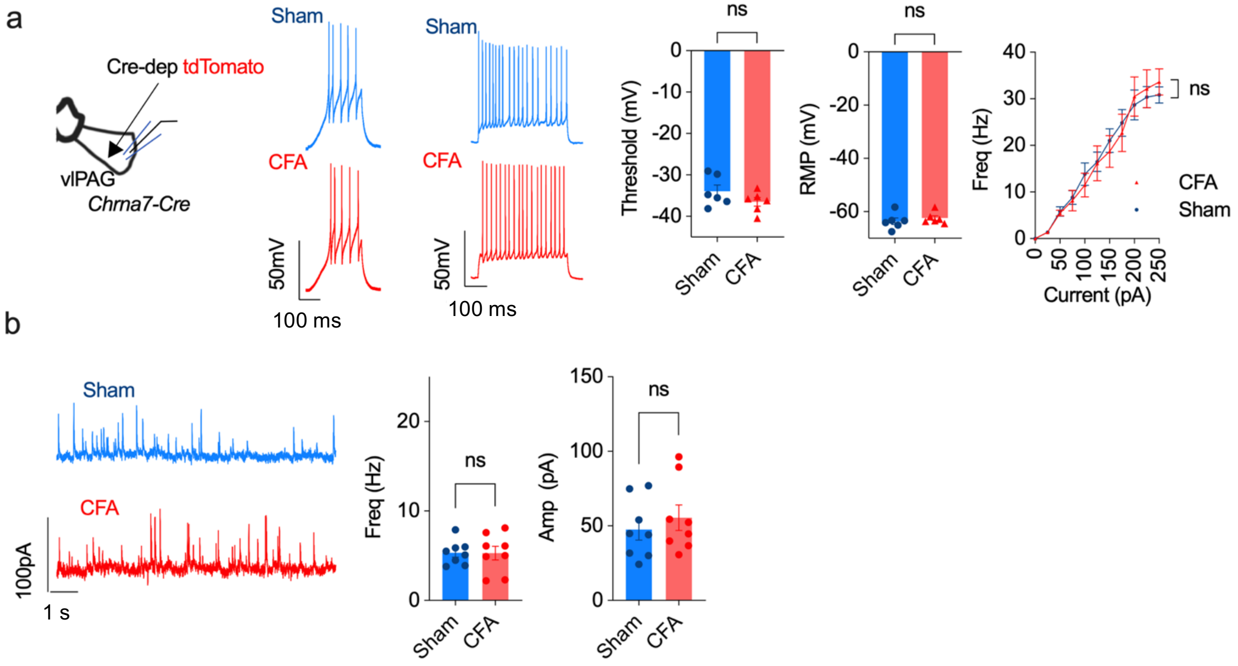

Supp Fig 6: Intrinsic properties of and inhibitory synaptic transmission to vlPAG$^{Chrna7+}$ neurons are unaltered by chronic inflammatory pain conditions.

a) Left to right: Slice electrophysiology schematic. vlPAG$^{Chrna7+}$ neurons were fluorescently labeled with tdTomato using viral surgeries. Representative voltage traces in response to the ramp and step current injections 3 days after intraplantar sham (blue) or CFA (red) injections. Action potential threshold and resting membrane potential (RMP) after Sham or CFA injections. Current-firing rate relationship after Sham or CFA injections. Threshold: Sham vs. CFA t-test p = 0.1933, t= 1.395. RMP: Sham vs. CFA t-test p= 0.4446, t= 0.7959. Current-firing rate: Sham vs. CFA KS test p-value 0.9934 KS D=0.1818. n= 6 neurons recorded from 4 mice for the Sham group and 6 neurons recorded from 5 mice for the CFA group.

b) Left to right: Representative spontaneous IPSC traces recorded from vlPAG$^{Chrna7+}$ neurons in voltage clamp (0mV, Cl$^-$ reversal ~-70mV) 3-days after intraplantar sham (blue) or CFA (red) injections. Mean sIPSC amplitude and frequency monitored from vlPAG$^{Chrna7+}$ neurons. Frequency: Sham vs. CFA t-test p = 0.9675, t= 0.04146 Amplitude: Sham vs. CFA t-test p= 0.4848, t= 0.7177. n= 8 neurons recorded from 4 mice for the Sham group and 8 neurons recorded from 3 mice for the CFA group.

Inhibiting vlPAG$^{Chrna7+}$ neurons is antinociceptive, despite opioid tolerance.

Given that pain states induce maladaptive hyperexcitability in vlPAG$^{Chrna7+}$ neurons, we hypothesized that inhibiting these cells would relieve pain. To test this hypothesis, we expressed inhibitory halorhodopsin (eNpHR 3.0) on vlPAG$^{Chrna7+}$ neurons and implanted an optical cannula in vlPAG (Fig 12a). Optogenetic inhibition of these neurons increased the latency to paw flick in acute thermal pain assays (Fig 12b). Conversely, activating vlPAG$^{Chrna7+}$ neurons using ChR2 was pronociceptive (Fig 12c), suggesting bidirectional pain modulation by vlPAG$^{Chrna7+}$ neurons. In a chronic inflammatory pain state following CFA injection into the hind paw, inhibiting vlPAG$^{Chrna7+}$ neurons increased latency to paw flick in RHS assay and increased paw withdrawal threshold in von Frey assay, consistent with reduced noxious stimulation-induced thermal hyperalgesia and mechanical allodynia (Fig 12d, Supp Fig 7a). Furthermore, inhibiting these neurons was antinociceptive in opioid-tolerant animals, even after administration of the opioid antagonist, naloxone (Supp Fig 7b).

In mice subjected to repeated opioid injections, naloxone administration induces somatic withdrawal signs, including jumping and rearing behaviors[115–119]. Optogenetic inhibition of vlPAG$^{Chrna7+}$ neurons during naloxone-precipitated opioid withdrawal reduced these somatic signs (Supp Fig 7c). It is also important to note that, similar to the effects of activating PPTg cholinergic inputs to vlPAG, inhibiting the activity of vlPAG$^{Chrna7+}$ neurons did not affect locomotor activity, anxiety or motivated behaviors using methods described above (Supp Fig 7d). Also, in line with previous experiments inhibiting these neurons relieved the affective component of chronic inflammatory pain (Supp Fig 7e)[120].

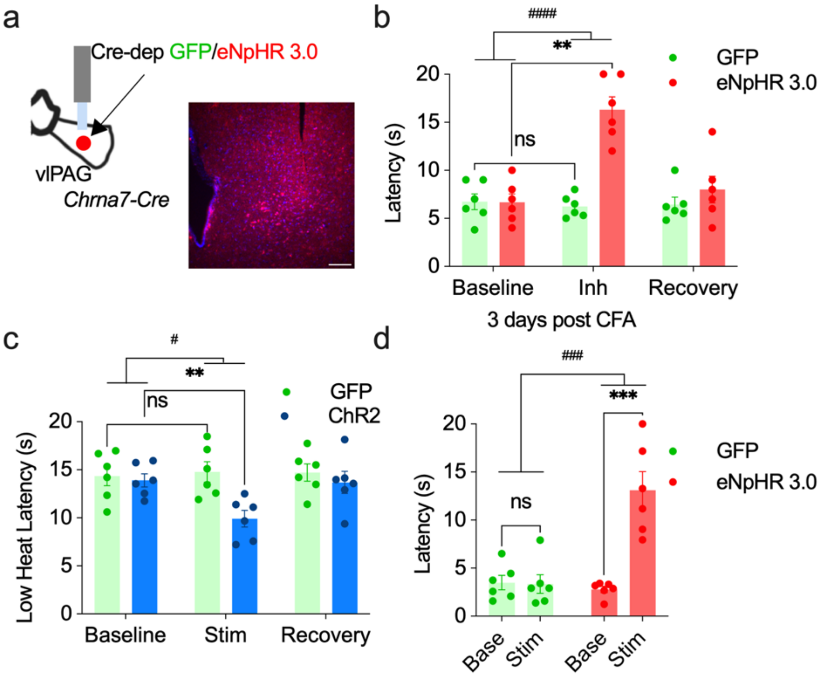

Figure 12: Inhibiting vlPAG$^{Chrna7+}$ neurons is antinociceptive.

a) Left: Schematic showing *Cre*-dependent eNpHR3.0 (or GFP) expression in vlPAG of *Chrna7-Cre* mice and cannula placement in the vlPAG. Right: Fluorescence image showing eNpHR3.0-mCherry expression in vlPAG$^{Chrna7+}$ neurons (red) with nuclear DAPI stain (blue, scale bar 50µm).
b) Latency to paw withdrawal in a RHS assay during no stimulation Baseline, optogenetic Inhibition, and post-inhibition Recovery in eNpHR 3.0 expressing (red) and GFP control animals (green). GFP: Baseline vs. Stim paired t-test p= 0.8669, t= 0.5047. eNpHR 3.0: Baseline vs. Stim paired t-test p<0.0011, t=7.864. Interaction: RM 2-way ANOVA p<0.0001, F(2,20)=27.88. n=6 per group.
c) In mice expressing ChR2 in vlPAG$^{Chrna7+}$ neurons, latency to paw withdrawal in a RHS assay during no stimulation Baseline, optogenetic Stimulation, and post-stimulation Recovery in ChR2 expressing (blue) and GFP control animals (green). This assay was conducted in decreased heat intensity with 20Hz stimulation. GFP: Baseline vs. Stim paired t-test p= 0.8461, t= 0.5474. ChR2: Baseline vs. Stim paired t-test p=0.0026, t=6.485. Interaction: RM 2-way ANOVA p=0.0309, F(2,20)=4.16. n=6 per group.
d) In mice expressing eNpHR 3.0 in vlPAG$^{Chrna7+}$ neurons, latency to paw withdrawal in a RHS assay conducted in mice injected with CFA (3 days prior) during no stimulation Baseline, optogenetic Inhibition and post-inhibition Recovery in eNpHR 3.0 expressing (red) and GFP control animals (green). GFP: Baseline vs. Stim paired t-test p=0.9954, t=0.08681. eNpHR 3.0: Baseline vs. Stim paired t-test p<0.0001, t=6.492. Interaction: RM 2-way ANOVA p=0.0009, F(1,8)=21.64. n=6 per group.

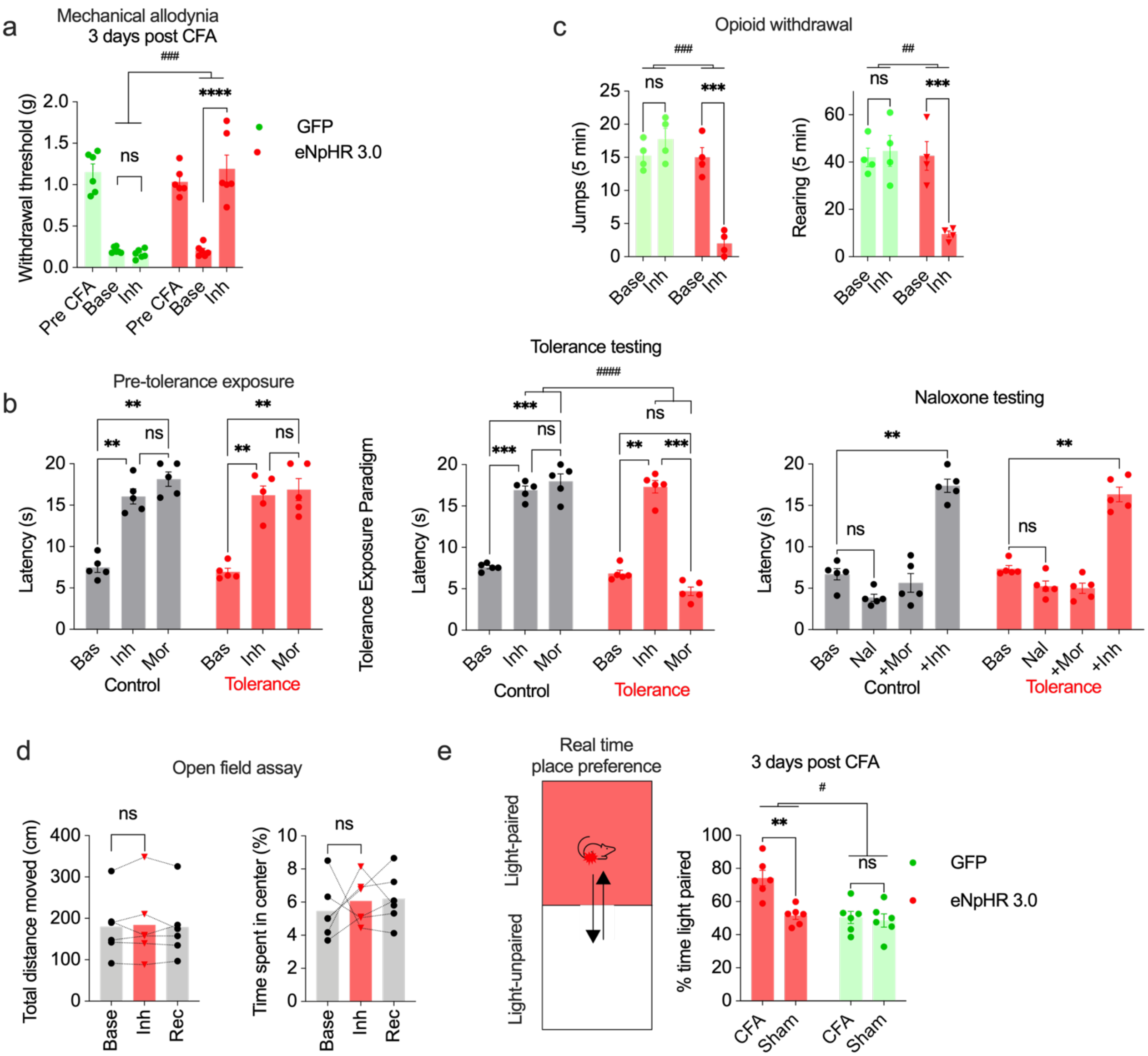

Supp Fig 7: Optogenetic inhibition of vlPAG$^{Chrna7+}$ neurons is antinociceptive in acute and chronic pain conditions and does not alter motor function.

a) Paw withdrawal threshold in von Frey assay before (Pre CFA) and after injection of CFA in GFP control (green) and eNpHR 3.0 expressing groups (red) during baseline (Base) and after optogenetic inhibition (Inh) of vlPAG$^{Chrna7+}$ neurons. In GFP group, inhibition refers to light delivery. GFP: Bas vs. Inh paired t-test p=0.0009, t=6.947. eNpHR 3.0: Base vs. Inh paired t-test p=0.0082, t=4.503. Interaction: RM 2-way ANOVA p=0.0002, F(1,6) = 65.55. n=6 per group.
b) Left: latency to paw withdrawal in RHS assay before opioid tolerance under baseline conditions (Bas), during optogenetic inhibition (Inh), and after morphine injection (Mor) in control (gray) and tolerance group (red). Control: Bas vs. Inh: paired t-test p=0.0011, t=11.08. Inh vs. Mor: paired t-test p=0.9330, t=5.910. Bas vs. Mor: paired t-test p=0.0015, t=10.34. Tolerance: Bas vs. Inh: paired t-test p=0.0036, t=8.210. Inh vs. Mor: paired t-test p=0.9904,

Supp Fig 7 (continued): t=0.2878. Bas vs. Mor: paired t-test p=0.0035, t=8.276. Middle: Latency to paw withdrawal in RHS assay after opioid tolerance under baseline conditions (Bas), during optogenetic inhibition (Inh), and after morphine injection (Mor) in control (gray) and tolerance group (red). Control: Bas vs. Inh: paired t-test p=0.0004, t=14.14. Inh vs. Mor: paired t-test p=0.8421, t=0.8176. Bas vs. Mor: paired t-test p=0.0006, t=12.84. Tolerance: Bas vs. Inh: paired t-test p=0.0024, t=9.101. Inh vs. Mor: paired t-test p=0.0005, t=13.34. Bas vs. Mor: paired t-test p=0.0896, t=3.269. Interaction: RM 2-way ANOVA p<0.0001, F(1,8)=63.60. Right: Latency to paw withdrawal in RHS assay after opioid tolerance and systemic naloxone injections under baseline conditions (Bas), after naloxone (Nal) and morphine administration (Mor), and during optogenetic Inhibition (Inh) in control (gray) and tolerance group (red). Control: Bas vs. Nal: paired t-test p=0.1440, t=3.470. Bas vs. +Inh: paired t-test p=0.0016, t=12.02. Tolerance: Bas vs. Nal: paired t-test p=0.2581, t=2.805. Bas vs. +Inh: paired t-test p=0.0069, t=8.296. n=5 per group.

c) Opioid-exposed animals (6 days, 2x/day 10→30mg/kg) were administered naloxone, and subsequent jumping (left) and rearing (right) behaviors were monitored in GFP (green) and eNpHR 3.0 (red) expressing mice before (Base) and after optogenetic inhibition (Inh) of vlPAG$^{Chrna7+}$ neurons. In GFP group, inhibition refers to light delivery.

Jumping: GFP: Base vs. Inh paired t-test p=0.3954, t=1.361. eNpHR 3.0: Base vs. Inh paired t-test p=0.0008, t=7.076. Interaction: RM 2-way ANOVA p=0.0010, F(1,6)=35.5. Rearing: GFP: Base vs. Inh paired t-test p=0.8236, t=0.5848. eNpHR 3.0: Base vs. Inh paired t-test p=0.0008, t=7.017. Interaction: RM 2-way ANOVA p=0.0017, F(1,6)=28.9. n=4 per group.

d) Total distance moved (left) and time spent in center (right) in an open field assay during no-stimulation baseline (Base), during optogenetic inhibition of vlPAG$^{Chrna7+}$ neurons (Inh), and during post-inhibition recovery. Distance moved: Bas vs. Inh: paired t-test p=0.6631, t-0.4626. Time in the center: Bas vs. Inh: paired t-test p=0.6174, t=0.5322. n=6 per group.

e) Left: Schematic of a real-time place preference assay demonstrating optogenetic inhibition when the CFA-injected mouse is in the light-paired chamber and no optogenetic inhibition when the mouse spontaneously moves to the light-unpaired chamber. The experiment was conducted 3 days after the CFA injection. Right: Time spent by mice in an optogenetic inhibition-paired chamber. eNpHR 3.0 expressing mice are shown in red, and GFP expressing mice in green. GFP: CFA vs. Sham t-test p=0.9348, t=0.3349. eNpHR 3.0: CFA vs. Sham t-test p=0.0039, t=4.159. Interaction: RM 2-way ANOVA p=0.0222, F(1,10)=7.313. n=6 per group.

α7 nAChR activation relieves pain by inhibiting the activity of vlPAG$^{Chrna7+}$ neurons.

Given that inhibiting vlPAG$^{Chrna7+}$ neurons is antinociceptive, we tested the effects of optogenetic activation of endogenous cholinergic drive on these neurons. In a *ChAT-Cre*::*Chrna7-Cre* mouse line, we expressed ChrimsonR in PPTg^{ChAT+} neurons and GCaMP6 in vlPAG$^{Chrna7+}$ neurons and conducted simultaneous optogenetics and fiber photometry (Fig 13a). We observed that activating PPTg^{ChAT+} terminals in the vlPAG increased latency to paw flick and a correlated decrease in the fluorescence intensity, indicating inhibition of vlPAG$^{Chrna7+}$ neurons (Fig 13b, c). The maximal increase in latency to paw flick was observed during the lowest activity of vlPAG$^{Chrna7+}$ neurons (Fig 13c). Activation of cholinergic inputs to vlPAG did not immediately suppress vlPAG$^{Chrna7+}$ neuronal activity but generated a transient increase in neural activity, followed by inhibition that took ~15 mins to develop, suggesting potential cell signaling after α7 nAChR activation. Given that stimulating cholinergic inputs suppressed vlPAG$^{Chrna7+}$ neuronal activity and was antinociceptive, we tested the analgesic effects of the α7 nAChR partial agonist, EVP-6124[121]. In acute RHS assay, pretreatment with EVP-6124 (0.3 mg/kg, i.p.) increased paw withdrawal latency (Fig 13d). This analgesic effect peaked 25-45 min after EVP-6124 administration and persisted for several hours (data not shown). Using *in vivo* fiber photometry, we also verified that EVP-6124 induced transient activation followed by a persistent decrease in the activity of vlPAG$^{Chrna7+}$ neurons at analgesic doses (Fig 13e, f). To test the necessity of this decrease in activity for the antinociceptive effects of EVP-6124, we expressed ChrimsonR and GCaMP6 on vlPAG$^{Chrna7+}$ neurons to activate and monitor these neurons (Fig 13g). After EVP-6124 administration, optogenetic activation of vlPAG$^{Chrna7+}$ neurons blocked the analgesic effects of the agonist in a stimulation frequency-dependent manner (Fig 13h, i). These observations demonstrate that a decrease in the activity of vlPAG$^{Chrna7+}$ neurons is an essential substrate for the analgesic effects of α7 nAChR activation.

To explain α7 nAChR activation-induced decrease in activity, we explored potential cell signaling mechanisms. High Ca^{2+} permeability of α7 nAChRs[32] has been shown to recruit N-acyl phosphatidyl-ethanolamine-specific phospho-lipase D (NAPE-PLD)-dependent signaling[122–124] in other brain regions. Interestingly, NAPE-PLD levels are dynamically regulated by pain states as well, where generally, chronic pain conditions decrease NAPE-PLD levels[74,125,126]. We tested if α7 nAChR activation alters NAPE-PLD in the vlPAG by injecting mice with EVP-6124 (0.3mg/kg) or saline, followed by a formalin assay. We observed significant upregulation in both the number of neurons expressing NAPE-PLD and the mean expression level per neuron (Supp Fig 8a).

NAPE-PLD has been known to recruit endocannabinoid-like signaling molecules that target the nuclear receptor - peroxisome proliferator-activated receptor α (PPARα)[127–132]. We explored if PPARα signaling is an essential substrate for α7 nAChR activation-induced decrease in activity. To that end, we labeled vlPAG$^{Chrna7+}$ neurons with tdTomato fluorophore and used cell-attached recordings to allow monitoring of the firing rate without altering the intracellular milieu (Fig 13j). Under these conditions, EVP-6124 (2nM) perfusion reduced the spontaneous firing rate (Fig 13k, l), as observed *in vivo* (Fig 13e, f). Preincubation with a PPARα antagonist, GW 6471 (1μM), blocked EVP-6124 (2nM)-mediated decrease in firing rate without altering baseline activity (Fig 13k, l). These data support a PPARα mediated decrease in excitability following a7 nAChR activation. In a separate set of experiments, we tested if GW 6471 alters α7 nAChR activation through endogenous cholinergic inputs. We observed that optical stimulation of PPTg^{ChAT+} terminals induced post-synaptic α7 nAChR currents that were not altered by GW 6471 treatment (Supp Fig 8d). Interestingly, these endocannabinoid-like signaling regulators, including NAPE-PLD, FAAH, and PPARα, have also been implicated in altered algesia.

While PPARα provides a nexus for the delayed inhibitory effects of α7 nAChR activation, the signaling target that regulates membrane excitability was unknown. Recent reports have suggested that PPARα activators phosphorylate 5' adenosine monophosphate-activated protein kinase (AMPK), a key regulator of $K_v2.1$, where increased pAMPK decreases $pK_v2.1$[133]. Interestingly, both AMPK and $K_v2.1$ are implicated in nociception[134–140], opioid use[141–144], and regulating neuronal excitability[145–147]. These characteristics made them important targets for further exploration of signaling downstream of α7 nAChR activation. Using similar assays as above, we explored the phosphorylation of AMPK and various phosphorylation sites of $K_v2.1$ (S440, S537, S563, S603). Following EVP-6124 administration, we observed an increase in phosphorylated AMPK (Thr172) expression in vlPAG neurons (Supp Fig 8b), accompanied by a decrease in phosphorylated $K_v2.1$ at S603 (Supp Fig 8c). Decreased phosphorylation of $K_v2.1$(S603) increases K^+ conductance to reduce excitability[147]. Interestingly, levels of $pK_v2.1$ correlated strongly with the observed antinociceptive effects of EVP-6124 in the formalin assay (Supp Fig 8c). Other phosphorylation sites did not show appreciable differences (not shown). These observations highlight a novel relationship between α7 nAChRs and potassium channels mediated through Ca^{2+}-dependent signaling cascades.

Given these observations, we tested the effects of blocking PPARα on the analgesic effects of α7 nAChR agonist administration. Indeed, the analgesic effects of EVP-6124 (0.3mg/kg, s.c.) in Phase 2 of the formalin assay were reduced after pre-administration of GW

6471 (2 mg/kg, i.p., Fig 13m). These observations suggest that α7 nAChRs agonists relieve pain by inhibiting the activity of vlPAG$^{Chrna7+}$ neurons through a PPARα-dependent signaling mechanism (Supp Fig 8e)[132,148–150].

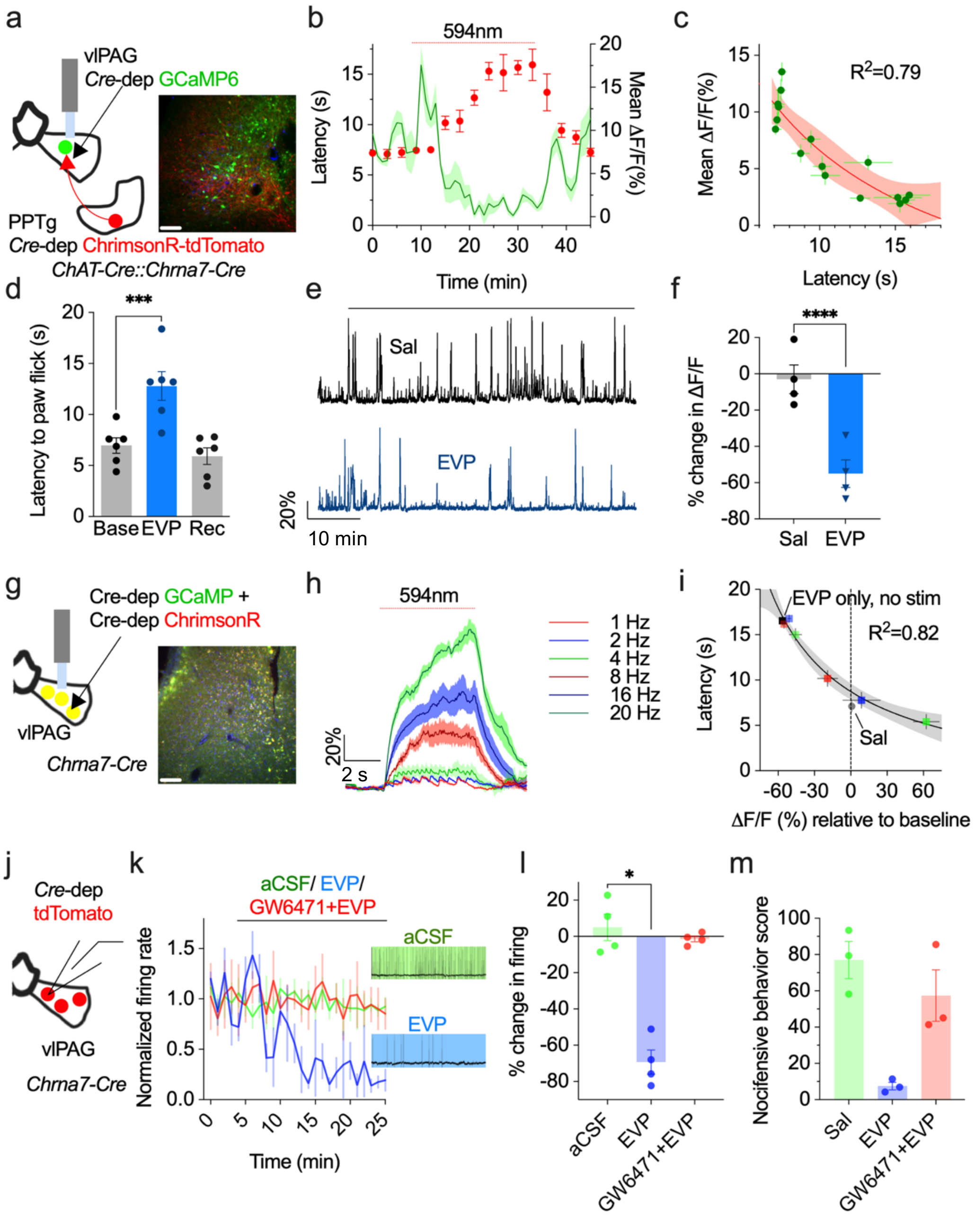

Figure 13: α7 nAChR activation is antinociceptive via inhibition of vlPAG$^{Chrna7+}$ neurons.

Figure 13 (continued): a) Latency to paw withdrawal in a RHS assay during Baseline, after systemic EVP-6124 (0.3mg/kg) administration, and Recovery. Baseline vs. EVP-6124: paired t-test p=0.0003, t=8.884. n=6.

b) Representative vlPAG$^{Chrna7+}$ GCaMP6 fluorescence measured using fiber photometry during open field behavior after saline (black) and EVP-6124 (blue) administration.

c) Percent change in mean fluorescence 25-30 min after saline (gray) or EVP-6124 (0.3mg/kg) administration compared to 0-5 mins before administration. Baseline vs. EVP-6124: paired t-test p<0.0001,t=127.4. n=4.

d) Left: schematic of simultaneous fiber photometry and optogenetics strategy. A double transgenic *ChAT-Cre::Chrna7-Cre* line is used to selectively activate PPTg^{ChAT+} terminals in vlPAG using ChrimsonR while monitoring vlPAG$^{Chrna7+}$ neuronal activity using GCaMP6 and fiber photometry. Right: Fluorescence image showing GCaMP6 expression on vlPAG$^{Chrna7+}$ neurons (green) and ChrimsonR-tdTomato expression on PPTg^{ChAT+} terminals (red) in the vlPAG (scale bar: 50μm).

e) Latency to paw withdrawal in RHS assay is plotted on the left y-axis (filled red circles). The RHS assay was conducted every 3 mins. The mean GCaMP6 fluorescence from vlPAG$^{Chrna7+}$ neurons during 1 min time bins is plotted on the right y-axis (green). Optogenetic activation of PPTg^{ChAT+} terminals using 594nm 20hz stimulation is denoted with a red dotted line. The data were fit to illustrate inverse correlation (red line), and shading illustrates the 95% confidence interval of the fit. n=4.

f) Mean GCaMP6 fluorescence from vlPAG$^{Chrna7+}$ neurons during the 3 min time bin is plotted against the corresponding latency to paw withdrawal in the RHS assay. Individual symbols represent 3 min time bins. n=4.

g) Left: schematic of simultaneous fiber photometry and optogenetics strategy. GCaMP6 and ChrimsonR were expressed on vlPAG$^{Chrna7+}$ neurons to monitor and manipulate their activity. Right: Fluorescence images showing GCaMP6 (green) and ChrimsonR-tdTomato (red) expression on vlPAG$^{Chrna7+}$ neurons (yellow denotes overlapping expression, scale bar: 50μm).

h) Optogenetic activation of vlPAG$^{Chrna7+}$ neurons at varying frequencies (1-20Hz) and the corresponding changes in GCaMP6 fluorescence from vlPAG$^{Chrna7+}$ neurons. Mean vlPAG$^{Chrna7+}$ GCaMP6 fluorescence traces collected using fiber photometry time locked to optogenetic activation (4 traces per animal, n=4 mice).

i) Latency to paw withdrawal in RHS assay is plotted against the change in GCaMP6 fluorescence of vlPAG$^{Chrna7+}$ neurons relative to baseline activity. Effects of saline administration are plotted as a solid gray circle. Subsequent effects of EVP-6124 (0.3mg/kg) administration only (without optogenetic stimulation) are plotted as a filled black square. Optogenetic activation of vlPAG$^{Chrna7+}$ neurons after EVP-6124 administration at different frequencies is denoted by different colors and symbols after EVP-6124 administration. n=4 mice.

j) Schematic of slice electrophysiology from fluorescently labeled vlPAG$^{Chrna7+}$ neurons using tdTomato.

k) On-cell recordings conducted from fluorescently labeled vlPAG$^{Chrna7+}$ neurons during different drug perfusions (EVP-6124: 2nM, GW6471: 1μM). Insets in green and blue background show representative traces during 20-25min after aCSF and EVP-6124, respectively. n=4 cells from 3 mice.

l) Percent change in firing rate relative to 0-5 mins time bin. Drug effects are plotted as the average firing rate during 15-20 mins after drug bath perfusion. aCSF vs. EVP: Kruskal-Walis test with Dunn's correction mean rank diff=-6.25, p=0.0427. n=4 cells from 3 mice.
m) Nocifensive behavior score (%) during Phase 2 of formalin assay after administration of Sal (black), EVP (blue), and EVP administered 10 min after GW6471 pre-infusion (red). n=3.

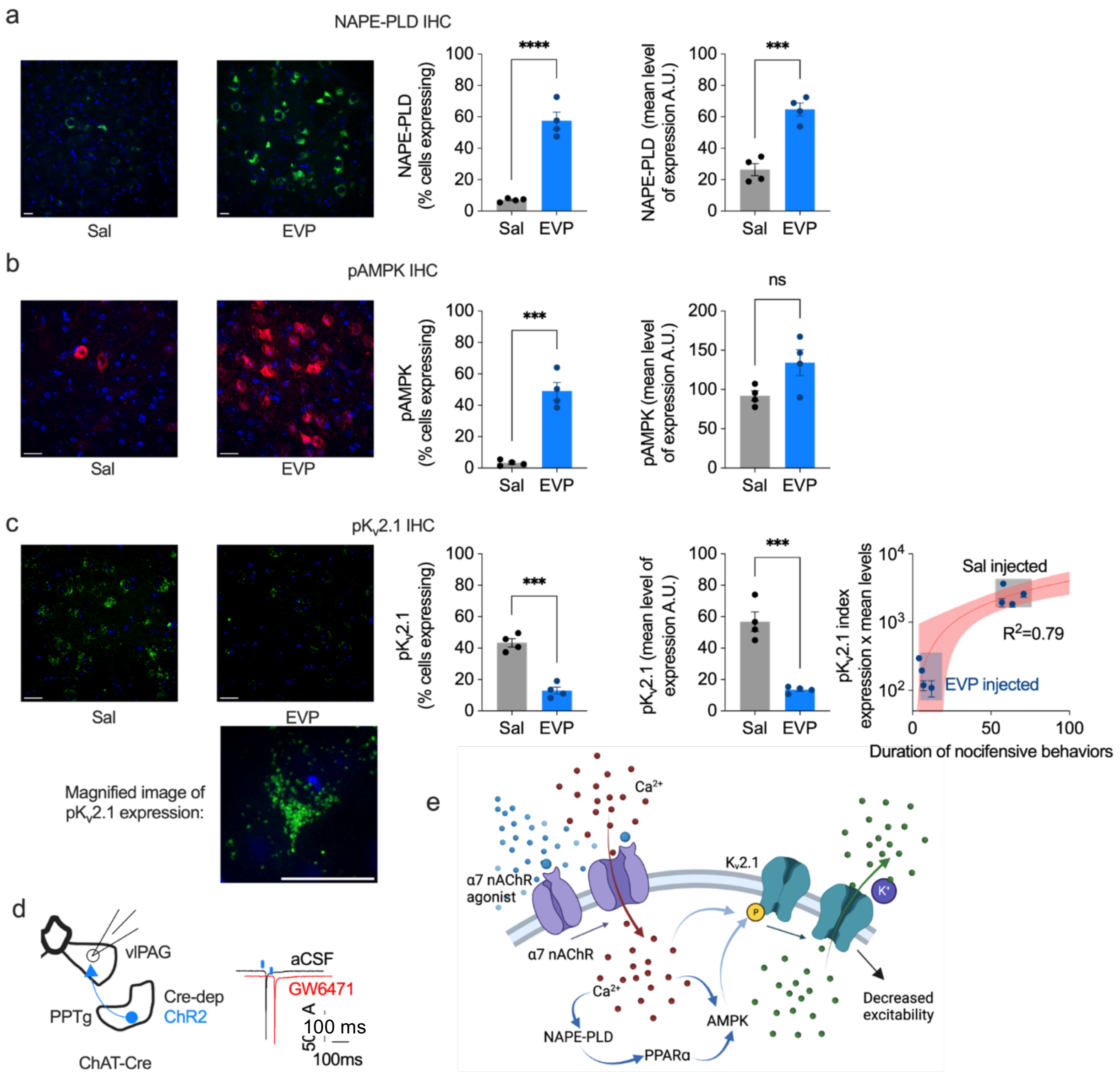

Supp Fig 8: α7 nAChR activation inhibits vlPAG$^{Chrna7+}$ neurons to produce antinociceptive effects.

a) Left: Representative fluorescence images showing NAPE-PLD expression in the vlPAG after saline or EVP-6124 (0.3mg/kg) administration (scale bar 10μm). Right: Mean percent of cells showing NAPE-PLD expression and mean level of expression per cell after saline and EVP-6124

Supp Fig 8 (continued): administration. % cells: Sal vs. EVP t-test p<0.0001, t=9.195. levels per cell: Sal vs. EVP t-test p=0.0002, t=8.049. n=4 per group.

b) Left: Representative fluorescence images showing phosphorylated AMPK expression in the vlPAG after saline or EVP-6124 (0.3mg/kg) administration (scale bar 10μm). Right: Mean percent of cells showing pAMPK expression and mean level of expression per cell after saline and EVP-6124 administration. % cells: Sal vs. EVP t-test p=0.0001, t=8.587. levels per cell: Sal vs. EVP t-test p=0.0005, t=6.821. n=4 per group.

c) Left: Representative fluorescence images showing phosphorylated $K_v2.1$ expression in the vlPAG after saline or EVP-6124 (0.3mg/kg) administration (scale bar 10μm). Right: Mean percent of cells showing $pK_v2.1$ expression and mean level of expression per cell after saline and EVP-6124 administration. The correlation curve between the pKv2.1 index and the duration of nocifensive behaviors in the formalin assay. % cells: Sal vs. EVP t-test p=0.0530, t=2.404. levels per cell: Sal vs. EVP t-test p=0.0004, t=6.941. n=4 per group.

d) Left: Slice electrophysiology schematic: ChR2-expressing $PPTg^{ChAT+}$ terminals were activated during voltage-clamp recordings (-70mV) from vlPAG neurons to monitor optogenetically evoked synaptic currents. Right: Representative traces demonstrating $PPTg^{ChAT+}$ terminal activation-evoked inward current is unaltered by bath application of PPARα antagonist GW 6471 (100nM).

e) Schematic depicting the proposed intracellular signaling mediating the observed decrease in neuronal excitability post α7 nAChR activation.

α7 nAChRs are expressed on vlPAG^{GABA+} interneurons, and their inhibition relieves pain via disinhibition of descending pain control pathways.

To explore how α7 nAChRs alter the descending pain circuits, we further investigated the role of vlPAG$^{Chrna7+}$ neurons in the context of the descending projections from the vlPAG. First, we explored the mRNA expression profile of vlPAG$^{Chrna7+}$ neurons using FISH. We identified that a majority of vlPAG$^{Chrna7+}$ neurons expressed the vesicular GABA transporter (vGAT; *Slc32a1*$^{+}$), a marker of GABAergic neurons (Supp Fig 9a, b). These vlPAG$^{Chrna7+}$ neurons co-expressed markers for other neuromodulators and receptors, including cannabinoid receptor 1 (*Cnr1*), prodynorphin (*Pdyn*), and μ-opioid receptors (*Oprm1*, explored later, Supp Fig 9a, b, c). Using optogenetics and slice electrophysiology, we tested whether vlPAG$^{Chrna7+}$ neurons function as local interneurons. To that end, we expressed ChR2 in vlPAG$^{Chrna7+}$ neurons and recorded from non-fluorescent neighboring vlPAG neurons (Fig 14a). Consistent with our FISH results, optogenetic stimulation of vlPAG$^{Chrna7+}$ neurons evoked outward currents in the neighboring recorded cells, and these currents were blocked by pretreatment with the GABA-A receptor antagonist, bicuculline (Fig 14b). We then tested how activating vlPAG$^{Chrna7+}$ neurons alters the activity of vlPAG→RVM projections *in vivo*, using simultaneous optogenetics and fiber photometry. Here, we injected a retrogradely transported virus in the RVM to express jGCaMP7s in projection neurons from vlPAG and another virus into the vlPAG to express ChrimsonR in vlPAG$^{Chrna7+}$ neurons (Fig 14c). We observed that activating vlPAG$^{Chrna7+}$ neurons decreased mean fluorescence, suggesting inhibition of the activity of vlPAG→RVM projections (Fig 14d). These observations support the conclusion that vlPAG$^{Chrna7+}$ neurons are local inhibitory interneurons that regulate the output of vlPAG projections to the RVM.

Based on these observations, we tested if α7 nAChR activation relieves pain by disinhibiting descending vlPAG projections to RVM. We used slice electrophysiology to test this hypothesis directly by fluorescently backlabeling RVM projecting vlPAG neurons using a retrogradely transported virus (Fig 14e). In preliminary investigations, we identified that very few (~11%) vlPAG$^{Chrna7+}$ neurons project to the RVM, consistent with their dominant local inhibitory phenotype. We observed that bath application of EVP-6124 (2nM) decreased the frequency of spontaneous inhibitory postsynaptic currents (sIPSCs) recorded from backlabeled vlPAG→RVM projection neurons over 20-25 mins (Fig 14f). Together, these findings demonstrate that α7 nAChR activation inhibits vlPAG$^{Chrna7+}$ neurons to disinhibit the descending pain pathways and relieve pain, similar to the physiological effects of opioids[46].

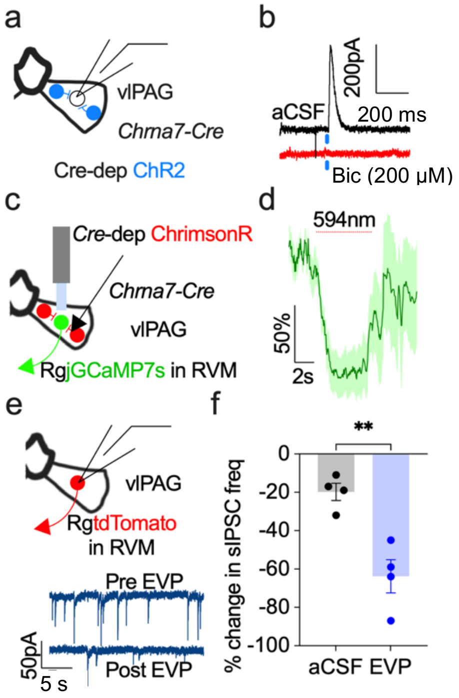

Figure 14: vlPAG$^{Chrna7+}$ neurons inhibit vlPAG→RVM neurons.

a) Slice electrophysiology schematic. ChR2-mCherry was virally expressed in vlPAG$^{Chrna7+}$ neurons, and whole-cell voltage clamp recordings were conducted from unlabeled (putative

Figure 14 (continued): projection) neurons while optically activating neighboring vlPAG$^{Chrna7+}$ neurons (0mV, E_{Cl-} ~-70mV).
b) Optically evoked inhibitory postsynaptic outward current blocked by bath application of bicuculline (20µM). Data are represented with a vertical offset.
c) Schematic depicting strategy to activate vlPAG$^{Chrna7+}$ neurons while monitoring vlPAG→RVM projection neurons using GCaMP6 and simultaneous optogenetics and fiber photometry. *Cre*-dependent ChrimsonR was expressed in vlPAG$^{Chrna7+}$ neurons and retrogradely transported AAV expressing GCaMP6 injected in the RVM.
d) Mean GCaMP6 fluorescence from vlPAG→RVM projection neurons (green trace) collected using fiber photometry time locked to optogenetic activation of vlPAG$^{Chrna7+}$ neurons (red line, 4 traces per animal, n=3).
e) Top: Schematic depicting retrograde tdTomato labeling of vlPAG→RVM projection neurons for slice electrophysiology. Bottom: Spontaneous IPSCs before (above) and after (below) EVP-6124 bath application. Neurons were voltage clamped at -70mV with E_{Cl-} ~0mV and CNQX (20µM) in the bath.
f) Percent change in the frequency of spontaneous IPSCs 2-5 mins before aCSF/EVP-6124 (2nM) application and 15-20 mins after aCSF(gray)/EVP(blue) bath application. Unpaired t-test p-value= 0.0041. n=4 cells from 3 mice.

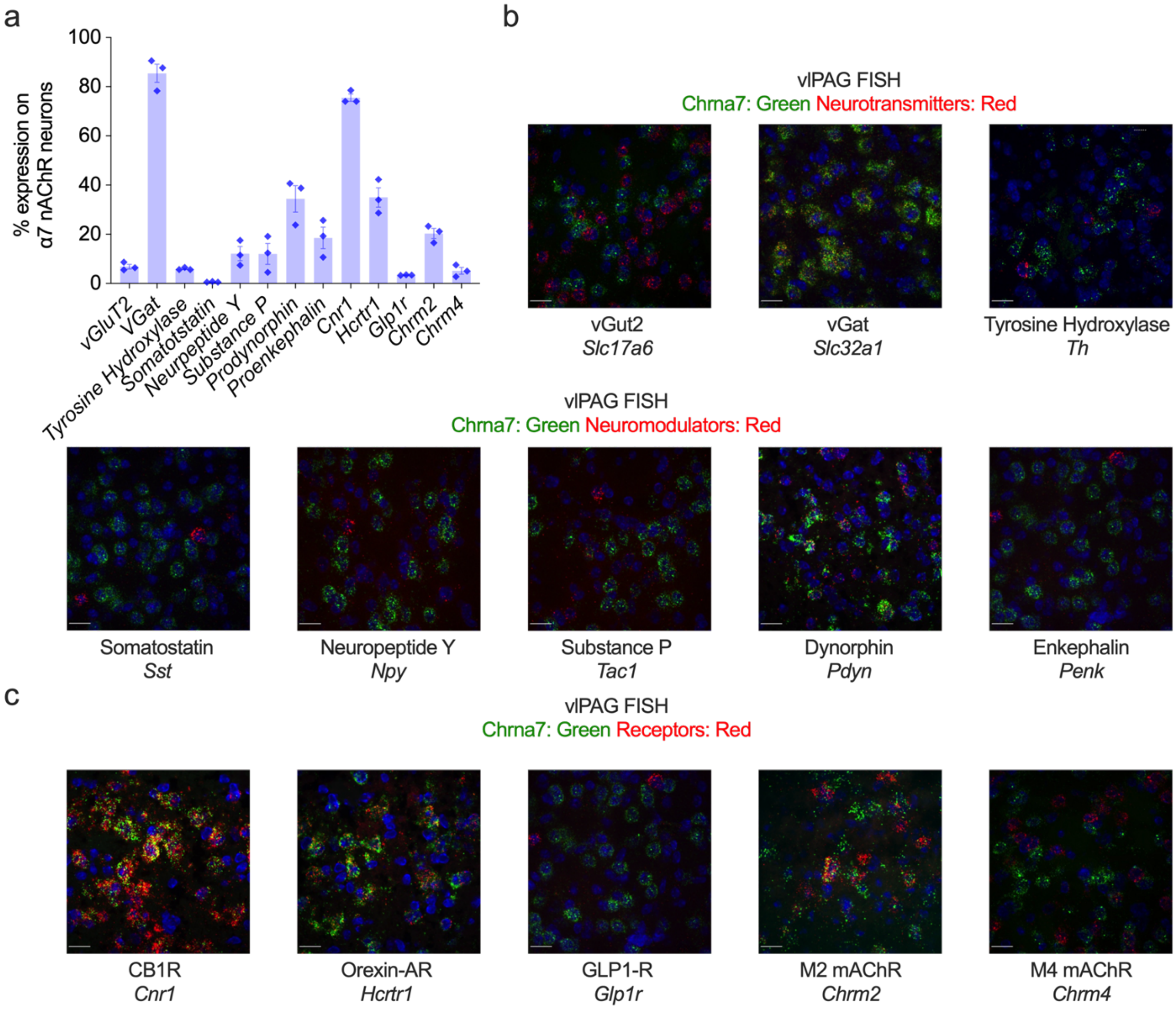

Supp Fig 9: α7 nAChRs are expressed on GABAergic vlPAG neurons.

a) Percent co-expression of α7 nAChR mRNA on vlPAG neurons expressing common neurotransmitters, modulators, and receptors explored using fluorescence *in situ* hybridization (FISH). Six representative vlPAG images were taken per mouse. From each image, the percent of cells positive for both α7 nAChR and the other mRNA were calculated and then averaged across all 6 images. n=3.
b) Representative images showing co-expression of α7 nAChR mRNA (green) with neurotransmitters (top, red) and neuromodulators (bottom, red) with nuclear DAPI stain (blue, scale bar 20μm).
c) Representative images showing co-expression of α7 nAChR mRNA (green) with receptors (red) with nuclear DAPI stain (blue, scale bar 20μm).

α7 nAChR agonist inhibits pain- and opioid-sensitive neurons in the vlPAG without reward and tolerance profiles.

α7 nAChRs show strong functional overlap with μ-opioid receptor-expressing vlPAG neurons.

Given the observed similarities in the observed physiological and behavioral effects of α7 nAChR and μ-opioid receptor agonist, we explored overlap in receptor expression in the vlPAG. Using FISH and protein assays, we found co-expression in 71-74% of the neurons that expressed at least one of these receptor types (Supp Fig 10a, b, c, d).

The significant overlap in receptor expression motivated us to test whether the opioid-sensitive pain-encoding vlPAG neuronal ensemble could be effectively targeted by the α7 nAChRs agonist (EVP-6124) to relieve pain. Additionally, it has been challenging to track the changes in the activity of individual neurons in descending pain control pathways across different pain states. To address these questions, we used an *in vivo* 2-photon imaging approach to monitor neuronal ensemble dynamics over multiple days in the progression to a chronic pain state and through the development of opioid tolerance. Pan-neuronal GCaMP6 was expressed in the vlPAG, and neurons were imaged through a GRIN lens in awake-behaving mice in a head-fixed apparatus (n=5 mice, Fig 15a). After habituation, mice were tested over four weeks, and the neurons that were consistently tracked across those days were analyzed for spontaneous and pain-evoked activity (Fig 15 b, c). A majority of the monitored vlPAG neurons were activated by noxious stimuli that elicited nocifensive behaviors (Fig 15f, Supp Fig 10e, f). Furthermore, opioids efficiently decreased both the spontaneous and the pain-evoked activity of these vlPAG neurons (Fig 15d, e, f, g). Establishing a chronic neuropathic pain state using paclitaxel (8mg/kg, four injections over eight days) induced thermal hyperalgesia (Supp Fig 10g) and hyperexcitability in these vlPAG neurons (Fig 15d, e, f, g). Interestingly, the chronic pain state also recruited neurons that were previously non-responsive to noxious stimuli into the pain-responsive ensemble (Supp Fig 15e, f). In this chronic pain state, morphine (10mg/kg) administration still inhibited the pain-responsive ensemble, including those newly recruited pain-responsive cells (Fig 15d, e, f, g, h). However, induction of opioid tolerance resulted in weaker opioid-mediated suppression of activity (Fig 15d, e, f, g). In agreement with our previous optogenetic testing in opioid-tolerant mice, subsequent exposure to EVP-6124 (0.3mg/kg s.c.) effectively inhibited the pain-responsive ensemble (Fig 15d, e, f, g, h) and increased latency to paw withdrawal (Supp Fig 10g). Interestingly, the majority of neurons inhibited by morphine before inducing opioid tolerance were also inhibited by EVP-6124 (Fig 15h). These observations unambiguously demonstrate that chronic pain conditions expand the vlPAG neuronal ensemble that responds to painful experiences. α7 nAChRs and opioid receptors inhibit similar ensembles of neurons, and α7 nAChR activation still inhibits these neurons after the induction of opioid tolerance.

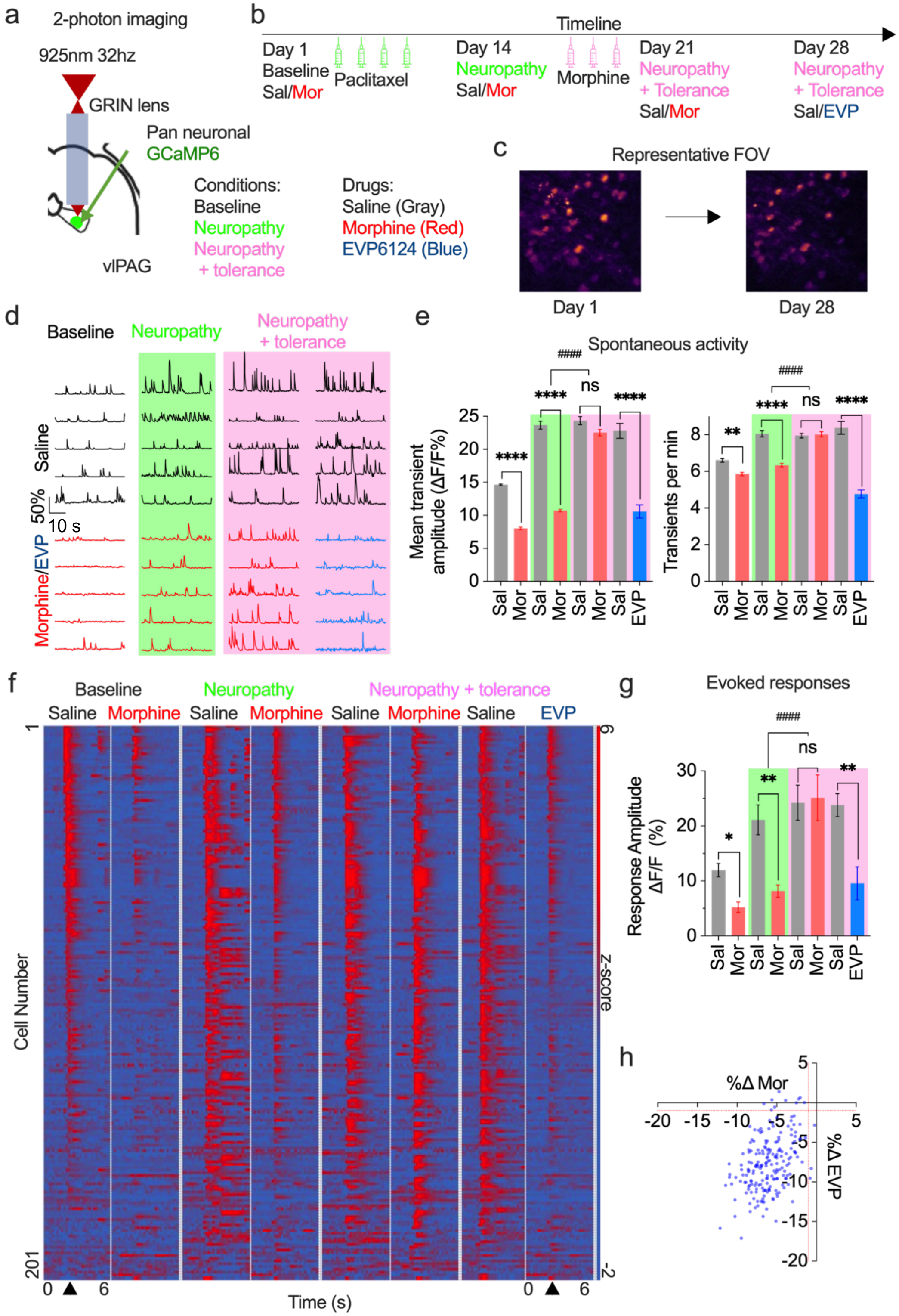

Figure 15: α7 nAChR agonist inhibits pain-responsive and opioid-sensitive ensembles.

Figure 15 (continued): a) Schematic showing 2-photon imaging strategy. GCaMP6 was expressed in vlPAG neurons, and a GRIN lens was implanted above to monitor neuronal activity in head-fixed awake-behaving animals.
b) Timeline of the experimental assays: mice were tested for spontaneous activity, and noxious stimuli evoked neuronal responses after saline and morphine administration on Days 1, 14, and 21. On Day 28, similar tests were conducted after saline or EVP-6124 administration. From Days 2-7, mice were subjected to paclitaxel-induced neuropathy. From Days 14-21, mice were subjected to opioid tolerance.
c) Standard deviation fluorescence image showing a representative field of view of tracked neurons from Day 1 to Day 28.
d) Activity traces from 5 representative neurons tracked through the course of behavioral assays (baseline, chronic pain, and opioid tolerance) and after various drug administrations: saline (black), morphine (red, 10mg/kg), and EVP-6124 (blue, 0.3mg/kg).
e) Quantification of spontaneous activity across all neurons and animals (n=201 neurons from 5 mice). Left: mean amplitude of transients and Right: mean transient frequency under baseline (1) and various pathological states, including chronic pain (2) and opioid tolerance (3). Metrics post morphine and EVP-6124 administration are represented in red and blue, respectively. Amplitude: 1. Sal vs. 1. Mor: paired t-test p-value<0.0001, t=7.325. 2. Sal vs. 2. Mor: paired t-test p-value<0.0001, t= 14.31. 3. Sal vs. 3. Mor: paired t-test p-value=0.2821, t= 1.995. 4. Sal vs. 4 EVP: paired t-test p-value<0.0001, t= 13.47. Interaction: p-value<0.0001, F(3,800) = 114.9. Frequency: 1. Sal vs. 1. Mor: paired t-test p-value= 0.0021, t=3.286. 2. Sal vs. 2. Mor: paired t-test p-value<0.0001, t= 7.466. 3. Sal vs. 3. Mor: paired t-test p-value= 0.7617, t=0.3033. 4. Sal vs. 4 EVP: paired t-test p-value<0.0001, t=15.83 (Holm Sidak adjustment for all comparisons). Interaction: p-value<0.0001, F(3,800) = 65.00.
f) Raster plots with each row representing separate vlPAG neurons with color-coded z-scored fluorescence. Warmer colors represent stronger activation under different treatment conditions. Tail withdrawal response to acute thermal noxious stimuli is indicated by an arrow—n=201 neurons from 5 mice.
g) Summary data quantifying the evoked fluorescence response amplitude after various drug treatments, including saline (gray), morphine (red), and EVP-6124 (blue) during baseline conditions, after chronic pain and opioid tolerance. 1. Sal vs. 1. Mor: paired t-test p-value=0.0248, t=1.870. 2. Sal vs. 2. Mor: paired t-test p-value= 0.0013, t= 3.595. 3. Sal vs. 3. Mor: paired t-test p-value= 0.9985, t=0.02473. 4. Sal vs. 4. EVP: paired t-test p-value= 0.0003, t=3.945. (Holm Sidak adjustment for all comparisons). Interaction: p-value<0.0001, F(3,800) = 10.32. n=201 neurons from 5 mice.
h) % change in evoked response amplitude of vlPAG neurons in chronic pain state after morphine (x-axis) and EVP-6124 (y-axis) administration as compared to baseline.

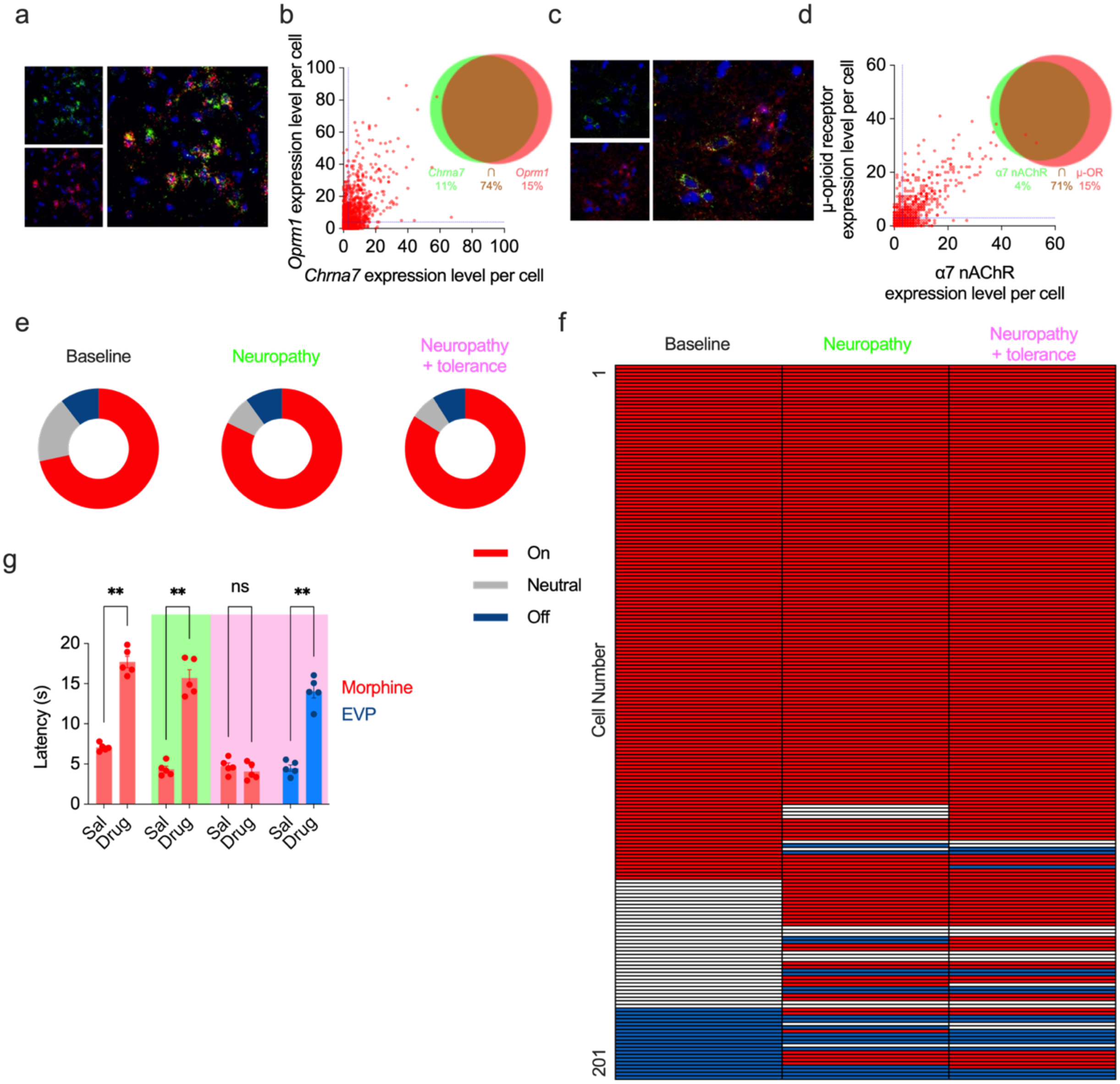

Supp Fig 10: α7 nAChR agonist inhibits opioid-responsive and pain-encoding ensembles to relieve pain.

a) Representative fluorescence *in situ* hybridization images showing co-expression of *Chrna7* (green) and *Oprm1* (red) mRNA with nuclear DAPI stain (blue).
b) Expression levels per cell for *Oprm1* mRNA plotted against *Chrna7* expression levels. Inset shows a Venn diagram demonstrating 74% overlap in mRNA expression on cells. n=1481 cells from 3 animals.
c) Representative fluorescence image with antibody staining for μ-opioid receptors (red) and fluorescently conjugated α-bungarotoxin stain for α7 nAChRs (green) with nuclear DAPI stain (blue).
d) Expression levels per cell for μ-opioid receptors and α7 nAChRs. Inset shows a Venn diagram demonstrating 71% overlap in protein expression on cells. n=1481 cells from 3 animals.

Supp Fig 10 (continued): e) Pie charts demonstrating the progression of neuronal responses to noxious stimuli across baseline, neuropathic pain, and tolerance. Neurons with a statistically significant increase in activity (bootstrap method) in response to a noxious stimuli are termed 'On' cells (red). Neurons with a statistically significant decrease in activity are termed 'Off' cells (blue). The remaining neurons are termed 'Neutral' (gray).
f) Progression of individual cellular identity across different phases of testing. Similar labeling is used as panel Supp Fig 10e.
g) Latency to paw withdrawal for the mice undergoing *in vivo* imaging experiments after drug injections (morphine: red, EVP-6124: blue) and across different pathological states of neuropathy and opioid tolerance. Green represents neuropathy and pink represents neuropathy with opioid tolerance.
Baseline: Sal vs. Drug paired t-test p=0.0013, t=11.50. Neuropathy: Sal vs. Drug paired t-test p=0.0010, t=12.30. Tolerance: Sal vs. Drug paired t-test, p=0.4230, t=1.912. EVP: Sal vs. Drug paired t-test p=0.0032, t=9.100. n=5.

α7 nAChR agonists relieve pain without the development of tolerance, rewarding effects, or withdrawal symptoms.

In addition to the analgesic effects of EVP-6124, we tested for the development of tolerance, reward profile, and affective withdrawal symptoms following repeated exposure to the drug. To test for analgesic tolerance, we repeatedly administered EVP-6124 (6 days, 2x/day, 0.3 mg/kg, n=8 per group), similar to the opioid tolerance paradigm. When we tested for antinociceptive effects using a RHS assay, we observed that even after repeated administration, EVP-6124 increased the latency to paw flick (Fig 16a). These observations suggest that repeated α7 nAChR activation does not produce tolerance to the analgesic effects. Opioid exposure using a similar paradigm induces opioid tolerance.

Next, we explored the reward profile associated with EVP-6124 using a conditioned place preference assay (Fig 16b). Here we observed that, unlike morphine, exposure to an analgesic dose of EVP-6124 (0.3 mg/kg, n=10 per group) in a particular context did not cause a preference for that context (Fig 16c)[151]. Finally, to test for affective withdrawal symptoms, we repeatedly exposed mice to EVP-6124 or morphine over five days and then conducted a conditioned place aversion assay where we precipitated withdrawal using the respective antagonists, MLA (α7 nAChR antagonist, 3 mg/kg) or naloxone (μ-opioid receptor antagonist, 6 mg/kg, n=8 per group, Fig 16d). We observed that while the naloxone-paired chamber was avoided by animals pre-exposed to morphine, EVP-6124-treated mice did not show an aversion to the MLA-paired chamber (Fig 16e). These observations suggest limited affective withdrawal symptoms associated with repeated EVP-6124 use. These results are consistent with previous demonstrations that α7 nAChRs do not elicit significant rewarding effects in rodents or humans.

In addition to acute and chronic neuropathic pain, we tested if α7 nAChR agonist treatment relieved tonic inflammatory pain. We observed that EVP-6124 (0.3 mg/kg) decreased the duration of nocifensive behaviors in Phase 2 of the formalin assay to similar levels as that of morphine (n=5 per group, Supp Fig 11a, b). Furthermore, a different α7 nAChR agonist (PHA-543613, 10 mg/kg, n=4 per gorup) and a positive allosteric modulator (PNU-120596, 10mg/kg) yielded antinociceptive effects similar to EVP-6124, in agreement with previous studies (Supp Fig 11b)[89,152]. As the positive allosteric modulator requires endogenous acetylcholine to achieve receptor activation and behavioral analgesic effects, these data complement our earlier results demonstrating changes in basal cholinergic tone during the formalin assay (Fig 6).

Drug combinations are commonly used clinically to limit opioid use. To test if α7 nAChR agonists could augment the analgesic effects of submaximal doses of morphine, we first established the behavioral effects of lower doses of morphine (4 mg/kg, i.p.) and EVP-6124 (0.1 mg/kg, s.c., n=4 per group). Co-administration of these doses decreased the duration of nocifensive behaviors in Phase 2 of the formalin assay relative to the effects of either drug alone (Supp Fig 11c). Under these conditions, the reduction in nocifensive behaviors had a magnitude similar to that of a maximal analgesic dose of morphine (10 mg/kg, i.p, Supp Fig 11b), in agreement with previous studies. Interestingly, with the combination of submaximal morphine and EVP-6124, we observed less dissociative locomotor behavior that may be induced by an analgesic dose of morphine (data not shown)[153–155]. We next tested if EVP-6124 (0.3 mg/kg) could decrease formalin-induced nocifensive behaviors in opioid-tolerant mice or after treatment with naloxone (6mg/kg, Supp Fig 11d). We observed that EVP-6124 reduced the duration of nocifensive behaviors in the formalin assay in opioid-tolerant mice and even after the administration of naloxone (Supp Fig 11d).

Additionally, EVP-6124 also relieved the affective component of tonic inflammatory pain, as tested using a conditioned place preference assay (CPP; Supp Fig 11e). Here, in the experimental group of animals, formalin injections in the hind paw were paired to both chambers of the CPP behavioral apparatus. However, in one chamber, the mice received EVP-6124 (0.3mg/kg) before formalin, and in the other chamber, saline (Supp Fig 11e, n=10 per group). Post-conditioning testing revealed that mice preferred the EVP-6124 paired chamber, suggesting a decrease in the affective component of pain (Supp Fig 11e). Together, these observations indicate that α7 nAChR agonists relieve pain and, along with the endogenous cholinergic circuit, form a viable avenue for pain treatment.

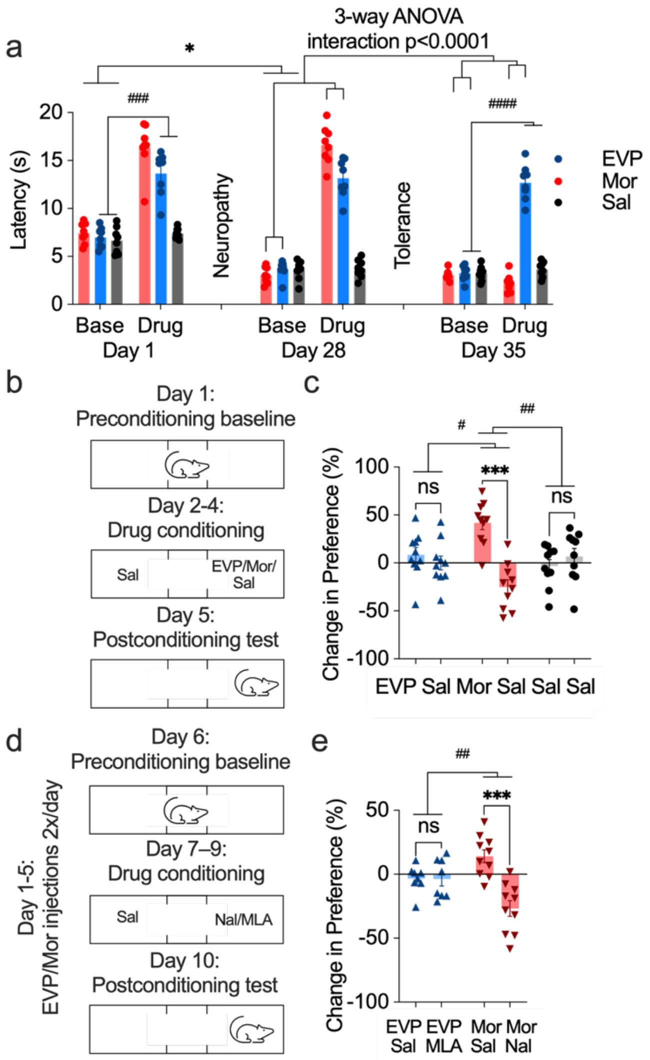

Figure 16: α7 nAChR agonist relieves pain without tolerance, reward, or withdrawal phenotype.

a) Latency to paw withdrawal in RHS assay is plotted before (Base) and after drug administration (Drug) of morphine (red, 10mg/kg), EVP-6124 (blue, 0.3mg/kg), or saline (gray). Tests were conducted before (Day 1) and after the chronic neuropathic pain state (Day 28) and after the induction of opioid tolerance. The baseline, neuropathic pain, and tolerance assays were conducted on Days 1, 28, and 35, respectively. n=8 per group.
b) Schematic showing conditioned place preference paradigm for reward phenotype. On Day 1, preconditioning baseline preference was tested. On Days 2-4, mice were conditioned to EVP-6124 (blue), morphine (red), or saline (gray) in the drug-paired chamber, and saline was administered in the other chamber. On Day 5, post-conditioning preference for the drug- and the saline-paired chamber was evaluated.
c) Percent change in preference on the post-conditioning day as compared to the preconditioning baseline for the drug-paired or the saline-paired chambers. The saline control group is in gray,

Figure 16 (continued): the morphine group in red, and the EVP-6124 group in blue. EVP vs. Sal: paired t-test p-value=0.9036, t=0.6184. Mor vs. Sal: paired t-test p-value=0.0002, t=4.809. Sal vs. Sal: paired t-test p-value=0.8554, t=0.7242. Interaction: p-value=0.0015, F(2,27) = 8.329. n=10 per group.

d) Schematic showing conditioned place preference paradigm for withdrawal phenotype. On Days 1-5, EVP-6124 (0.3mg/kg) or morphine (10mg/kg) was administered 2x/day. On Day 6, preconditioning baseline preference was established. On Days 7-8, mice were conditioned to MLA (blue) or naloxone (red) in the drug-paired chamber, and saline was administered in the other chamber. Mice received EVP-6124 and morphine in both chambers. On Day 10, post-conditioning preference for the drug- and the saline-paired chamber was evaluated.

e) Percent change in preference on the post-conditioning day as compared to the preconditioning baseline for the drug-paired or the saline-paired chambers. EVP-6124 and MLA group is in blue, and the morphine and naloxone group is in red. EVP-Sal vs. EVP-MLA: paired t-test p-value=0.9996, t=0.02467. Mor-Sal vs. Mor-Nal: paired t-test p-value=0.0004, t=4.744. Interaction: p=value=0.0063, F(1,16)=9.887. n=8 in the EVP-MLA group, and 10 in the Mor-Nal group.

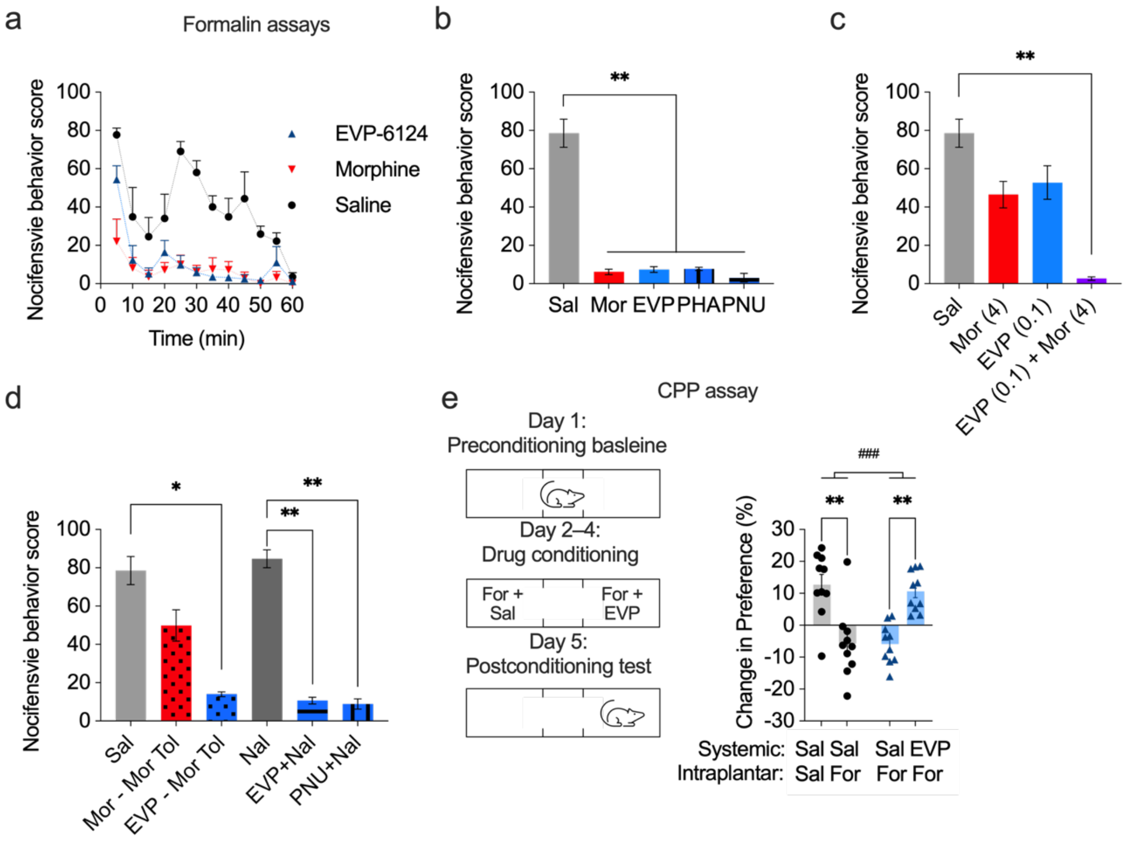

Supp Fig 11: α7 nAChR agonists and positive allosteric modulators relieve the somatic and affective components of inflammatory pain.

Supp Fig 11 (continued): a) Nocifensive behavior score (% time spent in 5 min time bin licking or lifting paw) during formalin assay after EVP-6124 (blue, 0.3mg/kg), morphine (red, 10mg/kg), and saline injections. n=5 per group.
b) Mean nocifensive behavior score during the tonic inflammatory phase (Phase 2) of the formalin assay after saline (gray), morphine (red, 10mg/kg), EVP-6124 (blue, 0.3mg/kg), PHA (blue with vertical stripes, 10mg/kg), PNU (blue horizontal stripes, 10mg/kg) administration. Sal vs. Mor: t-test p=0.0069, t=9.620. Sal vs. EVP: t-test p=0.0073, t=9.441. Sal vs. PHA: t-test p=0.0071, t=9.534/ Sal vs. PNU: t-test p=0.0020, t=9.754. n=4 per group. The common saline group was used in subsequent figures and analysis.
c) Mean nocifensive behavior score during the tonic inflammatory phase (Phase 2) of the formalin assay after low-dose morphine (red, 4mg/kg), low-dose EVP-6124 (blue, 0.1mg/kg), and the combination dose (purple). Sal vs. EVP (0.1): t-test p=0.1657, t=2.254. Sal vs. Mor (4): t-test p=0.0518, t=3.164. Sal vs EVP (0.1) + Mor (4): t-test p=0.0048, t=10.19. n=4 per group.
d) Mean nocifensive behavior score during the tonic inflammatory phase (Phase 2) of the formalin assay after morphine administration in morphine-tolerant mice (red with dots), EVP-6124 administration in morphine-tolerant mice (blue with dots), mice injected with naloxone (6mg/kg grey with horizontal stripes), EVP-6124 administration after naloxone (blue with horizontal stripes) and PNU-120596 after naloxone (blue with vertical stripes). Sal vs. Mor-Mor Tol: p=0.1568, t=2.596. Sal vs. EVP-Mor Tol: p=0.0110, t=8.636. Nal vs. EVP+Nal: p=0.0099, t=8.946. Nal vs. PNU+Nal: p=0.0034, t=8.854. n=4 per group.
e) Left: Schematic showing conditioned place preference paradigm for affective pain testing. On Day 1, preconditioning baseline preference was established. On Days 2-4, test mice (blue) were conditioned to intraplantar formalin injections in both chambers, but in one chamber, they received systemic EVP-6124 (0.3mg/kg), and in saline in the other. The control mice (gray) received intraplantar formalin in one chamber and intraplantar saline in the other but received systemic saline in both chambers. On Day 5, post-conditioning preference for the drug- and the saline-paired chamber was evaluated. Right: Percent change in preference on the post-conditioning day as compared to the preconditioning baseline for the EVP-6124 and saline-paired chambers. The test group is blue, and the control group is gray. Formalin intraplantar (blue): EVP (s.c.) vs. Sal (s.c.): paired t-test p=0.0089, t=3.251. Sal (s.c., gray): Formalin intraplantar vs. saline intraplantar: paired t-test p=0.0035, t=3.664. n=10 per group.

Discussion

Chronic pain states are encoded in multiple brain regions at cellular and network levels through synaptic and intrinsic excitability mechanisms[156–160]. Within these networks, the vlPAG serves as a critical nexus that modulates painful experiences by integrating and processing information from functionally diverse brain regions, including the medial prefrontal cortex, orbitofrontal cortex, amygdala, and parabrachial nucleus[73,161–166]. Electrical, pharmacological, and chemogenetic manipulation of vlPAG neurons has analgesic effects[48–69], predominantly through outputs to key nuclei, including the rostral ventromedial medulla and the locus coeruleus[74,167]. While vlPAG neurons respond to acute noxious stimuli that elicit nocifensive behaviors, how chronic pain and opioid exposure alters the physiology of pain-encoding ensembles in the vlPAG has not been explored[45]. Furthermore, the role of neuromodulation in the PAG, including the role of cholinergic inputs in acute and chronic pain, remains understudied. In this study, we demonstrate the bidirectional relationship between pain and the endogenous cholinergic dynamics in vlPAG. Next, we identify the AChRs and their signaling pathway that reverses the pain-induced maladaptive plasticity and hyperexcitability in neuronal ensembles of the vlPAG. We also show that the analgesic potency of descending pain control circuits, particularly cholinergic analgesia, is preserved after opioid tolerance. We identify that ACh strongly modulates vlPAG excitability to alter sensory and affective pain experiences. This cholinergic modulation originates from synaptic inputs and ultimately alters the intrinsic excitability of pain-encoding neuronal ensembles. These observations deepen our understanding of pain circuits and point toward molecular and cellular targets for identifying non-opioid pain treatment strategies.

While opioids are potent analgesics, their repeated use leads to analgesic tolerance and opioid-induced hyperalgesia through molecular, synaptic, and network-level adaptations[168–172]. These adaptations include activation of G protein βγ-subunit signaling pathways or biased signaling mechanisms that recruit β-arrestin[110,173,174]. Changes in the recruitment of GIRK channels in the vlPAG and other brain regions have also been suggested as potential underlying mechanisms of opioid tolerance[175–177]. In the vlPAG, opioids inhibit vlPAG$^{Oprm1+/GABA+}$ interneurons to remove the tonic inhibition on vlPAG output projection neurons and relieve pain. Opioid tolerance could result from decreased efficacy of opioids to inhibit these interneurons[46]. Our investigations demonstrate that even after the maladaptive molecular changes associated with opioid tolerance, direct somatic inhibition of vlPAG^{Oprm1+} neurons relieves pain, suggesting that the analgesic potency of these descending pain control circuits is preserved and can be recruited to relieve pain. Additionally, recruiting endogenous cholinergic signaling can alleviate pain while co-administering opioid agonists at submaximal doses or even opioid antagonists, supporting the independent nature of their analgesic mechanisms. Parallel investigations could explore the effects of other endogenous neurotransmitters in the context of opioid dependence and withdrawal to decrease relapse.

In contrast to opioids, the role of neuromodulators like ACh in the pathophysiological development of chronic pain has been underexplored. Our anatomical, physiological, and optogenetic assays identified that endogenous cholinergic circuits and AChRs potently modulate the pain-encoding vlPAG ensembles and nocifensive behaviors. These investigations identified unexpected observations regarding cholinergic physiology: First, we observed an unexpected pain-induced decrease in ACh levels in the vlPAG. Canonically, salient stimuli *increase* ACh release in brain regions like the cortex, hippocampus, and amygdala[8,178]. Increased ACh release in these brain regions facilitates salient cue detection, enhances the signal to noise, and serves as a learning signal. In the ventral tegmental area, cholinergic drive from the LDTg primes dopaminergic neurons for burst firing. However, few studies have identified a role for a decrease in ACh levels[179], suggesting an unexplored, but important, role of the baseline cholinergic tone. Our data unambiguously demonstrate that decreases in basal cholinergic tone are correlated with nocifensive behaviors in acute and chronic pain states. These observations suggest that baseline cholinergic tone helps set an equilibrium level of algesia. Interestingly, the cholinergic tone in other brain regions is associated with attention and other cognitive functions[8,10–13], and intriguingly, chronic pain conditions like diabetic neuropathies are associated with comorbidities like ADHD[180]. Exploring relationships between cognitive comorbidities and changes in cholinergic tone in chronic pain could present additional avenues for exploration. Furthermore, what the basal cholinergic tone in the vlPAG encodes will be an important area of future research.

Second, the role of cholinergic signaling in evolutionarily conserved behaviors has been challenging to identify. These difficulties stem partially from the enigmatic and debated nature of cholinergic synaptic transmission – both bulk volume transmission through diffuse axonal arborizations and fast synaptic transmission have been proposed[8,15,113,114]. These difficulties also stem from the exquisite activation and desensitization kinetics of AChRs, the rapid hydrolysis of ACh, its electrochemically neutral nature, and its dominant effects on presynaptic terminals as opposed to somatodendritic sites[13]. Additionally, multiple cholinergic projections co-release other neurotransmitters[13,181,182], further complicating efforts to identify the effects of ACh.

Methodological innovations employed in this study have aided our explorations. Using cell-type and projection-specific optogenetic approaches and slice electrophysiology, we demonstrate clear evidence of fast cholinergic synaptic transmission. Furthermore, this cholinergic transmission alters the neuronal excitability of postsynaptic neurons, as monitored both *in vivo* and *ex vivo*. Using a fluorescent ACh sensor, we observed spontaneous ACh tone in the vlPAG, which was reduced by pain. In addition, exogenously increasing cholinergic tone relieves pain by modulating the activity of the postsynaptic vlPAG pain-encoding ensembles. Using similar approaches to investigate functions of ACh in the CNS further will advance our understanding of this enigmatic neurotransmitter.

Third, our research has primarily focused on cholinergic inputs from the PPTg, given their pain-modulatory effects. However, we observed anatomical inputs from other cholinergic nuclei, including LDTg and MS-DBB. While anatomical connectivity does not prove functional relevance, exploring these other cholinergic inputs in vlPAG function is an important area for future investigation. Along with pain modulation, vlPAG plays a role in REM sleep, and a similar function is attributed to the cholinergic neurons of the LDTg[183–185]. Whether LDTg cholinergic neurons modulate vlPAG REM sleep-regulating neurons is unknown. vlPAG also plays additional roles in fear encoding[186–188], deciding between coping strategies and stress encoding. Cholinergic projections from the basal forebrain to the amygdala play a critical role in the learning of aversive stimuli-predicting cues. Based on their encoding properties, cholinergic MS-DBB projections to the vlPAG could play a role in fear conditioning[105]. Expanding on the analgesic role of PPTg neurons identified in this study, recent investigations demonstrated that PPTg^{ChAT} regulates reversal learning and could thus further impact fear conditioning. Cholinergic neurons in the basal forebrain also regulate attention and cognitive functions of the cortex[189–192]. Evaluating the role of these cholinergic nuclei in the learning of painful stimuli-predicting cues or in attentional[193,194]- and placebo-analgesia[195–197] would be valuable for future investigations.

Our experiments indicate that the pain-relieving effects of increasing ACh levels are mediated through α7 nAChRs that inhibit vlPAG$^{\mathit{Oprm1+/GABA+}}$ interneurons. Recent studies have suggested that inhibiting vlPAG$^{\mathit{GABA+}}$ interneurons reduces acute pain[66,67], but their role in chronic pain conditions remained underexplored. We observed that inhibiting these interneurons relieves the chronic and affective components of pain, along with the effects of opioid withdrawal. Interestingly, we observed that higher frequencies of optogenetic activation of vlPAG$^{\mathit{GABA+}}$ interneurons reverse the inhibitory effects of α7 nAChR agonist. This suggests that vlPAG$^{\mathit{GABA+}}$ interneurons are tonically active and inhibit vlPAG projection neurons. These results cross-verify our *ex vivo* cell-attached recordings demonstrating the tonic activity of vlPAG$^{\mathit{Chrna7+}}$ neurons. Others have shown that vlPAG$^{\mathit{GABA+}}$ neurons undergo hyperexcitability under pain states[198–201], mirroring our observations of vlPAG$^{\mathit{Chrna7+}}$ interneurons. Our molecular profiling explored the overlap of α7 nAChRs with multiple known molecular markers of vlPAG neurons. Recent studies determined that vlPAG$^{\mathit{Tac1+}}$ and vlPAG$^{\mathit{Sst+}}$ neurons did not show pain modulatory effects, but did modulate itch[202]. We did not observe α7 nAChR mRNA expression on vlPAG$^{\mathit{Tac1+}}$ and vlPAG$^{\mathit{Sst+}}$ neurons, suggesting that vlPAG$^{\mathit{Chrna7+}}$ neurons are independent of these populations. While we attribute the main analgesic effects of activating PPTg$^{\mathit{ChAT+}}$→vlPAG to α7 nAChRs, intriguingly, we observed strong expression of M2 mAChRs in the vlPAG, agreeing with a previous study that suggested expression of mAChRs in the PAG[87]. Our M2 mAChR antagonist experiments suggest that M2 mAChRs may contribute to baseline pain sensitivity and thus may contribute to the onset of chronic pain physiology. Indeed, these M2 mAChRs were observed on GABAergic vlPAG interneurons that were activated during the formalin pain assay. Perhaps the decrease in ACh release in the vlPAG is *'sensed'* by decreased activation of M2 mAChRs[203,204], contributing to disinhibition of vlPAG$^{Chrna7+/Oprm1+/GABA+}$ interneurons. This mechanism is plausible given the higher affinity of M2 mAChR to ACh as compared to α7 nAChRs[203,204]. Further investigations exploring the role of M2 mAChRs in setting the baseline excitability of vlPAG ensembles and the pain sensitivity could help elucidate the role of these receptors in the vlPAG.

Our lab and others have reported analgesic actions of α7 nAChR agonists through central mechanisms[89,205–208]. Our previous study suggested that α7 nAChRs were partially expressed on vlPAG→RVM projection neurons that lack μ-opioid receptors, where they might increase excitability to relieve pain (29% vlPAG neurons expressed μ-opioid receptors, 27% α7 nAChRs, and 19% both receptors). That study explored μ-opioid receptor expression by monitoring changes in membrane current, with small effect sizes that were challenging to assess accurately. In this study, we have expanded our assessment to identify that α7 nAChRs are expressed predominantly on local interneurons where they alter the activity of vlPAG→RVM projection neurons, in a manner similar to opioid receptors[46,199]. Furthermore, that study was conducted in rats, where *Chrna7-Cre* lines are not available, making comprehensive assessment difficult. Finally, obtaining electrophysiological recordings from a large and representative neuronal population can be challenging. In the current study, we used complementary genetic, mRNA, protein, and physiological measures to demonstrate a much higher degree of overlap between μ-opioid receptors and α7 nAChR, and that these receptors are found on GABAergic vlPAG interneurons.

Unexpectedly, we also observed that α7 nAChRs relieve pain by inhibiting neuronal activity. This effect on physiology mediated by α7 nAChRs was surprising given their non-selective cation conductance and high Ca^{2+}-permeability[32]. Increasingly, studies are demonstrating that Ca^{2+}-permeable receptors may signal through non-canonical pathways and exert physiological effects beyond their ionotropic actions on neuronal excitability and synaptic plasticity[209–214]. Recently, NMDA receptors have been shown to activate metabotropic-like signaling pathways, extending our understanding of these receptors[27–31]. Similarly, α7 nAChRs have been proposed to couple to metabotropic signaling and exert physiological effects through phosphorylation of Erk-, Jak2/Stat3, and other kinases in various biological systems[215–217]. Elevating intracellular Ca^{2+} through these Ca^{2+} permeable receptors could induce an adaptive decrease in neuronal excitability, a conserved mechanism across various systems from inner ear hair cells to hippocampal neurons[218–221]. Our experiments suggest that a similar intracellular signaling cascade forms an essential substrate for the analgesic effects of α7 nAChR agonists. Furthermore, the time required for the decrease in neuronal excitability and the analgesic effects also suggests that these physiological and behavioral effects are triggered by intracellular signaling cascades that extend beyond transient receptor activation, ion flux, and elevated neuronal activity. Studies in other brain regions have indicated that activation of α7 nAChRs and other Ca^{2+} permeable AChRs can modulate neuronal physiology in unexpected ways, including phosphorylation of β2-subunit-containing nAChRs[148,149], calcineurin signaling[222–224], and activation of K_{Ca}-channels[225,226]. While our investigations showed minimal expression of other nAChR subtypes on these vlPAG$^{Chrna7+}$ neurons, we observed strong regulation of K_v2.1 phosphorylation by α7 nAChR agonists, mediating the decrease in excitability of these neurons. Our investigations also implicate non-genomic actions of PPARα in the analgesic effects, consistent with recent findings[145,227–232]. PPARα is involved in energy homeostasis and phosphorylation of AMP Kinase, a critical neuronal activity, and energy-sensing enzyme. While this endocannabinoid-like PPARα signaling regulates pain-related behaviors, our investigations also demonstrate the expression of CB1 receptors on vlPAG$^{Chrna7+}$ neurons. CB1R allosteric modulators can regulate vlPAG physiology and alter pain-related behaviors, suggesting a putative cellular target for endocannabinoids in pain modulation. Recently, systemic treatment of GAT211 was shown to relieve pain without losing efficacy over weeks of repeated treatment, with no rewarding effects and no withdrawal symptoms. These effects of GAT211 closely mimic the behavioral outcomes observed with activating PPTg^{ChAT+}→vlPAG neurons or α7 nAChR agonists[66,233–237]. Thus, these vlPAG neuronal ensembles could serve as a fascinating unexplored nexus where cholinergic, opioid, and endocannabinoid systems merge to regulate nocifensive behaviors. Reversing the maladaptive changes in the excitability of these pain-encoding neuronal ensembles will yield novel therapeutics for chronic pain conditions.

Future Directions

While our research has identified that activating cholinergic inputs to the vlPAG is analgesic, we do not know what the baseline cholinergic tone in the vlPAG encodes for. Spontaneous moment-by-moment transients of various neurotransmitters can encode multiple characteristics, e.g., dopamine levels in the nucleus accumbens are thought to encode the value of task engagement[238]. Identifying a similar underlying principle for the latent variable encoded by ACh in the vlPAG would yield significant insights. Current preliminary experiments suggest that ACh levels in the vlPAG are related to perceived physical efforts, without relating to movement. However, substantial work is necessary to elucidate the evolutionary role of ACh in the vlPAG.

We believe that while the analgesic effects of activating cholinergic inputs are mediated primarily through α7 nAChRs, the baseline cholinergic tone is primarily 'sensed' through higher affinity M2 mAChRs co-expressed in the vlPAG. M2 mAChRs are coupled to inhibitory intracellular signaling cascades. Thus, their disinhibition in chronic pain conditions could contribute to the observed hyperexcitability of GABAergic vlPAG neurons. Further electrophysiological and in vivo investigation could provide insights while providing an additional target for pain management. This research would also provide an exciting perspective where the same neurotransmitter contributes to different aspects of behavior based on the postsynaptic receptor signaling mechanisms.

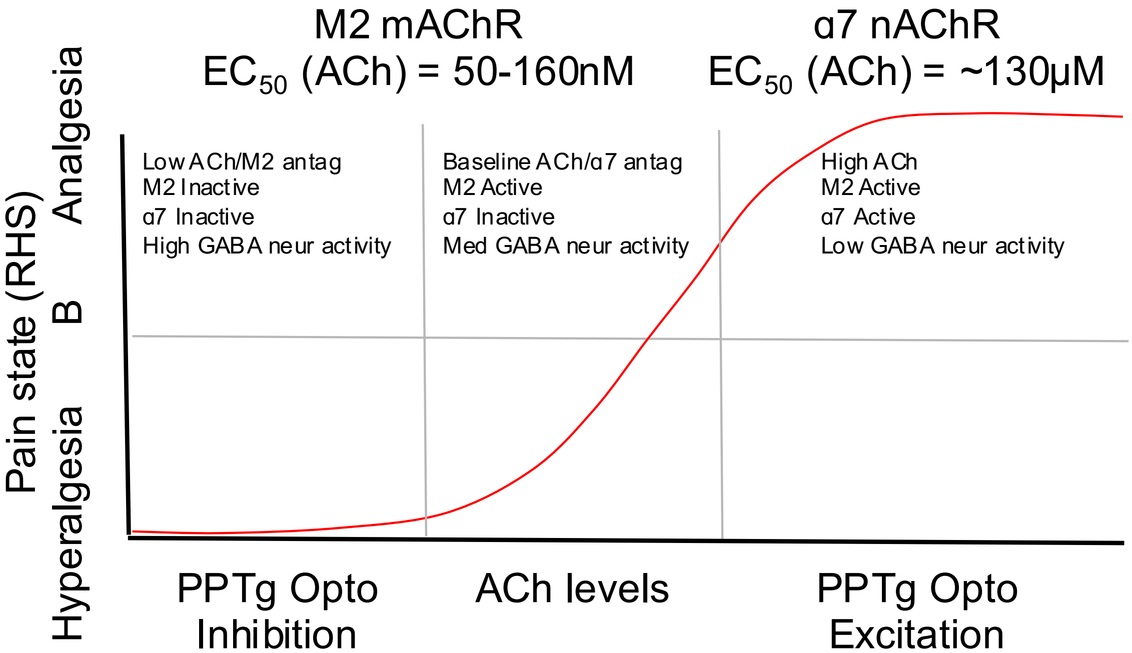

Figure 17: Dependence of analgesia on ACh levels and AChR activation in the vlPAG. Differential recruitment of M2 mAChRs and α7 nAChRs may contribute to diverse pathophysiological and behavioral impacts.

The role of ACh in the vlPAG in the context of learning and memory, especially from the perspective of synaptic plasticity, remains to be explored. These investigations could provide substantial insights into the learning and pain anticipation phenomenon that we have observed in the vlPAG. Additionally, the learning experiments need to be expanded along two directions: 1. Exploring the animal's pain state during the time when we observe the anticipatory rise in vlPAG activity, and 2. Identifying whether the anticipatory or conditioned increase in activity is a single-cell phenomenon or if it involves the recruitment of new cells into the pain-predictive ensemble. We are starting to conduct single-cell opto-tagged *in vivo* electrophysiology experiments in head-fixed animals. Future researchers could explore behavioral paradigms amenable to such recordings that allow appropriate assessment of these questions. After identifying answers, we would be curious if cholinergic inputs play a role in this learning phenomenon. While PPTg inputs are obvious candidates, medial septum also sparsely projects to the vlPAG. Septal cholinergic neurons might be ideally suited to guiding learning and synaptic plasticity in the vlPAG. We also believe that exploring orbitofrontal cortex (OFC) projections to the vlPAG might serve as a guide to this anticipatory learning, given the known functions of OFC. Hence, exploring the cholinergic modulation of excitatory synaptic drive from OFC presynaptic terminals in the vlPAG could serve as a valuable starting point. Some of our preliminary anatomical experiments with an *Oprm1-tdTomato* mouse line also identified strong expression of μ-opioid receptors in the orbitofrontal cortex (OFC). This expression could again be further explored using an *Oprm1-Cre* mouse line. Current preliminary single-unit *in vivo* electrophysical recordings of optically tagged OFC→vlPAG neurons strongly suggest that these neurons may play an essential role in anticipatory learning of painful stimuli. However, substantial work is necessary to truly disentangle these mechanisms.

Given that a dominant source of ACh in the vlPAG are the cholinergic neurons of the PPTg and pain alters ACh levels in the vlPAG, exploring the changes in intrinsic excitability of these PPTg neurons during chronic pain conditions could provide valuable mechanistic insights. Similarly, conducting detailed characterization of α7 nAChR and M2 mAChR expressing neurons to identify molecular and cellular changes associated with chronic pain states would be quite valuable from a therapeutic perspective. These investigations could employ single-cell RNA sequencing approaches to identify targets that show differential regulation after exposure to a chronic pain state.

We may be the most limited by the lack of robust anterograde tracing tools. We lack the ability to identify the anatomical projection targets of genetically defined populations of neurons. Such explorations would substantially help us determine the circuit-level impact of a neuronal population of interest. While we have employed synaptophysin-tagged approaches, the signal-to-noise associated with this method does not allow for unbiased discovery but rather just confirmations of known projection regions. Hence, better methods, similar to rabies virus tracing of presynaptic inputs, that anterogradely label postsynaptic partners would be a valuable asset to the field of circuit neuroscience. In the future, perhaps there will be better AAV1 serotypes that would allow viruses to jump to postsynaptic cells monosynaptically and fluorescently label the neurons allowing for robust anatomical circuit investigations. Given such tools, we would be interested in knowing whether α7 nAChR expressing vlPAG neurons are solely interneurons or if they have post-synaptic partners in brain regions other than the vlPAG. While the RVM could be a potential output, we are also curious about thalamic and cortical brain regions that may receive direct projections from these α7 nAChR expressing vlPAG neurons, as that would represent an additional avenue for exploration.

We demonstrate that inhibiting GABAergic vlPAG neurons using optogenetic or pharmacological approaches can be analgesic. The key is to find pharmacological agents that target these GABAergic vlPAG neurons. While we have conducted some fiber photometry experiments using iGABASnFR, we could not comprehensively survey all the receptor targets that we identified from our FISH assays. We are particularly excited about cannabinoid and orexin receptors expressed in the vlPAG. Orexin signaling has been implicated in hunger and sleep. Identifying the role of these receptors in the vlPAG could provide insights into how hunger or sleep regulates pain. We would want to focally infuse the agonist of CB1 or Orexin receptors while simultaneously monitoring GABA levels in the vlPAG using iGABASnFR and fiber photometry. Neuropeptides like dynorphin and enkephalin also modulate neurophysiology in the vlPAG. Exploring how these neuromodulators alter GABA levels could provide both mechanistic and therapeutic insights into the role of these neuropeptides in modulating pain.

Finally, the most significant limitation of this project was the knowledge that we had identified a pharmacological target that relieves pain, and yet, we cannot help individuals who are in desperate need of pain relief options. My satisfaction in this project would have been substantially improved if we had better access to clinicians to provide valuable guidance, better access to an appropriate patient population that keeps us motivated towards translationally relevant goals, and a more considered view of the broader implications of this research. Ideally, it would have been wonderful to collaborate with clinicians. However, a wise colleague once said: “If you can’t do it yourself, no one else is going to be interested in it either”. While we could not do it, we would be grateful if others could investigate whether Tropisetron, EVP-6124 (Encenicline), or a Positive Allosteric Modulator (PAM) of α7 nAChR, e.g., PNU 120596 would relieve pain in humans.

References

1. Guzman, M. S. *et al.* Elimination of the vesicular acetylcholine transporter in the striatum reveals regulation of behaviour by cholinergic-glutamatergic co-transmission. *PLoS Biol.* **9**, e1001194 (2011).

2. Teles-Grilo Ruivo, L. M. *et al.* Coordinated Acetylcholine Release in Prefrontal Cortex and Hippocampus Is Associated with Arousal and Reward on Distinct Timescales. *Cell Rep.* **18**, 905–917 (2017).

3. Morley, B. J., Lysakowski, A., Vijayakumar, S., Menapace, D. & Jones, T. A. Nicotinic acetylcholine receptors regulate vestibular afferent gain and activation timing. *J. Comp. Neurol.* **525**, 1216–1233 (2017).

4. Disney, A. A., Aoki, C. & Hawken, M. J. Gain modulation by nicotine in macaque v1. *Neuron* **56**, 701–13 (2007).

5. Puigbò, J.-Y. *et al.* Cholinergic Behavior State-Dependent Mechanisms of Neocortical Gain Control: a Neurocomputational Study. *Mol. Neurobiol.* **55**, 249–257 (2018).

6. Wilson, M. A. & Fadel, J. R. Cholinergic regulation of fear learning and extinction. *J. Neurosci. Res.* **95**, 836–852 (2017).

7. Jiang, L. *et al.* Cholinergic Signaling Controls Conditioned Fear Behaviors and Enhances Plasticity of Cortical-Amygdala Circuits. *Neuron* **90**, 1057–70 (2016).

8. Picciotto, M. R., Higley, M. J. & Mineur, Y. S. Acetylcholine as a neuromodulator: cholinergic signaling shapes nervous system function and behavior. *Neuron* **76**, 116–29 (2012).

9. Parikh, V., Kozak, R., Martinez, V. & Sarter, M. Prefrontal Acetylcholine Release Controls Cue Detection on Multiple Timescales. *Neuron* **56**, 141–154 (2007).

10. Ballinger, E. C., Ananth, M., Talmage, D. A. & Role, L. W. Basal Forebrain Cholinergic Circuits and Signaling in Cognition and Cognitive Decline. *Neuron* **91**, 1199–1218 (2016).

11. Luchicchi, A., Bloem, B., Viaña, J. N. M., Mansvelder, H. D. & Role, L. W. Illuminating the role of cholinergic signaling in circuits of attention and emotionally salient behaviors. *Front. Synaptic Neurosci.* **6**, 24 (2014).

12. Decker, M. W., Brioni, J. D., Bannon, A. W. & Arneric, S. P. Diversity of neuronal nicotinic acetylcholine receptors: lessons from behavior and implications for CNS therapeutics. *Life Sci.* **56**, 545–70 (1995).

13. Jiang, L., López-Hernández, G. Y., Lederman, J., Talmage, D. A. & Role, L. W.

Optogenetic studies of nicotinic contributions to cholinergic signaling in the central nervous system. *Rev. Neurosci.* **25**, 755–771 (2014).

14. Mark, G. P., Shabani, S., Dobbs, L. K. & Hansen, S. T. Cholinergic modulation of mesolimbic dopamine function and reward. *Physiol. Behav.* **104**, 76–81 (2011).

15. Sarter, M., Parikh, V. & Howe, W. M. Phasic acetylcholine release and the volume transmission hypothesis: time to move on. *Nat. Rev. Neurosci.* **10**, 383–90 (2009).

16. Galindo-Charles, L. *et al.* Serotoninergic dorsal raphe neurons possess functional postsynaptic nicotinic acetylcholine receptors. *Synapse* **62**, 601–15 (2008).

17. Power, S. K., Venkatesan, S. & Lambe, E. K. Xanomeline restores endogenous nicotinic acetylcholine receptor signaling in mouse prefrontal cortex. *Neuropsychopharmacology* **48**, 671–682 (2023).

18. Li, X., Rainnie, D. G., McCarley, R. W. & Greene, R. W. Presynaptic nicotinic receptors facilitate monoaminergic transmission. *J. Neurosci.* **18**, 1904–1912 (1998).

19. Mao, D., Gallagher, K. & McGehee, D. S. Nicotine potentiation of excitatory inputs to ventral tegmental area dopamine neurons. *J. Neurosci.* **31**, 6710–20 (2011).

20. Genzen, J. R. & McGehee, D. S. Short- and long-term enhancement of excitatory transmission in the spinal cord dorsal horn by nicotinic acetylcholine receptors. *Proc. Natl. Acad. Sci. U. S. A.* **100**, 6807–6812 (2003).

21. Yan, Y. *et al.* Nicotinic Cholinergic Receptors in VTA Glutamate Neurons Modulate Excitatory Transmission. *Cell Rep.* **23**, 2236–2244 (2018).

22. Ren, J. *et al.* Habenula ‘ Cholinergic’ Neurons Corelease Glutamate and Acetylcholine and Activate Postsynaptic Neurons via Distinct Transmission Modes. *Neuron* **69**, 445–452 (2011).

23. Jones, C. K., Byun, N. & Bubser, M. Muscarinic and Nicotinic Acetylcholine Receptor Agonists and Allosteric Modulators for the Treatment of Schizophrenia. *Neuropsychopharmacology* **37**, 16–42 (2012).

24. Li, X. *et al.* Generation of a whole-brain atlas for the cholinergic system and mesoscopic projectome analysis of basal forebrain cholinergic neurons. *Proc. Natl. Acad. Sci.* **115**, 415–420 (2018).

25. Gong, S. & Ford, C. P. Cholinergic Interneurons Provide a Link to Balance Excitation across Striatal Output Neurons. *Neuron* **103**, 351–353 (2019).

26. Augustin, S. M., Chancey, J. H. & Lovinger, D. M. Dual Dopaminergic Regulation of Corticostriatal Plasticity by Cholinergic Interneurons and Indirect Pathway Medium Spiny Neurons. *Cell Rep.* **24**, 2883–2893 (2018).

27. Dore, K. *et al.* Unconventional NMDA Receptor Signaling. *J. Neurosci.* **37**, 10800–10807 (2017).

28. Valbuena, S. & Lerma, J. Non-canonical Signaling, the Hidden Life of Ligand-Gated Ion Channels. *Neuron* **92**, 316–329 (2016).

29. Aow, J., Dore, K. & Malinow, R. Conformational signaling required for synaptic plasticity by the NMDA receptor complex. *Proc. Natl. Acad. Sci. U. S. A.* **112**, 14711–6 (2015).

30. Nabavi, S. *et al.* Metabotropic NMDA receptor function is required for NMDA receptor-dependent long-term depression. *Proc. Natl. Acad. Sci. U. S. A.* **110**, 4027–32 (2013).

31. Dore, K., Aow, J. & Malinow, R. The Emergence of NMDA Receptor Metabotropic Function: Insights from Imaging. *Front. Synaptic Neurosci.* **8**, 20 (2016).

32. Séguéla, P. *et al.* Molecular cloning, functional properties, and distribution of rat brain alpha 7: a nicotinic cation channel highly permeable to calcium. *J. Neurosci.* **13**, 596–604 (1993).

33. Dahlhamer, J. *et al.* Prevalence of Chronic Pain and High-Impact Chronic Pain Among Adults - United States, 2016. *MMWR. Morb. Mortal. Wkly. Rep.* **67**, 1001–1006 (2018).

34. Fields, H. State-dependent opioid control of pain. *Nat. Rev. Neurosci.* **5**, 565–75 (2004).

35. Brodin, E., Ernberg, M. & Olgart, L. Neurobiology: General considerations - from acute to chronic pain. *Den Nor. Tann. Tid.* **126**, (2016).

36. Mu, D. *et al.* A central neural circuit for itch sensation. *Science* **357**, 695–699 (2017).

37. Todd, A. J. Neuronal circuitry for pain processing in the dorsal horn. *Nat. Rev. Neurosci.* **11**, 823–36 (2010).

38. Gao, Z.-R. *et al.* Tac1-Expressing Neurons in the Periaqueductal Gray Facilitate the Itch-Scratching Cycle via Descending Regulation. *Neuron* **101**, 45-59.e9 (2019).

39. Corder, G. *et al. An amygdalar neural ensemble that encodes the unpleasantness of pain. Science* vol. 363 (2019).

40. Basbaum, A. I. & Fields, H. L. Endogenous pain control systems: brainstem spinal pathways and endorphin circuitry. *Annu. Rev. Neurosci.* **7**, 309–38 (1984).

41. Heinricher, M. M. Pain Modulation and the Transition from Acute to Chronic Pain. *Adv. Exp. Med. Biol.* **904**, 105–15 (2016).

42. Heinricher, M. M., Tavares, I., Leith, J. L. & Lumb, B. M. Descending control of nociception: Specificity, recruitment and plasticity. *Brain Res. Rev.* **60**, 214–25 (2009).

43. Fields, H. L. & Heinricher, M. M. Anatomy and physiology of a nociceptive modulatory system. *Philos. Trans. R. Soc. Lond. B. Biol. Sci.* **308**, 361–74 (1985).

44. Heinricher, M. M., Cheng, Z. F. & Fields, H. L. Evidence for two classes of nociceptive modulating neurons in the periaqueductal gray. *J. Neurosci.* **7**, 271–278 (1987).

45. Samineni, V. K., Premkumar, L. S. & Faingold, C. L. Neuropathic pain-induced enhancement of spontaneous and pain-evoked neuronal activity in the periaqueductal gray that is attenuated by gabapentin. *Pain* **158**, 1241–1253 (2017).

46. Vaughan, C. W., Ingram, S. L., Connor, M. A. & Christie, M. J. How opioids inhibit GABA-mediated neurotransmission. *Nature* **390**, 611–614 (1997).

47. Kim, J.-H. *et al.* Yin-and-yang bifurcation of opioidergic circuits for descending analgesia at the midbrain of the mouse. *Proc. Natl. Acad. Sci. U. S. A.* **115**, 11078–11083 (2018).

48. Behbehani, M. M. Functional characteristics of the midbrain periaqueductal gray. *Prog. Neurobiol.* **46**, 575–605 (1995).

49. Bennett, G. J. & Mayer, D. J. Inhibition of spinal cord interneurons by narcotic microinjection and focal electrical stimulation in the periaqueductal central gray matter. *Brain Res.* **172**, 243–57 (1979).

50. Carstens, E., Hartung, M., Stelzer, B. & Zimmermann, M. Suppression of a hind limb flexion withdrawal reflex by microinjection of glutamate or morphine into the periaqueductal gray in the rat. *Pain* **43**, 105–112 (1990).

51. Carstens, E., Stelzer, B. & Zimmermann, M. Microinjections of glutamate or morphine at coincident midbrain sites have different effects on nociceptive dorsal horn neurons in the rat. *Neurosci. Lett.* **95**, 185–91 (1988).

52. Depaulis, A., Morgan, M. M. & Liebeskind, J. C. GABAergic modulation of the analgesic effects of morphine microinjected in the ventral periaqueductal gray matter of the rat. *Brain Res.* **436**, 223–228 (1987).

53. Heinricher, M. M., Martenson, M. E. & Neubert, M. J. Prostaglandin E2 in the midbrain periaqueductal gray produces hyperalgesia and activates pain-modulating circuitry in the rostral ventromedial medulla. *Pain* **110**, 419–426 (2004).

54. Jensen, T. S. & Yaksh, T. L. Comparison of the antinociceptive effect of morphine and glutamate at coincidental sites in the periaqueductal gray and medial medulla in rats. *Brain Res.* **476**, 1–9 (1989).

55. Pertovaara, A., Wei, H. & Hämäläinen, M. M. Lidocaine in the rostroventromedial medulla and the periaqueductal gray attenuates allodynia in neuropathic rats. *Neurosci. Lett.* **218**, 127–30 (1996).

56. Roychowdhury, S. M. & Fields, H. L. Endogenous opioids acting at a medullary mu-opioid receptor contribute to the behavioral antinociception produced by GABA antagonism in the midbrain periaqueductal gray. *Neuroscience* **74**, 863–72 (1996).

57. Sandkühler, J., Willmann, E. & Fu, Q. G. Blockade of GABAA receptors in the midbrain periaqueductal gray abolishes nociceptive spinal dorsal horn neuronal activity. *Eur. J. Pharmacol.* **160**, 163–6 (1989).

58. Hosobuchi, Y., Adams, J. E. & Linchitz, R. Pain relief by electrical stimulation of the central gray matter in humans and its reversal by naloxone. *Science* **197**, 183–6 (1977).

59. Jones, S. L. & Gebhart, G. F. Inhibition of spinal nociceptive transmission from the midbrain, pons and medulla in the rat: activation of descending inhibition by morphine, glutamate and electrical stimulation. *Brain Res.* **460**, 281–96 (1988).

60. Liebeskind, J. C., Guilbaud, G., Besson, J. M. & Oliveras, J. L. Analgesia from electrical stimulation of the periaqueductal gray matter in the cat: behavioral observations and inhibitory effects on spinal cord interneurons. *Brain Res.* **50**, 441–6 (1973).

61. Mayer, D. J. & Liebeskind, J. C. Pain reduction by focal electrical stimulation of the brain: an anatomical and behavioral analysis. *Brain Res.* **68**, 73–93 (1974).

62. Millan, M. J., Członkowski, A., Millan, M. H. & Herz, A. Activation of periaqueductal grey pools of beta-endorphin by analgetic electrical stimulation in freely moving rats. *Brain Res.* **407**, 199–203 (1987).

63. Morgan, M. M., Sohn, J. H. & Liebeskind, J. C. Stimulation of the periaqueductal gray matter inhibits nociception at the supraspinal as well as spinal level. *Brain Res.* **502**, 61–6 (1989).

64. Reynolds, D. V. Surgery in the Rat during Electrical Analgesia Induced by Focal Brain Stimulation Sex Differences in Verbal and Performance IQ's of Children Undergoing Open-Heart Surgery. *Science (80-.).* **164**, 444–445 (1969).

65. Behbehani, M. M., Jiang, M., Chandler, S. D. & Ennis, M. The effect of GABA and its antagonists on midbrain periaqueductal gray neurons in the rat. *Pain* **40**, 195–204 (1990).

66. Zhu, H. *et al.* Inhibition of GABAergic Neurons and Excitation of Glutamatergic Neurons in the Ventrolateral Periaqueductal Gray Participate in Electroacupuncture Analgesia Mediated by Cannabinoid Receptor. *Front. Neurosci.* **13**, 484 (2019).

67. Samineni, V. K. *et al.* Divergent Modulation of Nociception by Glutamatergic and GABAergic Neuronal Subpopulations in the Periaqueductal Gray. *eNeuro* **4**, ENEURO.0129-16.2017 (2017).

68. Yang, L. *et al.* Ventrolateral periaqueductal gray astrocytes regulate nociceptive sensation and emotional motivation in diabetic neuropathic pain. *J. Neurosci.* (2022)

doi:10.1523/JNEUROSCI.0920-22.2022.

69. Taylor, N. E. *et al.* The Role of Glutamatergic and Dopaminergic Neurons in the Periaqueductal Gray/Dorsal Raphe: Separating Analgesia and Anxiety. *eNeuro* **6**,.

70. Wager, T. D. *et al.* Placebo-induced changes in FMRI in the anticipation and experience of pain. *Science* **303**, 1162–7 (2004).

71. Schafer, S. M., Geuter, S. & Wager, T. D. Mechanisms of placebo analgesia: A dual-process model informed by insights from cross-species comparisons. *Prog. Neurobiol.* **160**, 101–122 (2018).

72. Huang, J. *et al.* Modulation of Neuropathic Pain. *Nat. Neurosci.* doi:10.1038/s41593-019-0481-5.

73. Huang, J., Zhang, Z., Gambeta, E., Chen, L. & Zamponi, G. W. An orbitofrontal cortex to midbrain projection modulates hypersensitivity after peripheral nerve injury. *Cell Rep.* **35**, 109033 (2021).

74. Huang, J. *et al.* A neuronal circuit for activating descending modulation of neuropathic pain. *Nat. Neurosci.* **22**, 1659–1668 (2019).

75. Zhang, Z. *et al.* Role of Prelimbic GABAergic Circuits in Sensory and Emotional Aspects of Neuropathic Pain. *Cell Rep.* **12**, 752–759 (2015).

76. Alhadeff, A. L. *et al.* A Neural Circuit for the Suppression of Pain by a Competing Need State. *Cell* **173**, 140-152.e15 (2018).

77. Hao, S. *et al.* The Lateral Hypothalamic and BNST GABAergic Projections to the Anterior Ventrolateral Periaqueductal Gray Regulate Feeding. *Cell Rep.* **28**, 616-624.e5 (2019).

78. Avegno, E. M. *et al.* Central Amygdala Circuits Mediate Hyperalgesia in Alcohol-Dependent Rats. *J. Neurosci.* **38**, 7761–7773 (2018).

79. Li, J.-N. & Sheets, P. L. The central amygdala to periaqueductal gray pathway comprises intrinsically distinct neurons differentially affected in a model of inflammatory pain. *J. Physiol.* **596**, 6289–6305 (2018).

80. Faull, O. K. & Pattinson, K. T. The cortical connectivity of the periaqueductal gray and the conditioned response to the threat of breathlessness. *Elife* **6**, (2017).

81. Floyd, N. S., Price, J. L., Ferry, A. T., Keay, K. A. & Bandler, R. Orbitomedial prefrontal cortical projections to distinct longitudinal columns of the periaqueductal gray in the rat. *J. Comp. Neurol.* **422**, 556–578 (2000).

82. Vianna, D. M. L. & Brandão, M. L. Anatomical connections of the periaqueductal gray:

specific neural substrates for different kinds of fear. *Brazilian J. Med. Biol. Res. = Rev. Bras. Pesqui. medicas e Biol.* **36**, 557–66 (2003).

83. Mason, P. Medullary circuits for nociceptive modulation. *Curr. Opin. Neurobiol.* **22**, 640–5 (2012).

84. Romano, J. A. & Shih, T. M. Cholinergic mechanisms of analgesia produced by physostigmine, morphine and cold water swimming. *Neuropharmacology* **22**, 827–833 (1983).

85. Naser, P. V. & Kuner, R. Molecular, Cellular and Circuit Basis of Cholinergic Modulation of Pain. *Neuroscience* **387**, 135–148 (2018).

86. McClintick, J. N. *et al.* Gene Expression Changes in Glutamate and GABA-A Receptors, Neuropeptides, Ion Channels, and Cholesterol Synthesis in the Periaqueductal Gray Following Binge-Like Alcohol Drinking by Adolescent Alcohol-Preferring (P) Rats. *Alcohol. Clin. Exp. Res.* **40**, 955–68 (2016).

87. Lau, B. K. & Vaughan, C. W. Muscarinic modulation of synaptic transmission via endocannabinoid signalling in the rat midbrain periaqueductal gray. *Mol. Pharmacol.* **74**, 1392–8 (2008).

88. Yang, C. & Brown, R. E. The cholinergic agonist carbachol increases the frequency of spontaneous GABAergic synaptic currents in dorsal raphe serotonergic neurons in the mouse. *Neuroscience* **258**, 62–73 (2014).

89. Umana, I. C. *et al.* Nicotinic modulation of descending pain control circuitry. *Pain* **158**, 1938–1950 (2017).

90. Jing, M. *et al.* An optimized acetylcholine sensor for monitoring in vivo cholinergic activity. *Nat. Methods* **17**, 1139–1146 (2020).

91. Sherathiya, V. N., Schaid, M. D., Seiler, J. L., Lopez, G. C. & Lerner, T. N. GuPPy, a Python toolbox for the analysis of fiber photometry data. *Sci. Rep.* **11**, (2021).

92. Bruno, C. A. *et al.* pMAT: An open-source software suite for the analysis of fiber photometry data. *Pharmacol. Biochem. Behav.* **201**, 173093 (2021).

93. Cantu, D. A. *et al.* EZcalcium: Open-Source Toolbox for Analysis of Calcium Imaging Data. *Front. Neural Circuits* **14**, 1–9 (2020).

94. Aharoni, D. & Hoogland, T. M. Circuit Investigations With Open-Source Miniaturized Microscopes: Past, Present and Future. *Front. Cell. Neurosci.* **13**, 1–12 (2019).

95. Friedrich, J., Giovannucci, A. & Pnevmatikakis, E. A. *Online analysis of microendoscopic 1-photon calcium imaging data streams*. *PLoS Computational Biology* vol. 17 (2021).

96. Campos, P., Walker, J. J. & Mollard, P. Diving into the brain: Deep-brain imaging techniques in conscious animals. *J. Endocrinol.* **246**, R33–R50 (2020).

97. Rossi, M. A. *et al.* Obesity remodels activity and transcriptional state of a lateral hypothalamic brake on feeding. *Science (80-.).* **364**, 1271–1274 (2019).

98. Sheintuch, L. *et al.* Tracking the Same Neurons across Multiple Days in Ca2+ Imaging Data. *Cell Rep.* **21**, 1102–1115 (2017).

99. Bannon, A. W. & Malmberg, A. B. Models of nociception: hot-plate, tail-flick, and formalin tests in rodents. *Curr. Protoc. Neurosci.* **Chapter 8**, Unit 8.9 (2007).

100. Tervo, D. G. R. *et al.* A Designer AAV Variant Permits Efficient Retrograde Access to Projection Neurons. *Neuron* **92**, 372–382 (2016).

101. Bäck, S. *et al.* Neuron-Specific Genome Modification in the Adult Rat Brain Using CRISPR-Cas9 Transgenic Rats. *Neuron* **102**, 105-119.e8 (2019).

102. Wang, H.-L. & Morales, M. Pedunculopontine and laterodorsal tegmental nuclei contain distinct populations of cholinergic, glutamatergic and GABAergic neurons in the rat. *Eur. J. Neurosci.* **29**, 340–58 (2009).

103. Beitz, A. J. The organization of afferent projections to the midbrain periaqueductal gray of the rat. *Neuroscience* **7**, 133–59 (1982).

104. Deisseroth, K. Optogenetics: 10 years of microbial opsins in neuroscience. *Nat. Neurosci.* **18**, 1213–25 (2015).

105. Ruan, Y. *et al.* Cholinergic neurons in the pedunculopontine nucleus guide reversal learning by signaling the changing reward contingency. *Cell Rep.* **38**, 110437 (2022).

106. Prut, L. & Belzung, C. The open field as a paradigm to measure the effects of drugs on anxiety-like behaviors: a review. *Eur. J. Pharmacol.* **463**, 3–33 (2003).

107. Deacon, R. M. J. Measuring motor coordination in mice. *J. Vis. Exp.* e2609 (2013) doi:10.3791/2609.

108. Corder, G. *et al.* Loss of μ opioid receptor signaling in nociceptors, but not microglia, abrogates morphine tolerance without disrupting analgesia. *Nat. Med.* **23**, 164–173 (2017).

109. Dumas, E. O. & Pollack, G. M. Opioid tolerance development: a pharmacokinetic/pharmacodynamic perspective. *AAPS J.* **10**, 537–51 (2008).

110. Kieffer, B. L. & Evans, C. J. Opioid tolerance-in search of the holy grail. *Cell* **108**, 587–90 (2002).

111. Cahill, C. M., Walwyn, W., Taylor, A. M. W., Pradhan, A. A. A. & Evans, C. J. Allostatic

Mechanisms of Opioid Tolerance Beyond Desensitization and Downregulation. *Trends Pharmacol. Sci.* **37**, 963–976 (2016).

112. Wang, F. *et al.* RNAscope: a novel in situ RNA analysis platform for formalin-fixed, paraffin-embedded tissues. *J. Mol. Diagn.* **14**, 22–9 (2012).

113. Sarter, M. & Lustig, C. Forebrain Cholinergic Signaling: Wired and Phasic, Not Tonic, and Causing Behavior. *J. Neurosci.* **40**, 712–719 (2020).

114. Disney, A. A. & Higley, M. J. Diverse Spatiotemporal Scales of Cholinergic Signaling in the Neocortex. *J. Neurosci.* **40**, 720–725 (2020).

115. Siegel, R. K., Gusewelle, B. E. & Jarvik, M. E. Naloxone-induced jumping in morphine dependent mice: stimulus control and motivation. *Int. Pharmacopsychiatry* **10**, 17–23 (1975).

116. Kaka, G., Rahmanzade, R., Safee, F. & Haghparast, A. Naloxone induces frequent jumping after chronic morphine and methamphetamine co-administration in rats. *Basic Clin. Neurosci.* **5**, 42–7 (2014).

117. García-Carmona, J. A., Baroja-Mazo, A., Milanés, M. V. & Laorden, M. L. Sex differences between CRF1 receptor deficient mice following naloxone-precipitated morphine withdrawal in a conditioned place aversion paradigm: Implication of HPA axis. *PLoS One* **10**, 1–16 (2015).

118. Sharf, R., Sarhan, M. & Dileone, R. J. Role of orexin/hypocretin in dependence and addiction. *Brain Res.* **1314**, 130–8 (2010).

119. Alvarez-Bagnarol, Y., Marchette, R. C. N., Francis, C., Morales, M. M. & Vendruscolo, L. F. NEURONAL CORRELATES OF HYPERALGESIA AND SOMATIC SIGNS OF HEROIN WITHDRAWAL IN MALE AND FEMALE MICE. *eNeuro* (2022) doi:10.1523/ENEURO.0106-22.2022.

120. Rodriguez, E. *et al.* A craniofacial-specific monosynaptic circuit enables heightened affective pain. *Nat. Neurosci.* **20**, 1734–1743 (2017).

121. Prickaerts, J. *et al.* EVP-6124, a novel and selective α7 nicotinic acetylcholine receptor partial agonist, improves memory performance by potentiating the acetylcholine response of α7 nicotinic acetylcholine receptors. *Neuropharmacology* **62**, 1099–110 (2012).

122. Vallés, A. S. & Barrantes, F. J. Interactions between the Nicotinic and Endocannabinoid Receptors at the Plasma Membrane. *Membranes (Basel).* **12**, (2022).

123. Melis, M. & Pistis, M. Hub and switches: endocannabinoid signalling in midbrain dopamine neurons. *Philos. Trans. R. Soc. Lond. B. Biol. Sci.* **367**, 3276–85 (2012).

124. Melis, M. *et al.* PPARα regulates cholinergic-driven activity of midbrain dopamine

neurons via a novel mechanism involving α7 nicotinic acetylcholine receptors. *J. Neurosci.* **33**, 6203–6211 (2013).

125. Huang, W.-J., Chen, W.-W. & Zhang, X. Endocannabinoid system: Role in depression, reward and pain control (Review). *Mol. Med. Rep.* **14**, 2899–903 (2016).

126. Sagar, D. R. *et al.* Tonic modulation of spinal hyperexcitability by the endocannabinoid receptor system in a rat model of osteoarthritis pain. *Arthritis Rheum.* **62**, 3666–76 (2010).

127. Costa, M. *et al.* Investigation of endocannabinoid system genes suggests association between peroxisome proliferator activator receptor-α gene (PPARA) and schizophrenia. *Eur. Neuropsychopharmacol.* **23**, 749–59 (2013).

128. Okine, B. N., Gaspar, J. C. & Finn, D. P. PPARs and pain. *Br. J. Pharmacol.* **176**, 1421–1442 (2019).

129. Maeda, T. & Kishioka, S. PPAR and Pain. *Int. Rev. Neurobiol.* **85**, 165–77 (2009).

130. Donvito, G., Wilkerson, J. L., Damaj, M. I. & Lichtman, A. H. Palmitoylethanolamide Reverses Paclitaxel-Induced Allodynia in Mice. *J. Pharmacol. Exp. Ther.* **359**, 310–318 (2016).

131. Caillaud, M. *et al.* Targeting Peroxisome Proliferator-Activated Receptor-α (PPAR- α) to reduce paclitaxel-induced peripheral neuropathy. *Brain. Behav. Immun.* **93**, 172–185 (2021).

132. Jackson, A. *et al.* In vivo interactions between α7 nicotinic acetylcholine receptor and nuclear peroxisome proliferator-activated receptor-α: Implication for nicotine dependence. *Neuropharmacology* **118**, 38–45 (2017).

133. Lee, W. H. & Kim, S. G. AMPK-Dependent Metabolic Regulation by PPAR Agonists. *PPAR Res.* **2010**, (2010).

134. Asiedu, M. N., Dussor, G. & Price, T. J. Targeting AMPK for the Alleviation of Pathological Pain. *Exp. Suppl.* **107**, 257–285.

135. Wang, S. & Dai, Y. Roles of AMPK and Its Downstream Signals in Pain Regulation. *Life (Basel, Switzerland)* **11**, (2021).

136. Xiang, H.-C. *et al.* AMPK activation attenuates inflammatory pain through inhibiting NF-κB activation and IL-1β expression. *J. Neuroinflammation* **16**, 34 (2019).

137. Price, T. J. & Dussor, G. AMPK: An emerging target for modification of injury-induced pain plasticity. *Neurosci. Lett.* **557 Pt A**, 9–18 (2013).

138. Bullón, P. *et al.* AMPK Phosphorylation Modulates Pain by Activation of NLRP3 Inflammasome. *Antioxid. Redox Signal.* **24**, 157–70 (2016).

139. Tsantoulas, C. *et al.* Kv2 dysfunction after peripheral axotomy enhances sensory neuron responsiveness to sustained input. *Exp. Neurol.* **251**, 115–26 (2014).

140. Zhu, X. *et al.* SP6616 as a Kv2.1 inhibitor efficiently ameliorates peripheral neuropathy in diabetic mice. *EBioMedicine* **61**, 103061 (2020).

141. Eacret, D., Noreck, J. & Blendy, J. A. Adenosine Monophosphate-activated Protein Kinase (AMPK) in serotonin neurons mediates select behaviors during protracted withdrawal from morphine in mice. *Behav. Brain Res.* **419**, (2022).

142. Zhang, Y. *et al.* Lidocaine alleviates morphine tolerance via AMPK-SOCS3-dependent neuroinflammation suppression in the spinal cord. *J. Neuroinflammation* **14**, 211 (2017).

143. Li, L., Zhang, H., Li, T. & Zhang, B. Involvement of adenosine monophosphate-activated protein kinase in morphine-induced cardioprotection. *J. Surg. Res.* **169**, 179–87 (2011).

144. Pan, Y. *et al.* Metformin reduces morphine tolerance by inhibiting microglial-mediated neuroinflammation. *J. Neuroinflammation* **13**, 294 (2016).

145. Muraleedharan, R. & Dasgupta, B. AMPK in the brain: its roles in glucose and neural metabolism. *FEBS J.* **289**, 2247–2262 (2022).

146. Misonou, H., Mohapatra, D. P. & Trimmer, J. S. Kv2.1: a voltage-gated k+ channel critical to dynamic control of neuronal excitability. *Neurotoxicology* **26**, 743–52 (2005).

147. Ikematsu, N. *et al.* Phosphorylation of the voltage-gated potassium channel Kv2.1 by AMP-activated protein kinase regulates membrane excitability. *Proc. Natl. Acad. Sci. U. S. A.* **108**, 18132–18137 (2011).

148. Melis, M. *et al.* PPAR Regulates Cholinergic-Driven Activity of Midbrain Dopamine Neurons via a Novel Mechanism Involving 7 Nicotinic Acetylcholine Receptors. *J. Neurosci.* **33**, 6203–6211 (2013).

149. Melis, M. *et al.* Peroxisome proliferator-activated receptors-alpha modulate dopamine cell activity through nicotinic receptors. *Biol. Psychiatry* **68**, 256–264 (2010).

150. Donvito, G. *et al.* The interaction between alpha 7 nicotinic acetylcholine receptor and nuclear peroxisome proliferator-activated receptor-α represents a new antinociceptive signaling pathway in mice. *Exp. Neurol.* **295**, 194–201 (2017).

151. Jackson, A., Alkhlaif, Y., Papke, R. L., Brunzell, D. H. & Damaj, M. I. Impact of modulation of the α7 nicotinic acetylcholine receptor on nicotine reward in the mouse conditioned place preference test. *Psychopharmacology (Berl).* **236**, 3593–3599 (2019).

152. Freitas, K., Ghosh, S., Ivy Carroll, F., Lichtman, A. H. & Imad Damaj, M. Effects of alpha 7 positive allosteric modulators in murine inflammatory and chronic neuropathic pain models. *Neuropharmacology* **65**, 156–164 (2013).

153. Guo, H. *et al.* Naloxone reversed cognitive impairments induced by repeated morphine under heavy perceptual load in the 5-choice serial reaction time task. *J. Neurosci. Res.* **97**, 1051–1065 (2019).

154. Kitanaka, J. *et al.* Memory impairment and reduced exploratory behavior in mice after administration of systemic morphine. *J. Exp. Neurosci.* **9**, 27–35 (2015).

155. Murphy, N. P., Lam, H. A. & Maidment, N. T. A comparison of morphine-induced locomotor activity and mesolimbic dopamine release in C57BL6, 129Sv and DBA2 mice. *J. Neurochem.* **79**, 626–35 (2001).

156. Denk, F., McMahon, S. B. & Tracey, I. Pain vulnerability: a neurobiological perspective. *Nat. Neurosci.* **17**, 192–200 (2014).

157. Waxman, S. G. & Zamponi, G. W. Regulating excitability of peripheral afferents: emerging ion channel targets. *Nat. Neurosci.* **17**, 153–63 (2014).

158. Piomelli, D. & Sasso, O. Peripheral gating of pain signals by endogenous lipid mediators. *Nat. Neurosci.* **17**, 164–74 (2014).

159. Prescott, S. A., Ma, Q. & De Koninck, Y. Normal and abnormal coding of somatosensory stimuli causing pain. *Nat. Neurosci.* **17**, 183–91 (2014).

160. Kuner, R. & Flor, H. Structural plasticity and reorganisation in chronic pain. *Nat. Rev. Neurosci.* **18**, 20–30 (2016).

161. Zhu, X. *et al.* Rostral Anterior Cingulate Cortex-Ventrolateral Periaqueductal Gray Circuit Underlies Electroacupuncture to Alleviate Hyperalgesia but Not Anxiety-Like Behaviors in Mice With Spared Nerve Injury. *Front. Neurosci.* **15**, 757628 (2021).

162. Sun, Y. *et al.* Involvement of the Ventrolateral Periaqueductal Gray Matter-Central Medial Thalamic Nucleus-Basolateral Amygdala Pathway in Neuropathic Pain Regulation of Rats. *Front. Neuroanat.* **14**, 32 (2020).

163. Yin, J.-B. *et al.* dmPFC-vlPAG projection neurons contribute to pain threshold maintenance and antianxiety behaviors. *J. Clin. Invest.* **130**, 6555–6570 (2020).

164. Sun, Y. *et al.* Amygdala GABA Neurons Project To vlPAG And mPFC. *IBRO reports* **6**, 132–136 (2019).

165. Li, J.-N. *et al.* Projections from the lateral parabrachial nucleus to the lateral and ventral lateral periaqueductal gray subregions mediate the itching sensation. *Pain* **162**, 1848–1863 (2021).

166. Yeh, L.-F., Ozawa, T. & Johansen, J. P. Functional organization of the midbrain periaqueductal gray for regulating aversive memory formation. *Mol. Brain* **14**, 136 (2021).

167. Kim, J. H. *et al.* Yin-and-yang bifurcation of opioidergic circuits for descending analgesia at the midbrain of the mouse. *Proc. Natl. Acad. Sci. U. S. A.* **115**, 11078–11083 (2018).

168. Geppetti, P. & Benemei, S. Pain treatment with opioids : achieving the minimal effective and the minimal interacting dose. *Clin. Drug Investig.* **29 Suppl 1**, 3–16 (2009).

169. Volkow, N., Benveniste, H. & McLellan, A. T. Use and Misuse of Opioids in Chronic Pain. *Annu. Rev. Med.* **69**, 451–465 (2018).

170. Labianca, R. *et al.* Adverse effects associated with non-opioid and opioid treatment in patients with chronic pain. *Clin. Drug Investig.* **32 Suppl 1**, 53–63 (2012).

171. Benyamin, R. *et al.* Opioid complications and side effects. *Pain Physician* **11**, S105-20 (2008).

172. Rosenblum, A., Marsch, L. A., Joseph, H. & Portenoy, R. K. Opioids and the treatment of chronic pain: controversies, current status, and future directions. *Exp. Clin. Psychopharmacol.* **16**, 405–16 (2008).

173. Bohn, L. M., Gainetdinov, R. R., Lin, F. T., Lefkowitz, R. J. & Caron, M. G. Mu-opioid receptor desensitization by beta-arrestin-2 determines morphine tolerance but not dependence. *Nature* **408**, 720–3 (2000).

174. Al-Hasani, R. & Bruchas, M. R. Molecular mechanisms of opioid receptor-dependent signaling and behavior. *Anesthesiology* **115**, 1363–1381 (2011).

175. McPherson, K. B. & Ingram, S. L. Cellular and circuit diversity determines the impact of endogenous opioids in the descending pain modulatory pathway. *Front. Syst. Neurosci.* **16**, 963812 (2022).

176. Macey, T. A., Bobeck, E. N., Suchland, K. L., Morgan, M. M. & Ingram, S. L. Change in functional selectivity of morphine with the development of antinociceptive tolerance. *Br. J. Pharmacol.* **172**, 549–61 (2015).

177. Bagley, E. E., Chieng, B. C. H., Christie, M. J. & Connor, M. Opioid tolerance in periaqueductal gray neurons isolated from mice chronically treated with morphine. *Br. J. Pharmacol.* **146**, 68–76 (2005).

178. Hasselmo, M. E. The role of acetylcholine in learning and memory. *Curr. Opin. Neurobiol.* **16**, 710–5 (2006).

179. Al-Hasani, R. *et al.* Ventral tegmental area GABAergic inhibition of cholinergic interneurons in the ventral nucleus accumbens shell promotes reward reinforcement. *Nat. Neurosci.* **24**, 1414–1428 (2021).

180. Kerekes, N., Sanchéz-Pérez, A. M. & Landry, M. Neuroinflammation as a possible link between attention-deficit/hyperactivity disorder (ADHD) and pain. *Med. Hypotheses* **157**,

110717 (2021).

181. Takács, V. T. *et al.* Co-transmission of acetylcholine and GABA regulates hippocampal states. *Nat. Commun.* **9**, 2848 (2018).

182. Saunders, A., Granger, A. J. & Sabatini, B. L. Corelease of acetylcholine and GABA from cholinergic forebrain neurons. *Elife* **4**, (2015).

183. Weber, F. *et al.* Regulation of REM and Non-REM Sleep by Periaqueductal GABAergic Neurons. *Nat. Commun.* **9**, 354 (2018).

184. Patel, A. A., McAlinden, N., Mathieson, K. & Sakata, S. Simultaneous Electrophysiology and Fiber Photometry in Freely Behaving Mice. *Front. Neurosci.* **14**, 148 (2020).

185. Van Dort, C. J. *et al.* Optogenetic activation of cholinergic neurons in the PPT or LDT induces REM sleep. *Proc. Natl. Acad. Sci. U. S. A.* **112**, 584–9 (2015).

186. Mondoloni, S., Mameli, M. & Congiu, M. Reward and aversion encoding in the lateral habenula for innate and learned behaviours. *Transl. Psychiatry* **12**, 3 (2022).

187. Roy, D. S. *et al.* Brain-wide mapping reveals that engrams for a single memory are distributed across multiple brain regions. *Nat. Commun.* **13**, 1799 (2022).

188. Lawrenson, C. *et al.* Cerebellar modulation of memory encoding in the periaqueductal grey and fear behaviour. *Elife* **11**, (2022).

189. Záborszky, L. *et al.* Specific Basal Forebrain-Cortical Cholinergic Circuits Coordinate Cognitive Operations. *J. Neurosci.* **38**, 9446–9458 (2018).

190. Ballinger, E. C., Ananth, M., Talmage, D. A. & Role, L. W. Basal Forebrain Cholinergic Circuits and Signaling in Cognition and Cognitive Decline. *Neuron* **91**, 1199–1218 (2016).

191. Tashakori-Sabzevar, F. & Ward, R. D. Basal Forebrain Mediates Motivational Recruitment of Attention by Reward-Associated Cues. *Front. Neurosci.* **12**, 786 (2018).

192. Voytko, M. L. Cognitive functions of the basal forebrain cholinergic system in monkeys: memory or attention? *Behav. Brain Res.* **75**, 13–25 (1996).

193. Oliva, V. *et al.* Parallel cortical-brainstem pathways to attentional analgesia. *Neuroimage* **226**, 117548 (2021).

194. Oliva, V., Gregory, R., Brooks, J. C. W. & Pickering, A. E. Central pain modulatory mechanisms of attentional analgesia are preserved in fibromyalgia. *Pain* **163**, 125–136 (2022).

195. Colloca, L., Klinger, R., Flor, H. & Bingel, U. Placebo analgesia: psychological and

neurobiological mechanisms. *Pain* **154**, 511–514 (2013).

196. Schafer, S. M., Geuter, S. & Wager, T. D. Mechanisms of placebo analgesia: A dual-process model informed by insights from cross-species comparisons. *Prog. Neurobiol.* **160**, 101–122 (2018).

197. Zunhammer, M., Spisák, T., Wager, T. D., Bingel, U. & Placebo Imaging Consortium. Meta-analysis of neural systems underlying placebo analgesia from individual participant fMRI data. *Nat. Commun.* **12**, 1391 (2021).

198. Pati, D. & Kash, T. L. Tumor necrosis factor-α modulates GABAergic and dopaminergic neurons in the ventrolateral periaqueductal gray of female mice. *J. Neurophysiol.* **126**, 2119–2129 (2021).

199. Lau, B. K. & Vaughan, C. W. Descending modulation of pain: the GABA disinhibition hypothesis of analgesia. *Curr. Opin. Neurobiol.* **29**, 159–64 (2014).

200. Hahm, E.-T., Kim, Y., Lee, J.-J. & Cho, Y.-W. GABAergic synaptic response and its opioidergic modulation in periaqueductal gray neurons of rats with neuropathic pain. *BMC Neurosci.* **12**, 41 (2011).

201. Tonsfeldt, K. J. *et al.* Sex Differences in GABAA Signaling in the Periaqueductal Gray Induced by Persistent Inflammation. *J. Neurosci.* **36**, 1669–81 (2016).

202. Gao, Z. R. *et al.* Tac1-Expressing Neurons in the Periaqueductal Gray Facilitate the Itch-Scratching Cycle via Descending Regulation. *Neuron* **101**, 45-59.e9 (2019).

203. Samochocki, M. *et al.* Galantamine is an allosterically potentiating ligand of neuronal nicotinic but not of muscarinic acetylcholine receptors. *J. Pharmacol. Exp. Ther.* **305**, 1024–36 (2003).

204. Maier-Peuschel, M. *et al.* A fluorescence resonance energy transfer-based M2 muscarinic receptor sensor reveals rapid kinetics of allosteric modulation. *J. Biol. Chem.* **285**, 8793–800 (2010).

205. Wang, Y., Su, D.-M., Wang, R.-H., Liu, Y. & Wang, H. Antinociceptive effects of choline against acute and inflammatory pain. *Neuroscience* **132**, 49–56 (2005).

206. Hamurtekin, E. & Gurun, M. S. The antinociceptive effects of centrally administered CDP-choline on acute pain models in rats: the involvement of cholinergic system. *Brain Res.* **1117**, 92–100 (2006).

207. Damaj, M. I., Meyer, E. M. & Martin, B. R. The antinociceptive effects of alpha7 nicotinic agonists in an acute pain model. *Neuropharmacology* **39**, 2785–91 (2000).

208. Bagdas, D., Sonat, F. A., Hamurtekin, E., Sonal, S. & Gurun, M. S. The antihyperalgesic effect of cytidine-5’-diphosphate-choline in neuropathic and inflammatory pain models.

Behav. Pharmacol. **22**, 589–98 (2011).

209. Corradi, J. & Bouzat, C. Understanding the Bases of Function and Modulation of α7 Nicotinic Receptors: Implications for Drug Discovery. *Mol. Pharmacol.* **90**, 288–99 (2016).

210. Yakel, J. L. Nicotinic ACh receptors in the hippocampus: role in excitability and plasticity. *Nicotine Tob. Res.* **14**, 1249–57 (2012).

211. Kabbani, N. & Nichols, R. A. Beyond the Channel: Metabotropic Signaling by Nicotinic Receptors. *Trends Pharmacol. Sci.* **39**, 354–366 (2018).

212. Zdanowski, R., Krzyżowska, M., Ujazdowska, D., Lewicka, A. & Lewicki, S. Role of α7 nicotinic receptor in the immune system and intracellular signaling pathways. *Cent. J. Immunol.* **40**, 373–9 (2015).

213. King, J. R., Gillevet, T. C. & Kabbani, N. A G protein-coupled α7 nicotinic receptor regulates signaling and TNF-α release in microglia. *FEBS Open Bio* **7**, 1350–1361 (2017).

214. Udakis, M., Wright, V. L., Wonnacott, S. & Bailey, C. P. Integration of inhibitory and excitatory effects of α7 nicotinic acetylcholine receptor activation in the prelimbic cortex regulates network activity and plasticity. *Neuropharmacology* **105**, 618–629 (2016).

215. Sawamura, N., Ju, Y. & Asahi, T. Cholinergic receptor, nicotinic, alpha 7 as a target molecule of Arctic mutant amyloid β. *Neural Regen. Res.* **13**, 1360–1361 (2018).

216. Souza, C. M. *et al.* JAK2/STAT3 Pathway is Required for α7nAChR-Dependent Expression of POMC and AGRP Neuropeptides in Male Mice. *Cell. Physiol. Biochem.* **53**, 701–712 (2019).

217. Charpantier, E. *et al.* Alpha7 neuronal nicotinic acetylcholine receptors are negatively regulated by tyrosine phosphorylation and Src-family kinases. *J. Neurosci.* **25**, 9836–49 (2005).

218. Johnson, S. L., Beurg, M., Marcotti, W. & Fettiplace, R. Prestin-driven cochlear amplification is not limited by the outer hair cell membrane time constant. *Neuron* **70**, 1143–54 (2011).

219. Daoudal, G. & Debanne, D. Long-term plasticity of intrinsic excitability: learning rules and mechanisms. *Learn. Mem.* **10**, 456–65.

220. van Welie, I., van Hooft, J. A. & Wadman, W. J. Homeostatic scaling of neuronal excitability by synaptic modulation of somatic hyperpolarization-activated Ih channels. *Proc. Natl. Acad. Sci. U. S. A.* **101**, 5123–8 (2004).

221. Nelson, A. B., Krispel, C. M., Sekirnjak, C. & du Lac, S. Long-lasting increases in intrinsic excitability triggered by inhibition. *Neuron* **40**, 609–20 (2003).

222. Gottschalk, A. *et al.* Identification and characterization of novel nicotinic receptor-associated proteins in Caenorhabditis elegans. *EMBO J.* **24**, 2566–78 (2005).

223. McClure-Begley, T. D. *et al.* Exploring the nicotinic acetylcholine receptor-associated proteome with iTRAQ and transgenic mice. *Genomics. Proteomics Bioinformatics* **11**, 207–18 (2013).

224. Shen, J. & Yakel, J. L. Nicotinic acetylcholine receptor-mediated calcium signaling in the nervous system. *Acta Pharmacol. Sin.* **30**, 673–80 (2009).

225. Decker, E. R. & Dani, J. A. Calcium permeability of the nicotinic acetylcholine receptor: the single-channel calcium influx is significant. *J. Neurosci.* **10**, 3413–20 (1990).

226. Dani, J. A. Neuronal Nicotinic Acetylcholine Receptor Structure and Function and Response to Nicotine. *Int. Rev. Neurobiol.* **124**, 3–19 (2015).

227. Belforte, N. *et al.* AMPK hyperactivation promotes dendrite retraction, synaptic loss, and neuronal dysfunction in glaucoma. *Mol. Neurodegener.* **16**, 43 (2021).

228. Williams, T., Courchet, J., Viollet, B., Brenman, J. E. & Polleux, F. AMP-activated protein kinase (AMPK) activity is not required for neuronal development but regulates axogenesis during metabolic stress. *Proc. Natl. Acad. Sci. U. S. A.* **108**, 5849–54 (2011).

229. Domise, M. *et al.* Neuronal AMP-activated protein kinase hyper-activation induces synaptic loss by an autophagy-mediated process. *Cell Death Dis.* **10**, 221 (2019).

230. Wójtowicz, S., Strosznajder, A. K., Jeżyna, M. & Strosznajder, J. B. The Novel Role of PPAR Alpha in the Brain: Promising Target in Therapy of Alzheimer’s Disease and Other Neurodegenerative Disorders. *Neurochem. Res.* **45**, 972–988 (2020).

231. Tyagi, S., Gupta, P., Saini, A. S., Kaushal, C. & Sharma, S. The peroxisome proliferator-activated receptor: A family of nuclear receptors role in various diseases. *J. Adv. Pharm. Technol. Res.* **2**, 236–40 (2011).

232. Grygiel-Górniak, B. Peroxisome proliferator-activated receptors and their ligands: nutritional and clinical implications--a review. *Nutr. J.* **13**, 17 (2014).

233. Slivicki, R. A. *et al.* Positive Allosteric Modulation of Cannabinoid Receptor Type 1 Suppresses Pathological Pain Without Producing Tolerance or Dependence. *Biol. Psychiatry* **84**, 722–733 (2018).

234. Datta, U., Kelley, L. K., Middleton, J. W. & Gilpin, N. W. Positive allosteric modulation of the cannabinoid type-1 receptor (CB1R) in periaqueductal gray (PAG) antagonizes anti-nociceptive and cellular effects of a mu-opioid receptor agonist in morphine-withdrawn rats. *Psychopharmacology (Berl).* **237**, 3729–3739 (2020).

235. Slivicki, R. A. *et al.* Positive Allosteric Modulation of CB1 Cannabinoid Receptor

Signaling Enhances Morphine Antinociception and Attenuates Morphine Tolerance Without Enhancing Morphine- Induced Dependence or Reward. *Front. Mol. Neurosci.* **13**, 54 (2020).

236. Jiang, Z. *et al.* Sex-specific cannabinoid 1 receptors on GABAergic neurons in the ventrolateral periaqueductal gray mediate analgesia in mice. *J. Comp. Neurol.* **530**, 2315–2334 (2022).

237. Winters, B. L., Lau, B. K. & Vaughan, C. W. Cannabinoids and Opioids Differentially Target Extrinsic and Intrinsic GABAergic Inputs onto the Periaqueductal Grey Descending Pathway. *J. Neurosci.* JN-RM-0997-22 (2022) doi:10.1523/JNEUROSCI.0997-22.2022.

238. Mohebi, A. *et al.* Dissociable dopamine dynamics for learning and motivation. *Nature* **570**, 65–70 (2019).